The Dissertation Committee for Javid Shiriyev Certifies that this is the approved version of the following Dissertation:

A Tri-Axial Electromagnetic Induction Tool for Hydraulic Fracture Diagnostics

Committee:

Mukul M. Sharma, Supervisor

Mrinal K. Sen

John T. Foster

Quoc P. Nguyen

Hugh Daigle

A TRI-AXIAL ELECTROMAGNETIC INDUCTION TOOL FOR HYDRAULIC FRACTURE DIAGNOSTICS

by

Javid Shiriyev

Dissertation

Presented to the Faculty of the Graduate School of

The University of Texas at Austin

in Partial Fulfillment

of the Requirements

for the Degree of

Doctor of Philosophy

The University of Texas at Austin

December 2018

Dedication

to Onc. Dr. Tarana Babayeva

Acknowledgements

I would like to express my sincere gratitude to my advisor, Dr. Mukul M. Sharma, for his guidance, support and encouragement throughout the duration of my study. I am very much happy to be a part of his cooperative research team and enjoyed every part of the project. His experience and vision enriched this work, and his questions motivated me to explore more.

I also want to thank all my dissertation committee members for answering any related questions and reviewing the work. My special thanks to Dr. Foster for his offered classes which helped me to have a good foundation of coding and to Dr. Mrinal Sen who helped me to build a good understanding of inversion analysis.

Many thanks go to Yaniv Brick for his patience, support and encouragement during this study. He helped me to grasp all the previous modeling work and guided me at the beginning of the project. I am also very lucky to have Peng Zhang as a fellow researcher who helped me in theoretical parts and supported me in the experiments.

Rodney T. Russell, Tom Hosbach, Mark Oerkfitz, Dave Glowka and Jeff Gabelmann deserve a special mention for their contribution to the experimental part of this dissertation. Their experience made the flow of work as smooth as possible. Thanks to Jin Kyung Lee for providing support and always being there to listen to any of my problems.

I would like to thank Onur Balan and Anuj Gupta for providing me an internship opportunity in Aramco Services Company which increased my understanding of fracture monitoring. I would also like to thank Elnur Aliyev and Orkhan Samandarli for sharing their knowledge and experience which is invaluable to me.

I feel very lucky to have caring people around me all this time. Thanks to Cagdas Eritici and Elif Ozdingis with whom I started the journey in the city of Austin. I am happy to have Hector Barrios and Igor Shovkun as friends and colleagues with whom it was never boring. It was always joyful and adventurous to spend time with my cheerful friends Sercan Gul, Tayyar Ozel, Kahraman Barut, Betsy Tal and Sean Brame. Many thanks to Emre Ozen, Hayrettin Aygol, Zeki Erincik and Namaz Gurbanov who never hesitated to offer their help in any difficulty. I am also very happy to have dear old friends Selin Guven, Tugce Ozdemir and Abbas Abbasov with whom it was always pleasant to talk disregarding the distance and time zone differences.

Finally, I would like to thank my father and best friend Farhad, my beautiful sister Parvin, my brother-in-law Fuad and my lovely niece Ayla for their unconditional love, support and encouragement.

Abstract

A Tri-Axial Electromagnetic Induction Tool for Hydraulic Fracture Diagnostics

Javid Shiriyev, Ph.D.

The University of Texas at Austin, 2018

Supervisor: Mukul M. Sharma

The monitoring and diagnostics of induced fractures are important for the real-time performance evaluation of hydraulic fracturing operations. Previous electromagnetic (EM) based studies show that single backbone tri-axial induction logging tools are promising candidates for the real-time monitoring and diagnosis of fractures in uncased wells. To support the development of field deployable tools, the concept must be tested in experiments, in a controllable environment, before it is tested under field-like conditions. To this end, we have developed numerical tools which can simulate any wellbore environment while logging hydraulic fractures with the induction tool. We have designed and built a prototype induction tool and performed two sets of tests to compare with numerical simulation results. The computational and experimental setup consists of tri-axial transmitter and receiver coils in co-axial, co-planar and cross-polarized configurations. Both lab and shallow earth measurements are shown to be in good agreement with simulations for all examined cases. The average relative and maximum discrepancies of the measured signals from the simulated ones were lower than 3% and 10%, respectively. With the prototype tool, strong signals sensitive to the fracture's

surface area and dip-angle were measured in the co-axial coil configuration, while weaker signals sensitive to the fracture's aspect ratio were observed in the co-planar configuration. Cross-polarized signals are also shown to be strong and sensitive to the fracture's dip. Lastly, we resolved the detectable components of the measured signal tensor to obtain parameters for simplified fracture geometries. The inversion algorithm, a derivative free directional search model, uses an objective function defined as a combination of co-axial and cross-polarized signals from different tool spacing, and the function provides a well behaved global minimum. The robustness of the inversion algorithm is tested on synthetic data for single cluster fractures in a homogeneous and heterogeneous background electrical conductivity. All the effective model parameters for different cases, electrical conductivity, size and dip-angle, are shown to be recovered with good accuracy. We also evaluated the effect of neighboring fractures and suggested a multi-cluster inversion path which can recover the proppant distribution in a stage very accurately. Based on the numerical and experimental results we suggest a tool with specifications that can effectively recover far-field proppant distribution in the fractures.

Table of Contents

List of Tables

List of Figures

Chapter 1: INTRODUCTION

While traditional hydrocarbon recovery techniques are not applicable in shales because of their very small matrix permeability, a recent combination of hydraulic fracturing treatments with horizontal drilling has led to a breakthrough in hydrocarbon production. To evaluate the outcomes and performance of such hydraulic fracturing treatments, induced propped fractures must be monitored, appraised and quantified. Indeed, unpropped portions of induced fractures close under high net stress shortly after fracing and may not contribute to well productivity (Sharma and Manchanda, 2015); thus, it is crucial to determine the spatial distribution of proppants for successful fracture diagnostics.

Conventional fracture diagnostic techniques are based on sensing physical events that occur during fracture growth. For example, microseismic detection is based on the monitoring of the shear waves generated due to rock failure in the vicinity of the hydraulic fracture or fracture network (Batchelor et al., 1983). Tiltmeter mapping is another commonly used technique, which is based on measuring fracture-induced rock deformations and relating them to the induced fracture geometry (Warpinski and Branagan, 1989). These techniques lack the correlation between the measured physical events and settled proppant locations and thus are not suitable for deducing proppant distributions and well productivity.

More recent fiber optic based measurements provide data that can be qualitatively interpreted for the efficiency of proppant placement. The application of fiber optics has the advantage of providing continuous wellbore monitoring capabilities during the injection, shut-in and production phases of fracturing operations and full-length wellbore characteristics can be transferred to the surface in real-time. Moreover, it requires no

installation of any down-hole equipment to interfere with field operations. A single fiber optic cable temporarily/permanently installed in the well may provide characteristics such as temperature (DTS), acoustic (DAS), strain (DSS), etc. (Smolen and Spek, 2003). Monitoring with only DTS lacks the same correlation with proppant location, and in some applications, DAS/DTS data have been used to infer dominant perforation clusters that are taking most of the fracturing fluid and proppant (Sookprasong et al., 2014; Wheaton et al., 2016). Such measurements have been used to avoid frack-hits while fracturing and to determine and eliminate dominant clusters. The measurements have shown that the fractures are heel dominated and that special steps may need to be taken to optimize the number of clusters per stage, spacing between clusters/stages and fracturing fluid injection rate to avoid non-uniform fluid/proppant distribution (Ugueto et al., 2016; Wu et al., 2017).

A more promising alternative for proppant detection is to use techniques that rely on sensing electromagnetic (EM) fields scattered due to the contrast in EM material properties between propped fractures and the surrounding formation. Although the contrast in EM properties can be enhanced by increasing the proppant's electrical conductivity, magnetic permeability, electrical permittivity, or a combination of them (Heagy and Oldenburg, 2013), enhancing the conductivity contrast generally enables better detectability compared to the other alternatives (LaBrecque et al., 2016) and is more practical. In fact, numerous proppant types have been reported to exhibit large effective electrical conductivities (LaBrecque et al., 2016; Palisch et al., 2016; Zhang et al., 2016; Hoversten et al., 2015).

A variety of field data acquisition techniques can be implemented to sense the EM fields scattered from proppants that display a large electrical conductivity contrast over the background shale. One acquisition technique, employed in LaBrecque et al. (2016),

Palisch et al. (2016), and Hibbs (2014), is to use receiver arrays densely deployed on the surface to sense the response to an electric current emitted into the subsurface by electrodes. While the spatially dense surface receiver array allows for relatively extensive coverage of the stimulated area, this transmitter-receiver coupling is inherently depth limited. As the source-observer distance increases, EM fields are significantly attenuated by the overburden layers greatly obfuscating the signals of interest.

This limitation can be considerably mitigated by utilizing source/observers in the vicinity of propped hydraulic fractures. The electrically conductive proppant can then be mapped using a single-backbone, electromagnetic induction tool (Salies, 2012; Basu, 2014). This has the potential to offer a cheap (Gul and Aslanoglu, 2018) far-field proppant detection technique that can be executed from a single wellbore at any time during the well's life cycle. The method can provide a time-lapse analysis of fracture growth or closure which can decrease the uncertainties in reservoir parameters critical for long-term production forecasting (Balan et al., 2017) where data-driven analyses are not available (Eftekhari et al., 2018). Furthermore, the application of such measurements in the field can be incorporated with complex-fracture proppant transport models (Shrivastava and Sharma, 2018) to improve their reliability.

In Pardo and Torres-Verdin (2013), Basu and Sharma (2014), Yang et al. (2015), and Zhang et al. (2016) such a low-frequency induction tool, where both sources and observers (tri-axial induction coils) are placed on the same backbone, were numerically studied and found to be sensitive to various propped fracture properties in open-hole hole completion wells. These findings were corroborated by independent laboratory experiments in Yu et al. (2016) that used a scaled-down co-axial induction tool and scaled-up electrical conductivities to evaluate orthogonal fractures. According to numerical forward studies and parametric inversion analyses with synthetic data (Yang et

al., 2015/2016), different transmitter/receiver coil configurations are sensitive to different propped fracture properties (area, shape and dip) and the best response occurs when the primary magnetic field is perpendicular to the plane of the target (Swift, 1988). In this dissertation, we further study the induction tool with fast and robust numerical forward and inversion models and conduct a complete set of experiments with a prototype tool.

1.1. LOW FREQUENCY ELECTROMAGNETIC INDUCTION TOOL

The low-frequency induction logging tool (Fig. 1.1) described in this dissertation is similar to those analyzed theoretically in Salies (2012), Pardo and Torres-Verdin (2013), Basu and Sharma (2014), Yang et al. (2015), and Zhang et al. (2016). It includes a tri-axial transmitter (Tx) coil that generates EM fields and a tri-axial receiver coil set composed of two coils, Rx_1 and Rx_2, measuring the EM response of the surrounding formation to those fields (Duesterhoeft et al., 1961). The measured total voltage on each of the receiver coils can be described as the superposition of two contributions: (i) a primary contribution corresponding to the fields in the shale formation in the absence of induced fractures and (ii) a secondary contribution that can be associated with fields arising due to the presence of a fracture filled with an electrically conductive proppant.

To formulate the tool's response we denote $\mathbf{H}_v^{\{\mathrm{p,s,t}\}}(\mathbf{r})$ the {primary, secondary, total} magnetic field at point $\mathbf{r}$, excited by a transmitter coil oriented in the $v \in \{x, y, z\}$ direction. We follow the $\mathrm{e}^{j\omega t}$ time convention used in engineering. For all figures, the Cartesian coordinate system is defined such that the positive z-axis is the direction of a horizontal wellbore, and the positive x-axis is the vertical direction opposite to gravity (Fig. 1.1). The signals of interest, for a receiver set oriented in the $u \in \{x, y, z\}$ direction, are given by

$$\Delta U_{uv}^{\{p,s,t\}} = -j\omega\mu_0 A_{RX} N_{RX} \hat{\mathbf{u}} \cdot \left[\mathbf{H}_v^{\{p,s,t\}}(\mathbf{r}_{Rx2}) - \mathbf{H}_v^{\{p,s,t\}}(\mathbf{r}_{Rx1}) \left(\frac{l_1}{l_2}\right)^3 \right] \quad (1.1)$$

where $\Delta U_{uv}^{\{p,s,t\}}$ are the bucked voltages, A_{RX} is the area of the receiver coils positioned at $\mathbf{r}_{RX1}$ and $\mathbf{r}_{RX2}$, N_{RX} is number of turns in the receiver coils, μ_0 is free-space magnetic permeability, and $(l_1/l_2)^3$ is a bucking coefficient used to approximately cancel the dominant imaginary component of the primary field (Lovell, 1993). Bucking increases the tool's sensitivity to small variations in the total magnetic field but must be carefully calibrated: for thin coils, l_1 and l_2 are the distances between the receiver and the transmitter coil's center. For such simple geometries, bucking can yield close to perfect primary component cancellation for low frequency signals in air, accounting for the $1/R^3$ decay of the primary field at distance R from the source. In practice, however, the coils are of finite length and thus should be calibrated for optimal cancellation of the primary signal prior to data acquisition in the well.

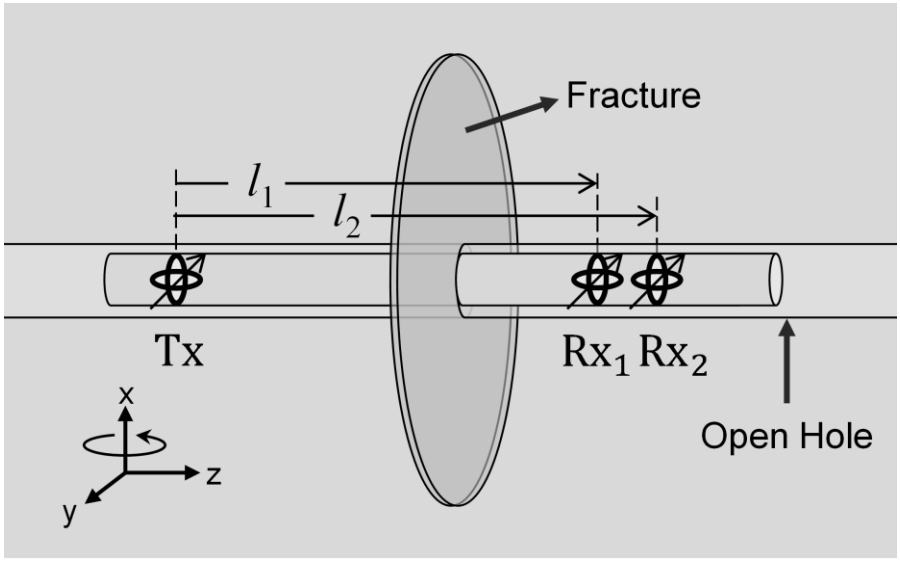

Figure 1.1: An electromagnetic induction logging tool with a single spacing couple: tri-axial transmitter (Tx) and receiver/bucking (Rx_1/Rx_2) coils.

The utilization of a tri-axial receiver coil system allows acquisition of more parameters of the fractures. In the previous numerical study, co-axial measurements were shown to be sensitive to the fracture cross-sectional area but cannot differentiate fractures of the same area with different cross-sectional shapes or dips. Transverse co-polarized measurements can discern axially symmetric from asymmetric ones and cross-polarized measurements can quantify fracture dip-angle and become more sensitive as the dip-angle increases (Yang et al., 2015).

An actual measurement in the field involves two passes of the tool along the wellbore, before and after the hydraulic fracturing operation, during which the bucked signals $\Delta U_{uv}^{\mathrm{p}}$ (before the hydraulic fracturing) and $\Delta U_{uv}^{\mathrm{t}}$ (after the hydraulic fracturing) are recorded. The difference between these bucked signals is given by:

$$\Delta U_{uv}^{\mathrm{s}} = \Delta U_{uv}^{\mathrm{t}} - \Delta U_{uv}^{\mathrm{p}} \tag{1.2}$$

This is referred as the "differential signal" in this dissertation. Since the distance between transmitter and receiver coils dictates the depth of investigation of the tool, three receiver coil sets at different distances from the tri-axial transmitter coil have been suggested to investigate fractures far away from the wellbore (Fig. 1.2). The short spacing can detect smaller fractures but is insensitive to larger ones. The signals from the long spacing are inherently weak but can distinguish larger fractures. The upper bound of sensitivity was shown to be 10 m^2 for the short spacing and 1000 m^2 for the long spacing receiver couples.

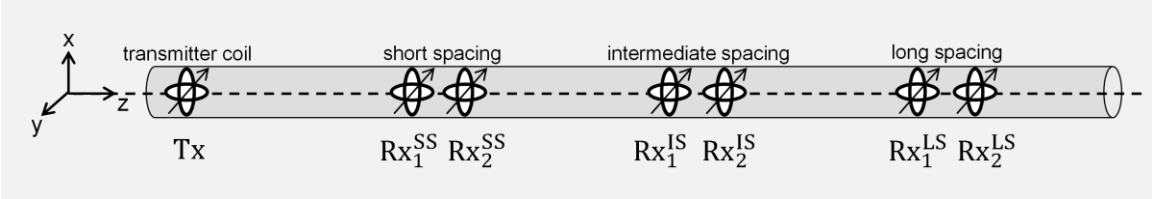

Figure 1.2: An electromagnetic induction logging tool with three spacings: short, intermediate and long spacing transmitter-receivers couples.

Table 1.1 shows nominal spacings used for the tool in the previous studies; we will use the same nominal distances.

Short Spacing		**Intermediate Spacing**		**Long Spacing**	
l_1^{SS} (m)	l_2^{SS} (m)	l_1^{IS} (m)	l_2^{IS} (m)	l_1^{LS} (m)	l_2^{LS} (m)
1.2	1.5	5.0	5.6	18.0	19.2

Table 1.1: Nominal tool spacings, the distance between transmitter and receiver/bucking coils, for short, intermediate and long spacings.

1.2. PROBLEM STATEMENT

Previous numerical studies presented for induction tools are more generic and not specialized for this range of frequencies. These models are computationally demanding and the time cost for these forward models do not allow inversion algorithms to be implemented in a time efficient manner. Moreover, the estimation of particular parameters from real signals measured in the field is likely to be limited by various factors not modeled in numerical studies, including the actual ambient noise and manufacturing uncertainties in the tool itself. To be able to judge the predictive value, and ultimately the potential of single backbone EM tools for propped fracture diagnosis, the detectability and differentiability of realistic signal levels corresponding to fractures

of various geometries must be studied experimentally with realistically sized tri-axial coils.

All the previous work theoretically demonstrates the method's capability to detect and characterize propped fractures, but numerous gaps still exist before this technology can be deployed in the field. These include, for example, specifications of transmitting and receiving components, uncertainty in their positioning, the required resolution of the processed signals, their sensitivity to the actual noise, etc. To bridge the gap between the theoretical proof of concept and a field deployable tool, the design, and testing of a lower-risk initial prototype is required. This testing should enable refining the tool specifications to guarantee its robustness while avoiding difficult and expensive down-hole measurements. In this study we have experimentally verified this technique and developed a list of recommended specifications and practices for a field deployable tool.

1.3. RESEARCH OBJECTIVES

The main research objective of this study is to verify the proposed methodology in a lab and field-like scenario and validate the numerical forward models used both for the simulation of the experimental and downhole scenarios and later as the cornerstone for an inversion analysis. In particular:

- To develop a laboratory measurement technique that can emulate hydraulic fractures in a controlled environment;
- To build a prototype tool which is very close in design to a field deployable tool;
- To develop a numerical forward model that can be compared with experimental results and is fast/robust enough to be used in the inversion analysis;
- To develop an inversion algorithm that is automated, fast and robust and ready to be used in a field.

The efforts, results and conclusions of the dissertation will enable the design and manufacturing of a field deployable tool.

1.4. DISSERTATION OUTLINE

This dissertation is divided into five chapters. A numerical model shown in Chapter 2 is compared to the response of a prototype tool described in Chapter 3. Then, a stochastic inversion algorithm is developed and described in Chapter 4 which is ready to use with field data. The last chapter uses both numerical and inversion models to demonstrate the capabilities of the tool and to make recommendations for field deployment. All forward and inversion models can be found in the Appendix of this dissertation.

Chapter 2 describes two numerical algorithms invoked to compute the response of the tool to the targets with EM contrast. The models developed here allow the regions of different EM properties to be included around the tool with little computational effort. We effectively utilize surface integral equations for the open-hole application and an axial hybrid method for the computation of tool response inside the production casing.

In Chapter 3, we describe the experimental system, including the design of a particular prototype tool and target models and measurement procedures for tests in laboratory and field environments; importantly, the coil sizes and operation frequency are not scaled. The experimentally measured signals are described and compared to numerical simulations for various receiver and transmitter configurations. These fracture models have increased electrical conductivity and reduced thickness, designed to provide signal levels similar to those expected from realistic propped fractures.

Chapter 4 develops a stochastic inversion algorithm for the full automated inversion of the tool's response. The model is validated with testing function and used for

the parametrized fracture model. We used synthetic data to evaluate the sensitivity of the signals to fracture electrical conductivity, size and dip-angle. The chapter also studies the effect of neighboring fractures on the recorded signals to accurately identify proppant distribution among the clusters of a stage.

In Chapter 5, we used numerical and forward models to evaluate the investigation area of the tool with the given optimized frequency and tool spacings. We further simulated inter-well deployment; showed the potential for the evaluation of proppant settlement. Finally, we simulated and presented results for proppants with enhanced electrical permittivity and magnetic permeability.

Chapter 2: NUMERICAL MODELING OF ELECTRICALLY CONDUCTIVE TARGETS

In this chapter, numerical modeling tools are presented to simulate the induction tool response while logging propped fractures both in open- and cased-hole applications. We are using methods which can simulate proppant distribution in fractures with arbitrary geometry which are not necessarily orthogonal to the wellbore. Wellbores may contain casing and/or fluid in the wellbore which may have electromagnetic properties that are very different than that of the proppant and background formation.

We develop two numerical models to simulate the tool's response in a time-efficient manner. The first model is based on the implementation of impedance boundary conditions to the surface integral equations and solving this system with a method of moments (MOM) (Rao et al., 1982; Qian et al., 2007). The convergence, validation, possible approximation and computation time analyses are shown in the following subsections. The second model is based on the axial hybrid method which simulates transversely isotropic media (Zhang et al., 1999; Wang et al., 2009). The model is mainly used to understand the behavior of the tool's response inside a production casing, and some analyses of the numerical features are shown at the end. In both cases, the governing equations are discussed in detail.

2.1. LITERATURE REVIEW

While logging a well with an induction tool, the tool is pulled along the wellbore and transmitter coils are excited at certain sampling points. The solution of the induction tool response to the propped fractures has to consider many excitation points. Therefore, a frequency domain computation is ideal for the analyses of the suggested single frequency tool where the system matrix obtained after deploying a numerical technique is

usually independent of excitations. Once this matrix is inverted or factorized, it can be used to obtain solutions to all excitations. Moreover, since the frequency-domain methods solve Maxwell's equations at each frequency, they can deal with dispersive media[1] easily.

Maxwell's equations in the frequency domain can be solved in 3-D using one of several numerical methods. The family of finite difference and finite element methods solves Maxwell's equations or their weak form representations directly but requires the solution domain to be truncated and treated carefully so that the truncated computational domain mimics the original open space. The method of moments, on the other hand, solves Maxwell's equations indirectly by dealing with integral equations formulated using the fundamental solution to a point source which is known as a Green's function. This simulation method is especially well suited for our analysis because it confines the computational domain to the anomalous conductivity region only.

The classical method of moment solution of the volume electric field integral equations is limited to small-scale problems because the integral equation methods yield fully populated matrices. In Yang et al. (2014; 2015), an adaptive integral method is used to accelerate the solution to the induction problem by making use of the translational invariance of Green's functions. Approximately 150, 1500 and 1800 minutes are spent on filling matrices, and the memory requirement is 1.6, 13 and 34 GB for solving a problem with 20,729, 120,000 and 320,000 unknowns, respectively. This is still computationally intensive especially if we consider the inversion analysis which requires multiple runs of the forward model to determine the fracture parameters. Moreover, high conductivity

[1]The medium is called dispersive if electromagnetic properties are dependent on the frequency of the field.

contrast between the fracture and formation cannot be easily handled because of the failure in convergence in the iterative procedure.

While simulating an open-hole induction tool response, Zhang et al. (2016) has shown negligible effects of the wellbore fluid on the results by testing different sizes of circular fractures with and without a borehole. This is due to the very high electrical conductivity contrast between the proppant filled fracture and the rock formation. In the same paper, a single thin bulk volume of a constant effective thickness was shown to be equivalent of a thin complex fracture showing that signal responses depend on fracture total volume rather than on fracture complexity. Removing the borehole not only significantly decreases the number of unknowns boosting the speed of the forward model but also allows deploying integral equations to be solved on the surface of the fracture.

The number of unknowns resulting from surface discretization is significantly smaller than that from volume discretization; therefore, the method of moments is much more efficient when it deals with surface integral equations (SIE). It enables meshing the surface with a typical element length that is not dictated by the penetration depth inside the conductive fracture as would be required for a volumetric integral equation solution. In this current work, we are using surface integral equations for simulating the open-hole application of the induction tool. This technique allows simulation of all fracture parameters listed in Yang et al. (2016): fracture location, conductivity, size, shape factor and dip-angle.

To avoid an outrageous increase in the number of unknowns when a casing pipe is introduced to the computational domain tremendous speed up can be obtained by decreasing the dimensions of the problem. In cylindrical coordinates, the ϕ-direction of the problem can be eliminated by use of a Fourier series, and the set of 2D problems can be solved with different types of numerical solvers. Although we lose the capability of

simulating the fracture parameters such as shape factor and dip-angle, this technique provides a very practical solution to the original large problem. In this dissertation, we use the axial hybrid method to solve the reduced 2D problem where the numerical solution is obtained in the wellbore direction, and a family of normalized Bessel functions is used to describe the EM fields in the radial direction (Gianzero et al., 1985; Pai, 1991; Li and Shen, 1993).

2.2. OPEN-HOLE SIMULATION OF INDUCTION TOOL

In this application of induction tools, the thickness of fractures is much smaller than their length and skin depth. This allows us to make the assumption of a zero thickness surface for the fracture models, rather than a very thin volume (Yang et al., 2015; Zhang et al., 2016), facilitating the use of surface integral equations (Ren et al., 2016). The magnetic fields $\mathbf{H}_v^{sca}(\mathbf{r})$ are computed in two main steps: 1) by discretizing the surface with triangular elements to calculate the surface currents on the anomalous region of conductivity by applying an impedance boundary condition; and 2) calculating the scattered fields on the observation points induced by these currents.

A model to simulate responses for a given perfectly electrically conductive (PEC) geometry was formulated and described earlier in Rao et al. (1982). In this work, an impedance boundary condition is implemented due to the finite conductivity and thickness of fractures as described in Lindell (1992). Before proceeding to numerical results, the basic steps of the computation are shown below. First, we start with the formulation of an integral equation for the problem under consideration. Second, the equation is expanded and tested with the same basis functions to convert the integral form of equations into the linear system of equations. Finally, the matrix equation is solved for the unknown coefficients and the desired magnetic fields are calculated. In the numerical

solution of integral equations shown below, the reservoir is assumed to have a homogeneous electrical conductivity.

2.2.1. Surface Integral Equation with Impedance Boundary Condition

The electromagnetic field generated by a time-harmonic source, a source oscillating with a single frequency, defined by volume electric current density **J** and volume magnetic current density **M** satisfies Maxwell's equations:

$$\nabla \times \mathbf{E} = -j\omega\mu\mathbf{H} - \mathbf{M} \tag{2.1}$$

$$\nabla \times \mathbf{H} = j\omega\tilde{\varepsilon}\mathbf{E} + \mathbf{J} \tag{2.2}$$

$$\nabla \cdot (\tilde{\varepsilon}\mathbf{E}) = \rho_e \tag{2.3}$$

$$\nabla \cdot (\mu\mathbf{H}) = \rho_m \tag{2.4}$$

If we assume that both electric and magnetic fields exist only due to the electric source then the problem can be formulated as follows:

$$\mathbf{E} = -j\omega\mathbf{A} - \nabla\varphi \tag{2.5}$$

$$\mathbf{H} = \frac{1}{\mu}\nabla \times \mathbf{A} \tag{2.6}$$

where the second component of the right-hand side in Eq. 2.5 can be represented in terms of **A** as well. For the given surface, the solution of **A** and φ are given by:

$$\mathbf{A}(\mathbf{r}) = \mu \iint_S \mathbf{J}_s(\mathrm{r}')G_{\mathrm{R}}(\mathbf{r},\mathbf{r}')\,dS' \tag{2.7}$$

$$\varphi(\mathbf{r}) = -\frac{1}{j\omega\tilde{\varepsilon}} \iint_S \nabla' \cdot \mathbf{J}_s(\mathbf{r}')G_{\mathrm{R}}(\mathbf{r},\mathbf{r}')\,dS' \tag{2.8}$$

in terms of surface current $\mathbf{J}_s$. Here, $\mathbf{r}$ and $\mathbf{r}'$ are observer and source points, respectively; and the Green's function is given as:

$$G_{\mathrm{R}}(\mathbf{r},\mathbf{r}') = \frac{e^{-jk|\mathbf{r}-\mathbf{r}'|}}{4\pi|\mathbf{r}-\mathbf{r}'|} \tag{2.9}$$

The wavenumber is given as:

$$k = \sqrt{\omega^2 \mu \tilde{\varepsilon}} \tag{2.10}$$

and the complex permittivity is defined as:

$$\tilde{\varepsilon} = \varepsilon - j\frac{\sigma}{\omega} \tag{2.11}$$

As can be seen from the equations above, if we find $\mathbf{J}_s$ then we can calculate the electromagnetic field on any observation point. To calculate $\mathbf{J}_s$, we need to apply impedance boundary conditions on the surface of the fracture. This boundary condition is similar to the PEC condition but with non-zero fields on both sides of the surface:

$$\hat{\mathbf{n}} \times \hat{\mathbf{n}} \times \left(\mathbf{E}^{\mathrm{sca}} + \mathbf{E}^{\mathrm{inc}}\right) = -Z_s \mathbf{J}_s \tag{2.12}$$

where $\hat{\mathbf{n}}$ is the unit normal vector of the surface, and Z_s is a surface impedance assigned to the target. Finite thickness and conductivity of fracture can be incorporated to the surface impedance as shown in Lindell (1992):

$$Z_s = \left[\sigma t + \frac{j}{\eta_{\mathrm{o}}}(\varepsilon_r - 1)k_{\mathrm{o}} t\right]^{-1} \tag{2.13}$$

The inverse of this equation is referred as the shunt admittance. For the more generalized impedance boundary condition, one can refer to the study by Qian et al. (2007). In cases when the fracture model has a relative permittivity of one, only the first part of the right-hand side is non-trivial. After taking the cross product of both sides of Eq. 2.12 with a normal vector and substituting the expressions for the electric field and surface impedance, the integral equation can be formulated as follows:

$$\hat{\mathbf{n}} \times (j\omega\mathbf{A} + \nabla\varphi) + \frac{\hat{\mathbf{n}} \times \mathbf{J}_s}{\sigma t} = \hat{\mathbf{n}} \times \mathbf{E}^{\text{inc}} \tag{2.14}$$

To solve Eq. 2.14, Rao-Wilton-Glisson (RWG) basis functions (Rao et al., 1982) are defined on triangular patches (Fig. 2.1) used to discretize the surface, and then surface currents $\mathbf{J}_s$ are approximated as follows:

$$\mathbf{J}_s(\mathbf{r}) \cong \sum_{n=1}^{N} l_n \mathbf{\Lambda}_n(\mathbf{r}) \tag{2.15}$$

In Fig 2.1, the plus or minus sign designation of the triangles is determined by the choice of a positive current reference direction for the nth edge, the reference for which is assumed to be from T_n^+ to T_n^-. The same figure includes the equation for the vector basis function and its divergence associated with the n^{th} edge.

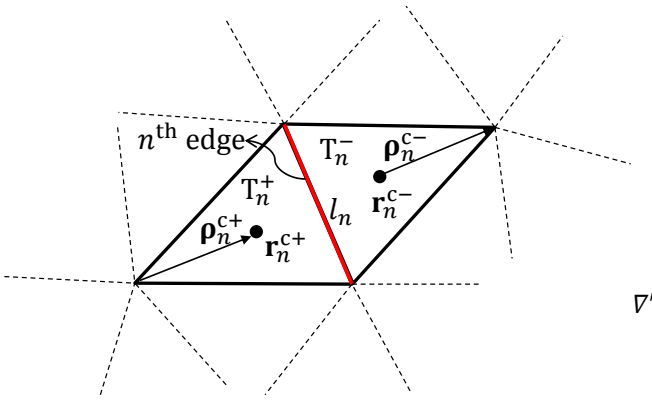

$$\mathbf{\Lambda}_n(\mathbf{r}) = \begin{cases} \frac{l_n}{2A_n^+}\boldsymbol{\rho}_n^+ & \mathbf{r} \in T_n^+ \\ \frac{l_n}{2A_n^-}\boldsymbol{\rho}_n^- & \mathbf{r} \in T_n^- \\ 0 & \text{otherwise} \end{cases}$$

$$\nabla' \cdot \mathbf{\Lambda}_n(\mathbf{r}') = \begin{cases} \frac{l_n}{A_n^+} & \mathbf{r} \in T_n^+ \\ -\frac{l_n}{A_n^-} & \mathbf{r} \in T_n^- \\ 0 & \text{otherwise} \end{cases}$$

Figure 2.1: The equations of vector RWG basis function and its divergence for a given common edge (red) of two triangular elements.

We substitute Eq. 2.15 into 2.14 and test all components of equation with the same RWG testing functions (Davidson, 2011) as in the equation shown below:

$$\langle \mathbf{f}, \mathbf{\Lambda}_m \rangle = \frac{l_m}{2}\left(\frac{1}{A_m^+} \iint\limits_{\mathrm{T}_m^+} \mathbf{f} \cdot \boldsymbol{\rho}_m^+ \, dS + \frac{1}{A_m^-} \iint\limits_{\mathrm{T}_m^-} \mathbf{f} \cdot \boldsymbol{\rho}_m^- \, dS \right) \cong \frac{l_m}{2}\left(\mathbf{f}(\mathbf{r}_m^{\mathrm{c}+}) \cdot \boldsymbol{\rho}_m^{\mathrm{c}+} + \mathbf{f}(\mathbf{r}_m^{\mathrm{c}-}) \cdot \boldsymbol{\rho}_m^{\mathrm{c}-}\right) \tag{2.16}$$

where $\mathbf{f}$ can be $\mathbf{A}$, $\nabla\varphi$, $\frac{\mathbf{J}_s}{\sigma t}$ or $\mathbf{E}^{\mathrm{inc}}$. The testing procedure results in a system of linear equations for the coefficients I_n which can be written as a matrix equation:

$$\left(\underline{\underline{\mathbf{Z}}} + \underline{\underline{\mathbf{B}}}\right)\underline{\mathbf{I}} = \underline{\mathbf{V}}^{\mathrm{inc}} \tag{2.17}$$

where the $N \times N$ matrix $\mathbf{Z}$ stores Eq. 2.18; $\mathbf{B}$ is the $N \times N$ correction matrix to the $\mathbf{Z}$'s near diagonal elements due to the impedance boundary condition and filled with Eq. 2.19; and $\mathbf{V}^{\mathrm{inc}}$ is a $N \times 1$ vector storing the tested primary field shown in Eq. 2.20:

$$Z_{mn} = j\omega\mu\left(\mathbf{A}_{mn}^+ \cdot \frac{\boldsymbol{\rho}_m^{\mathrm{c}+}}{2} + \mathbf{A}_{mn}^- \cdot \frac{\boldsymbol{\rho}_m^{\mathrm{c}-}}{2} + \phi_{mn}^- - \phi_{mn}^+\right) \tag{2.18}$$

$$B_{mn} = \frac{\mathbf{\Lambda}_n(\mathrm{r}_m^{\mathrm{c}+})}{\sigma(\mathbf{r}_m^{\mathrm{c}+})t(\mathbf{r}_m^{\mathrm{c}+})} \cdot \frac{\boldsymbol{\rho}_m^{\mathrm{c}+}}{2} + \frac{\mathbf{\Lambda}_n(\mathbf{r}_m^{\mathrm{c}-})}{\sigma(\mathbf{r}_m^{\mathrm{c}-})t(\mathbf{r}_m^{\mathrm{c}-})} \cdot \frac{\boldsymbol{\rho}_m^{\mathrm{c}-}}{2} \tag{2.19}$$

$$V_m^{\mathrm{inc}} = \mathbf{E}_m^{\mathrm{inc,c}+} \cdot \frac{\boldsymbol{\rho}_m^{\mathrm{c}+}}{2} + \mathbf{E}_m^{\mathrm{inc,c}-} \cdot \frac{\boldsymbol{\rho}_m^{\mathrm{c}-}}{2} \tag{2.20}$$

where

$$\mathbf{A}_{mn}^{\pm} = \iint\limits_S \mathbf{\Lambda}_n(\mathbf{r}') G_{\mathrm{R}}(\mathbf{r}_m^{\mathrm{c}\pm}, \mathbf{r}') \, dS' \tag{2.21}$$

$$\phi_{mn}^{\pm} = \frac{1}{k^2} \iint\limits_S \nabla' \cdot \mathbf{\Lambda}_n(\mathbf{r}') G_{\mathrm{R}}(\mathbf{r}_m^{c\pm}, \mathbf{r}') \, dS' \tag{2.22}$$

and the corresponding incident electric fields (Balanis, 2005) are given as:

$$E_r^{\mathrm{inc}} = E_\theta^{\mathrm{inc}} = 0 \tag{2.23}$$

$$E_\phi^{\mathrm{inc}} = M_{\mathrm{TX}} \frac{\omega\mu k \sin\theta}{4\pi|\mathbf{r} - \mathbf{r}'|}\left[1 + \frac{1}{jk|\mathbf{r} - \mathbf{r}'|}\right] e^{-jk|\mathbf{r}-\mathbf{r}'|} \tag{2.24}$$

where the fields are also multiplied with the rotation matrix to change to Cartesian coordinates. A Gaussian quadrature rule is applied to numerically solve the integral equations of Eq. 2.21 and 2.22. To avoid the singularity due to the Green's function, when $\mathbf{r}_m^{c\pm} = \mathbf{r}'$, the order of quadrature can be selected as 2, 4 and 6 (Fig. 2.2). To use the other orders of quadrature, the singularity in the center of a triangle can be avoided as shown in Kaur and Yilmaz (2011). In all presented results of this dissertation, the order of quadrature is selected to be 2.

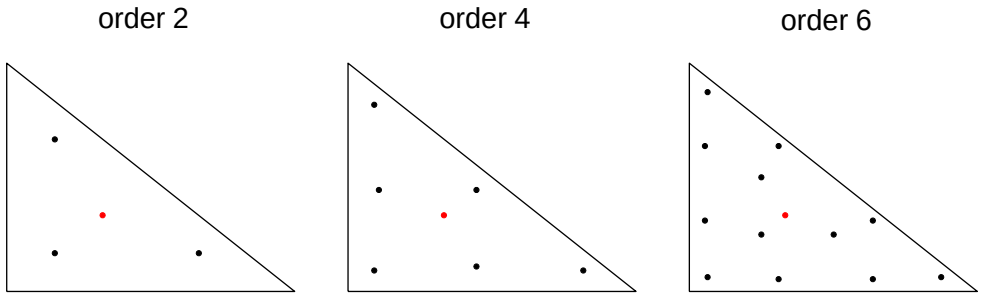

Figure 2.2: Gaussian quadrature of order 2, 4, and 6 for standard triangles: red dots are singularity points (center of triangles) and black dots are the points where integrals (Eqs. 2.21 and 2.22) are calculated.

The left-hand side of Eq. 2.17 is filled, factorized (LU-factorization) and stored for the next solution step. In the solution step, for each right-hand side of the same equation, unknowns are determined which are used to numerically compute $\mathbf{H}^{\text{sca}}$ with the following equation:

$$\mathbf{H}^{\text{sca}} = \iint_S \nabla G_{\text{R}}(\mathbf{r}, \mathbf{r}') \times \mathbf{J}_s(\mathbf{r}')\, dS' \tag{2.25}$$

where

$$\nabla G_{\text{R}}(\mathbf{r}, \mathbf{r}') = -\frac{G_{\text{R}}}{|\mathbf{r} - \mathbf{r}'|^2}(1 + jk|\mathbf{r} - \mathbf{r}'|)(\mathbf{r} - \mathbf{r}') \tag{2.26}$$

As in the matrix filling step, Gaussian quadrature of order 2 is used to solve the integral in Eq. 2.25.

2.2.2. Mesh Convergence

In this subsection, we are trying to understand the desired mesh density to get the required level of accuracy. The term λ is introduced which defines node spacing on the inner and outer circumferences of the circular fracture, e.g. the distance between two adjacent nodes on the circumference is equal to radius over λ. The node spacing factor, λ, is sampled in between 2 and 20. In Fig. 2.3, the absolute signal levels for small and large fracture sizes have been shown both for short and long spacing transmitter-receiver couples and for the node spacing factor of 20.

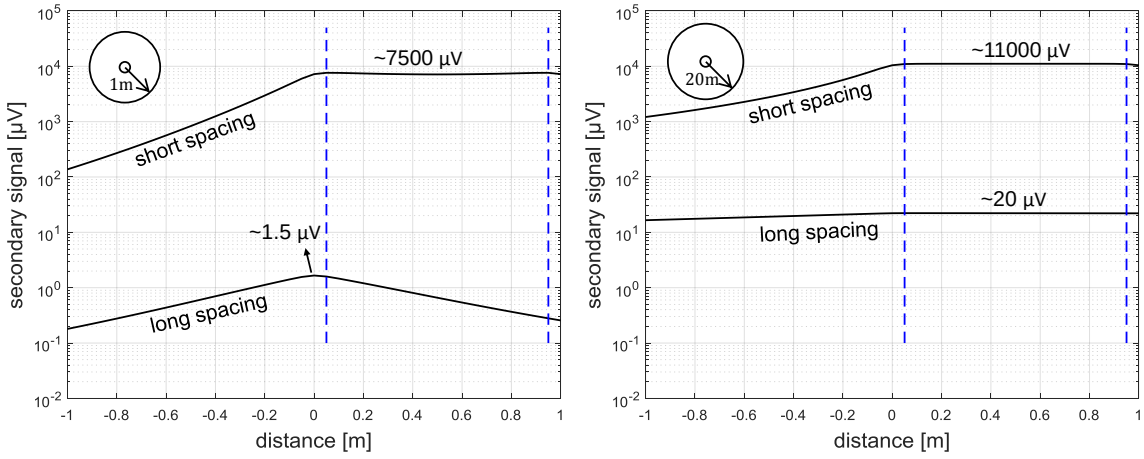

Figure 2.3: Absolute secondary signal levels for short ($l_{\mathrm{TR}} = 1$ m) and long ($l_{\mathrm{TR}} = 18$ m) spacing transmitter-receiver couples. Left and right plots show results for 1 m and 20 m outer radius orthogonal and circular fractures, respectively. In both cases, fracture inner radius is 6 cm, conductivity is 333 S/m and thickness is 5 mm; background (rock) conductivity is 0.333 S/m; tool is operated at 1 kHz frequency with transmitting magnetic dipole moment of 1500 A · m^2; cross-sectional area of receiver is 30 cm^2 and it has 600 turns.

The model with a division factor of 20 is the finest mesh and is selected to be the base case in the convergence analysis. The blue dashes in Fig. 2.3 show the interval where the values lying between those dashes are compared to the base case. The equation below defines the error in any iteration,

$$\epsilon = \frac{1}{N}\sqrt{\sum_{i=1}^{N}\left(U_{zz,i}^{\mathrm{sca}}(\lambda) - U_{zz,i}^{\mathrm{sca}}(20)\right)^2} \tag{2.27}$$

This error, ϵ, is shown in Fig. 2.4.

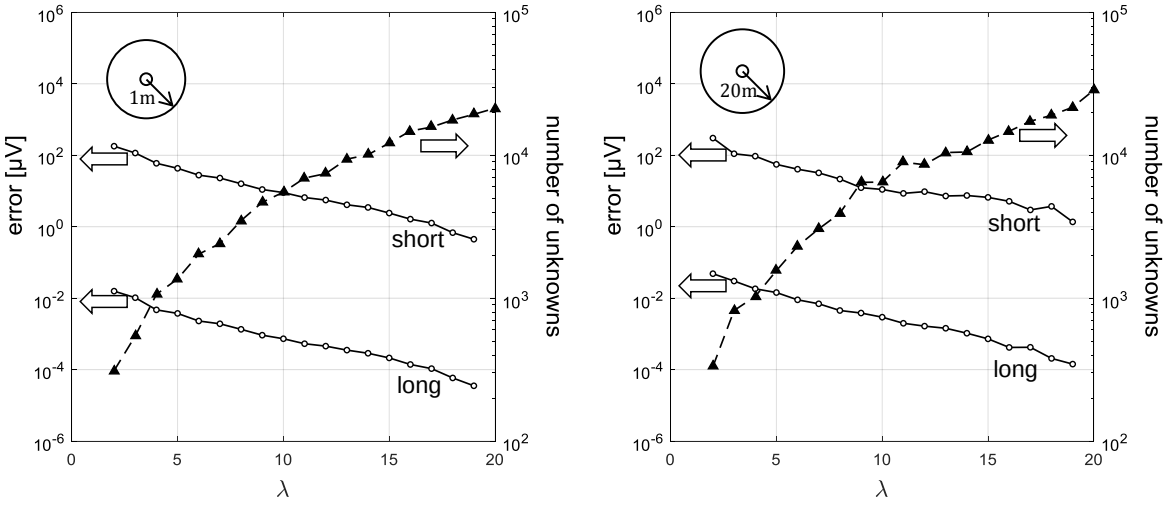

Figure 2.4: Convergence rate of the secondary signals with respect to the node spacing factor for short ($l_{\mathrm{TR}} = 1$ m) and long ($l_{\mathrm{TR}} = 18$ m) spacing transmitter-receiver couples. Left and right plots show results for 1 m and 20 m outer radius orthogonal and circular fractures, respectively. In both cases, fracture inner radius is 6 cm, conductivity is 333 S/m and thickness is 5 mm; background (rock) conductivity is 0.333 S/m; tool is operated at 1 kHz frequency with transmitting magnetic dipole moment of 1500 A · m^2; cross-sectional area of receiver is 30 cm^2 and it has 600 turns.

As it can be seen on the left plots of Fig. 2.3 and 2.4 the relative error is around 0.1% for short spacing and 0.05% for long spacing when the division factor is 10. This

relative error percentage further decreases for the right plots of Fig. 2.3 and 2.4 suggesting that coarser meshes can be used to minimize the computation time which will be a factor to consider when multiple runs are required such as in the inversion analysis.

2.2.3. Model Validation

The solution of surface integral equations is compared to analytical and numerical models. First, analytical equations for the scattered magnetic field are shown where a plane wave is propagating toward a PEC sphere, and then the same case is simulated with our numerical model. Later, scattered signals are computed for a representative fracture model and compared to the numerical results of Yang et al. (2015).

2.2.3.1. Fields Calculated for Conducting Sphere

In this section, an analytical solution for the scattering of a plane wave by a conducting sphere is presented and compared to the results of the numerical tool. Given the PEC sphere with radius a at the origin of a spherical coordinate system and a plane wave propagating in the positive z-direction (Fig. 2.4), the scattering magnetic field outside of the sphere can be calculated with the following equations:

$$H_r^{\mathrm{sca}} = H_0 \frac{\sin\phi}{j(kr)^2} \sum_{n=0}^{\infty} b_n n(n+1) \breve{H}_n^{(2)}(kr) P_n^1(\cos\theta) \tag{2.28}$$

$$H_\theta^{\mathrm{sca}} = -H_0 \frac{\sin\phi}{kr} \sum_{n=1}^{\infty} \left[a_n \breve{H}_n^{(2)}(kr) \frac{P_n^1(\cos\theta)}{\sin\theta} + b_n j \breve{H}_n^{(2)\prime}(kr) \frac{dP_n^1(\cos\theta)}{d\theta} \right] \tag{2.29}$$

$$H_\phi^{\mathrm{sca}} = -H_0 \frac{\cos\phi}{kr} \sum_{n=1}^{\infty} \left[a_n \breve{H}_n^{(2)}(kr) \frac{dP_n^1(\cos\theta)}{d\theta} + b_n j \breve{H}_n^{(2)\prime}(kr) \frac{P_n^1(\cos\theta)}{\sin\theta} \right] \tag{2.30}$$

where

$$a_n = -j^{-n} \frac{2n+1}{n(n+1)} \frac{\breve{J}_n'(ka)}{\breve{H}_n^{(2)\prime}(ka)} \tag{2.31}$$

$$b_n = -j^{-n}\frac{2n+1}{n(n+1)}\frac{\check{J}_n(ka)}{\check{H}_n^{(2)}(ka)} \tag{2.32}$$

A detailed explanation of these equations can be found in Jin (2010), subsection 7.4.3.

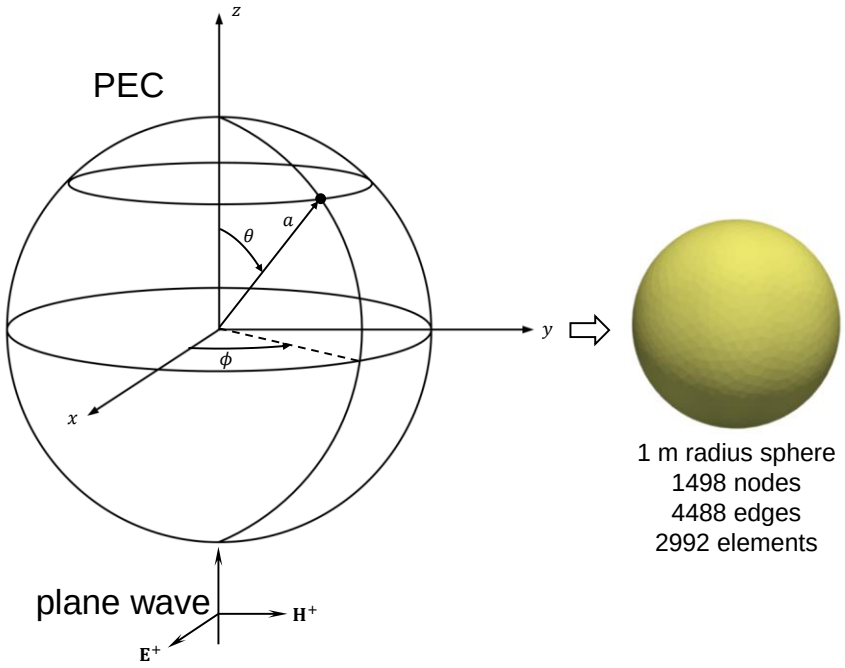

Figure 2.5: Plane wave scattering by a conducting sphere: a PEC sphere with radius a located at the center of spherical coordinate system and plane waves propagating in the positive z-direction; numerical surface discretization generated for the solver is shown to the right.

In the numerical calculations, to fill the vector $\underline{\mathbf{V}}^{\text{inc}}$, incident electric field is calculated with the following set of equations:

$$E_r^{\text{inc}} = E_0\frac{\cos\phi}{j(kr)^2}\sum_{n=0}^{\infty} j^{-n}(2n+1)\check{J}_n(kr)P_n^1(\cos\theta) \tag{2.33}$$

$$E_\theta^{\text{inc}} = E_0\frac{\cos\theta\cos\phi}{kr}\sum_{n=0}^{\infty} j^{-n}(2n+1)\check{J}_n(kr)P_n(\cos\theta) \tag{2.34}$$

$$E_\phi^{\text{inc}} = -E_0\frac{\sin\phi}{kr}\sum_{n=0}^{\infty} j^{-n}(2n+1)\check{J}_n(kr)P_n(\cos\theta) \tag{2.35}$$

For the comparison, the PEC sphere is selected to be 1 m in radius (Fig. 2.4), observer points are on the $r = 2$ m, $0 < \theta < \pi$ and $\phi = 90°$ line, the background is air (zero electrical conductivity), frequency is 100 MHz, and $E_0 = 1$ where $H_0 = E_0/\eta$. Fig. 2.6 shows results for both real and imaginary components of the scattered magnetic field. Note that since ϕ is selected to be 90 degrees, H_ϕ^{sca} is always zero as can be seen in Eq. 2.30. The sufficient level of the agreement obtained for both components of the magnetic field increases the confidence in the numerical tool. In the next subsection, further validation study is carried for the representative model and incident signals.

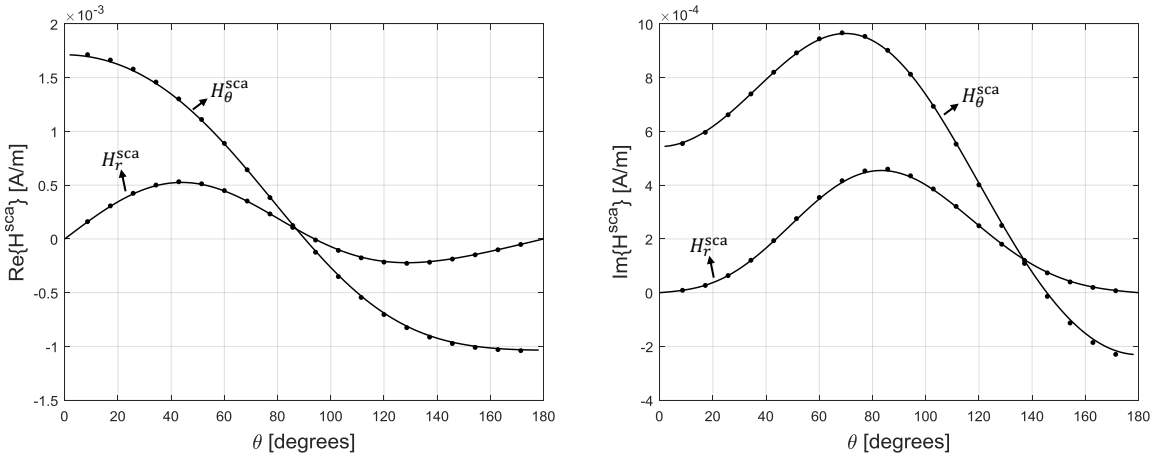

Figure 2.6: Comparison of analytical (solid line) and SIE solution (dots) of scattering from a meter radius PEC sphere; real (left) and imaginary (right) components of scattered magnetic fields are calculated for the observation points on the $r = 2$ m, $0 < \theta < \pi$ and $\phi = 90°$ line.

2.2.3.2. Numerical Results for a Representative Model

For the comparison, the iterative solution of the volume integral equations (Yang et al., 2015) has been used. The simulated orthogonal fracture model is a circle with an outer radius of 3 m, inner radius of 10 cm, thickness of 5 mm, and conductivity of 30 S/m. The background formation has a uniform conductivity of 0.333 S/m. The tool is

operated at 100 Hz frequency with 1500 $A \cdot m^2$ magnetic dipole moment on the transmitter coil. The receiver coil has 30 cm^2 cross-sectional area and 600 wire turns. The spacing between transmitter and receiver coil is 1.2 m.

In the generated volume mesh, there are 57,808 unknowns, and the solution for VIE is obtained in about 2 minutes with 512 parallel processors. There are 6420 unknowns in the generated surface mesh, and the solution for SIE is obtained in a minute with a single processor. Numerical results are shown in Fig. 2.7 where signal levels are shown with a solid line for the solution of surface integral equations (SIE) and absolute differences with the VIE are shown with dashed lines. For the real (blue) and imaginary (black) component of secondary signals it shows very good agreement for both numerical results, with a maximum discrepancy of less than 5%. It is important to note the significant dominance of real components over the imaginary signals.

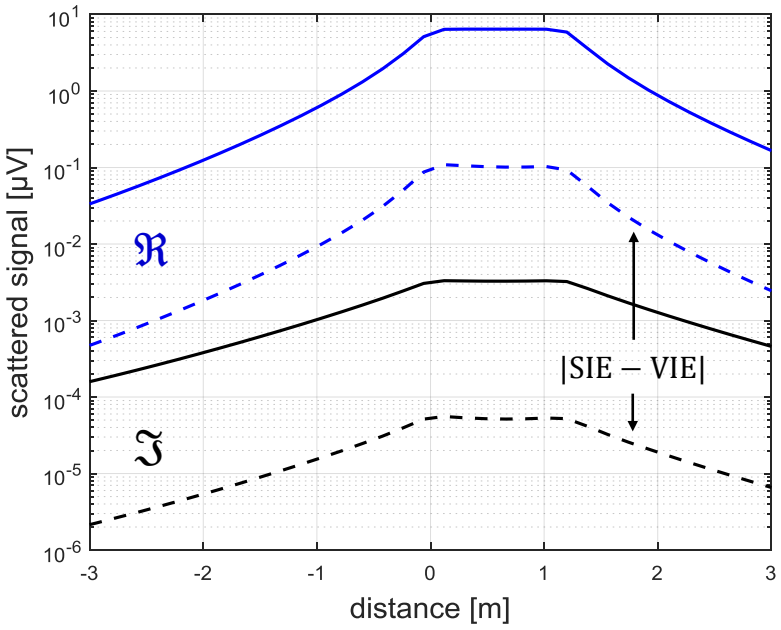

Figure 2.7: Comparison of SIE and VIE solutions of scattering from a representative fracture model; solid lines show the real (blue) and imaginary (black) components of absolute secondary (scattered) signals for the SIE solution; dashed lines show the absolute differences between both solutions.

2.2.4. In-Phase and Quadrature Components of Signals

Following the observation made in the previous section (high ratio of real and imaginary components), in this section, the parameters affecting this ratio are investigated. Fig. 2.8 shows the signal levels at the middle of the hump (Fig. 2.7) for the different conductivity of fracture and background formation at the operating frequency of 1 kHz. The fracture conductivity ranges between 10 and 10^4 S/m, and the background conductivity ranges between 10^{-2} and 1 S/m. The fracture is 1 m in radius and is assumed to be an orthogonal circle with 10 cm of inner radius and 5 mm thickness. The magnetic dipole moment of the transmitter coil is 1500 $A \cdot m^2$. The receiver coil has 30 cm^2 cross-sectional area and 600 wire turns. The spacing between the transmitter and receiver coil is 1 m.

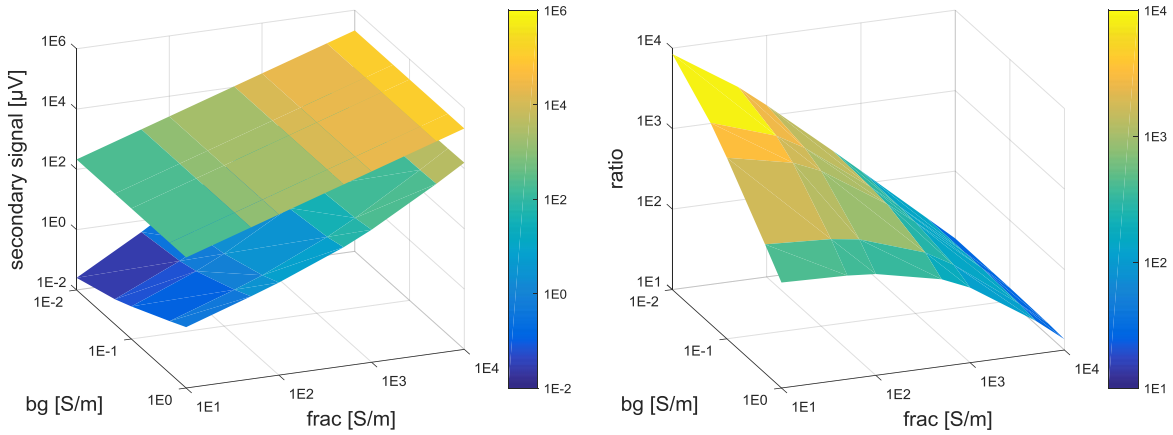

Figure 2.8: The relationship between real and imaginary components of secondary signals with changing background (bg) and fracture (frac) conductivity: left plot shows both real and imaginary components on upper and lower surfaces, respectively; right plot shows the ratio between them.

An increase in the background conductivity does not affect the real component; however, it increases the imaginary component of the signal. An increase in the fracture conductivity increases both real and imaginary components. The ratio between them $|\Re(U^{\mathrm{sca}})/\Im(U^{\mathrm{sca}})|$ stays above 10 for the selected region clearly showing the dominance of real components in the absolute signals. This may lead to a simplification in the forward model which is described in the next subsection.

2.2.5. Approximation of Surface Currents

In the previous section, the dominance of the real component is shown for an operating frequency of 1 kHz. If the magnitude of the signal is of interest, then the accurate calculation of only the real component is sufficient for the detailed analysis. It can be achieved with the simplification in the boundary condition shown in Eq. 2.12. If the scattered electric field is eliminated surface currents can be approximated as follows:

$$\mathrm{J}_{\boldsymbol{s}} \approx -\hat{\mathrm{n}} \times \hat{\mathrm{n}} \times \boldsymbol{G}\mathrm{E}^{\mathbf{inc}} \tag{2.36}$$

This procedure does not require inversion of the matrices and reduces computational time. The accuracy level is shown for orthogonal and rotated fracture models with metallic conductivity (the conductivity and thickness of 34.6 MS/m and 25.4 μm, respectively) and smaller size (this type of model is used in the next chapter). Transmitter coil is operated at 1 kHz frequency, and the magnetic dipole moment is $12\ \mathrm{A}\cdot\mathrm{m}^2$; receiver coil has the cross section of 30 cm^2 with 600 turns. The background has zero conductivity and the distance between transmitter and receiver coils is 1 m. Fig. 2.9 shows secondary signal magnitude for co-axial coil configuration and 10 cm radius orthogonal fracture. The relative error introduced due to the surface current approximation is always less than 1% along the sampling interval.

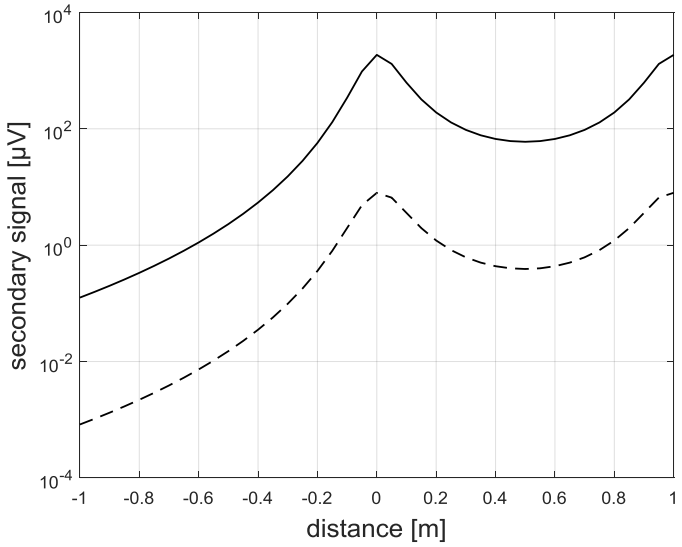

Figure 2.9: Magnitude of secondary signals when surface currents are approximated: solid line shows the full SIE solution; dashed line shows the difference between the approximation-based solution and full computation. The fracture model is orthogonal and coils are in co-axial configuration.

Fig. 2.10 shows secondary signal magnitude for the co-axial (left) and cross-polarized (right) coil configurations and for 20 cm radius fracture rotated 30˚ about the *x*-

axis. The relative error introduced due to the surface current approximation is always less than 10% for the co-axial coil configuration. For the cross-polarized configuration, however, approximation simulates the trend only; there is a poor quantitative match.

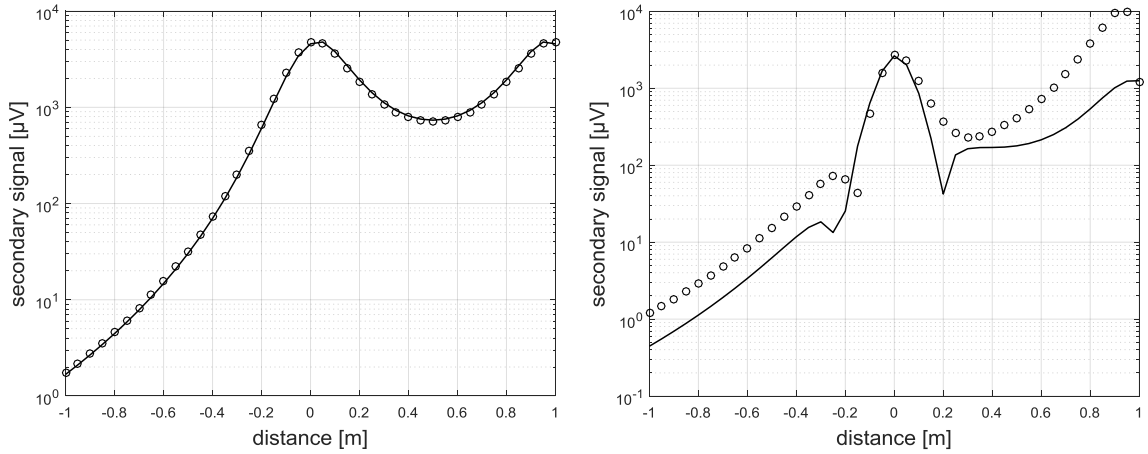

Figure 2.10: Magnitude of secondary signals when surface currents are approximated: solid line shows the full SIE solution; and circle markers show the approximation based solution. The fracture model is rotated and coils are in co-axial (left) and cross-polarized (right) configurations.

2.2.6. Computational Time

In this section, the computational time required for a typical run is explored. Fig. 2.11 shows the time required for the full numerical solution of SIE with an impedance boundary condition. Its solution has two stages: filling the impedance matrix and solving it for every excitation point. The first step dominates the computation time because integral equations yield a full matrix. LU-factorization of the matrix occurs once in a typical run, hence, for multiple excitation points, the total sampling time (factorization + solution for all excitations) is divided by the number of excitation points which is equal to 82 in this case. This step can be further accelerated by using numerical iterative solvers or parallelization.

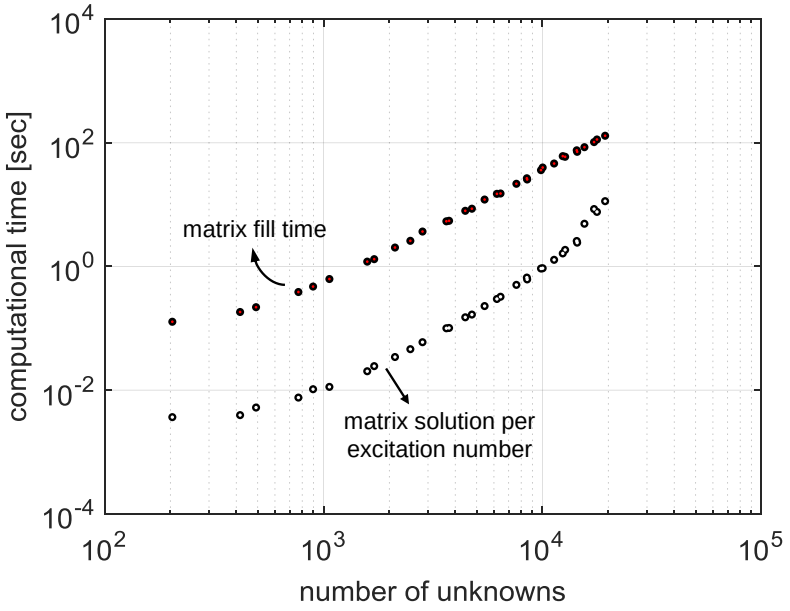

Figure 2.11: Computation time for the different number of surface unknowns: red filled circles show matrix fill-times which includes the application of impedance boundary condition as well, and empty circles show matrix solution times for each sampling point.

A typical run for the fracture size of 20 m yields 5,000-10,000 unknowns with λ being equal to 10. This problem can be solved in a minute. For the inversion analysis, the speed will be further increased by using coarser meshes.

2.3. Simulation of Induction Tool Response in Production Casing

In this computation, the set of 2D problems emerging from the Fourier series expansion is solved with an axial hybrid method where the wellbore axis (z-axis) is solved numerically and the radial part is solved analytically. After solving the generalized eigenvalue problem, normalized Bessel and Hankel functions are used to describe the fields in the radial direction. Amplitude and slope basis functions are defined over the discretized wellbore axis which allows the use of a coarse grid everywhere along the axis. This eliminates the need to refine the grid in the vicinity of the fracture. Before

proceeding to the numerical results, the detailed steps of the computation are shown below (Wang et al., 2009), and the results are compared to that of the surface integral equations.

2.3.1. Axial Hybrid Method

In any radial layer, the electric and magnetic fields in the z-direction can be expressed with the following governing equations:

$$\nabla_s^2 E_z + \frac{\partial}{\partial z}\sigma_s^{-1}\frac{\partial}{\partial z}\sigma_z E_z - j\omega\mu_o\mu_{r,s}\sigma_z E_z = \nabla_s \cdot (\mathbf{M}_s \times \hat{z}) \tag{2.37}$$

and

$$\nabla_s^2 H_z + \frac{\partial}{\partial z}\mu_{r,s}^{-1}\frac{\partial}{\partial z}\mu_{r,z} H_z - j\omega\mu_o\sigma_s\mu_{r,z} H_z = \sigma_s M_z - \frac{1}{j\omega\mu_o}\frac{\partial}{\partial z}\mu_{r,s}^{-1}\nabla \cdot \mathbf{M} \tag{2.38}$$

where the subscript s designates the transverse component and z shows the wellbore direction. Excluding the source terms in the above equations they can both be written in the following form:

$$\nabla_s^2 p_\eta^{-1} f_\eta + \frac{\partial}{\partial z} q_\eta^{-1}\frac{\partial f_\eta}{\partial z} + k_\eta^2 p_\eta^{-1} f_\eta = 0 \tag{2.39}$$

where $f_\eta = \{\sigma_z E_z, \mu_{r,z} H_z\}$, $p_\eta = \{\sigma_z, \mu_{r,z}\}$, $q_\eta = \{\sigma_s, \mu_{r,s}\}$, $k_\eta^2 = -j\omega\mu_o\{q_h p_e, q_e p_h\}$ and $\eta = \{e, h\}$. The ϕ variation of f_η is expressed in terms of a Fourier series. The solution of ρ dependence is obtained after solving the generalized eigenvalue problem, and it is in the form of a combination of normalized Bessel functions of the first kind $\hat{J}_n$ and the normalized Hankel function $\widehat{H}_n^{(1)}$. To solve the z dependence, basis functions are defined over one-dimensional elements along the z-axis. Local shape functions of each element are defined in the interval of (z_n, z_{n+1}) as follows:

$$L_1 = \frac{z_{n+1} - z}{z_{n+1} - z_n} \tag{2.40a}$$

$$L_2 = \frac{z - z_n}{z_{n+1} - z_n} \tag{2.40b}$$

and all elements, except the first and last one, have four basis functions defined as follows:

$$g_{\eta,1}(z) = -2L_1^3 + 3L_1^2 \tag{2.41a}$$

$$g_{\eta,2}(z) = q_\eta(z)\Delta z(z)L_1^2 L_2 \tag{2.41b}$$

$$g_{\eta,3}(z) = -2L_2^3 + 3L_2^2 \tag{2.41c}$$

$$g_{\eta,4}(z) = -q_\eta(z)\Delta z(z)L_2^2 L_1 \tag{2.41d}$$

Fig. 2.12 shows these basis functions (Eq. 2.41) when q_η is unity. For the first element only 2.41c, d and for the last element only 2.38 a, b are defined. Each basis function is non-zero over two neighbor elements; $g_{\eta,1}$ and $g_{\eta,2}$ are non-zero on the neighbor element in the negative z-direction, and $g_{\eta,3}$ and $g_{\eta,4}$ are non-zero on the neighbor element in the positive z-direction. Hence, if we have N_n number of nodes, we get $N_e = N_n - 1$ number of elements and $N = 2(N_n - 2)$ total number of basis functions.

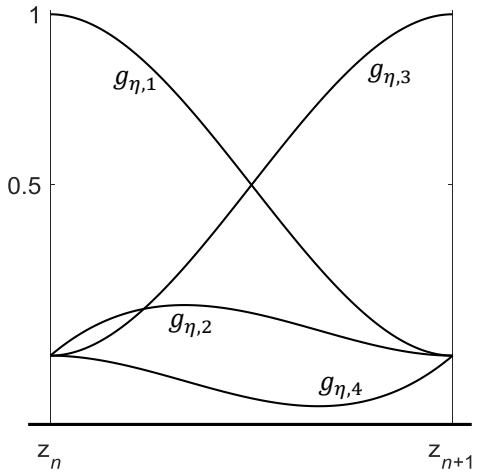

Figure 2.12: Basis functions defined over a one-dimensional element along the wellbore axis; relative permeability of one is used.

The solution of Eq. 2.39 is obtained after solving the generalized eigenvalue problem which is defined with the following equation:

$$\mathbf{A}_\eta \mathbf{C}_\eta = \mathbf{B}_\eta \mathbf{C}_\eta \mathbf{\Lambda}_\eta^2 \tag{2.42}$$

where $\mathbf{C}_\eta$ is the matrix of eigenvectors, $\mathbf{\Lambda}_\eta$ is the diagonal matrix of eigenvalues and $\mathbf{A}_\eta$ and $\mathbf{B}_\eta$ are defined as:

$$\mathbf{A}_\eta = -\int_{-\infty}^{\infty} \frac{1}{q_\eta} \frac{\partial \mathbf{g}_\eta(z)}{\partial z} \frac{\partial \mathbf{g}_\eta^t(z)}{\partial z} dz + \int_{-\infty}^{\infty} \frac{k_\eta^2}{p_\eta} \mathbf{g}_\eta(z) \mathbf{g}_\eta^t(z) dz \tag{2.43}$$

and

$$\mathbf{B}_\eta = \int_{-\infty}^{\infty} \frac{1}{p_\eta} \mathbf{g}_\eta(z) \mathbf{g}_\eta^t(z) dz \tag{2.44}$$

Integrals in Eq. 2.43 and 2.44 are solved analytically for each element. $\mathbf{A}_\eta$ and $\mathbf{B}_\eta$ are six-diagonal matrices and $N \times N$ in dimensions. It should be emphasized that the orthogonality relationship still holds for the numerical eigenmodes. Hence, the following equation must be satisfied:

$$\mathbf{C}_{\eta}^{t}\mathbf{B}_{\eta}\mathbf{C}_{\eta} = \mathbf{I} \tag{2.45}$$

Now, the solution to Eq. 2.39 for each layer can be expressed in the form of basis functions (Eq. 2.41), eigenvalues and eigenvectors (Eq. 2.42), and normalized Bessel and Hankel functions. Then, in each radial boundary, local transmission and reflection matrices are defined as:

$$\mathbf{T}_{l,l\pm1} = \left[\boldsymbol{\beta}_{(l\pm1)\mp}^{\pm} - \boldsymbol{\beta}_{(l)\pm}^{\mp}\mathbf{P}_{l,\underline{l\pm1}}\right]^{-1}\left[\boldsymbol{\beta}_{(l)\pm}^{\pm} - \boldsymbol{\beta}_{(l)\pm}^{\mp}\right] \tag{2.46}$$

and

$$\mathbf{R}_{l,l\pm1} = \mathbf{P}_{l,\underline{l\pm1}}\mathbf{T}_{l,l\pm1} - \mathbf{I} \tag{2.47}$$

where l represents the number of layer. In the above,

$$\boldsymbol{\beta}_{(k)\pm}^{\pm} = \begin{pmatrix} -j\dfrac{n}{\rho}\mathbf{D}_{he,l,k} & j\omega\mu_{\mathrm{o}}\mathbf{P}_{h,\underline{l},k}\boldsymbol{\chi}_{h,(k)\pm}^{\pm}\boldsymbol{\Lambda}_{h,k} \\ -\mathbf{P}_{e,\underline{l},k}\boldsymbol{\chi}_{e,(k)\pm}^{\pm}\boldsymbol{\Lambda}_{e,k} & -j\dfrac{n}{\rho}\mathbf{D}_{eh,l,k} \end{pmatrix}\boldsymbol{\Lambda}_{k}^{-2} \tag{2.48}$$

and

$$\mathbf{P}_{\eta,l,\underline{k}} = \mathbf{C}_{\eta,l}^{t}\int_{-\infty}^{\infty}\frac{1}{p_{\eta,k}}\mathbf{g}_{\eta,l}\mathbf{g}_{\eta,k}^{t}dz\,\mathbf{C}_{\eta,k} \tag{2.49}$$

$$\mathbf{P}_{\eta,\underline{l},k} = \mathbf{C}_{\eta,l}^{t}\int_{-\infty}^{\infty}\frac{1}{p_{\eta,l}}\mathbf{g}_{\eta,l}\mathbf{g}_{\eta,k}^{t}dz\,\mathbf{C}_{\eta,k} \tag{2.50}$$

$$\mathbf{D}_{he,l,k} = \mathbf{C}_{h,l}^{t}\int_{-\infty}^{\infty}\frac{1}{p_{h,l}q_{e,k}}\mathbf{g}_{\eta,l}\frac{\partial}{\partial z}\mathbf{g}_{\eta,k}^{t}dz\,\mathbf{C}_{e,k} \tag{2.51}$$

$$\mathbf{D}_{eh,l,k} = \mathbf{C}_{e,l}^{t}\int_{-\infty}^{\infty}\frac{1}{p_{e,l}q_{h,k}}\mathbf{g}_{e,l}\frac{\partial}{\partial z}\mathbf{g}_{h,k}^{t}dz\,\mathbf{C}_{h,k} \tag{2.52}$$

where $k = l$ or $l \pm 1$. Note that when $k = l$ $\mathbf{P}_{\eta,l,\underline{k}} = \mathbf{I}$ and $\mathbf{P}_{\eta,\underline{l},k} = \mathbf{I}$. In the outermost layer, there is no incoming wave. Starting with this we can calculate a generalized reflection matrix at the wellbore $\mathbf{Q}_{1}^{+}$ by using recursive relationships:

$$\mathbf{S}_{m,m+1} = \left[\mathbf{I} - \mathbf{R}_{m+1,m}\mathbf{Q}_{(m+1)-}^{+}\right]^{-1}\mathbf{T}_{m,m+1} \tag{2.53}$$

$$\mathbf{Q}^{+}_{(m)+} = \mathbf{R}_{m,m+1} + \mathbf{T}_{m+1,m}\mathbf{Q}^{+}_{(m+1)-}\mathbf{S}_{m,m+1} \tag{2.54}$$

along with the propagation relationship:

$$\mathbf{Q}^{+}_{m}(\rho_a) = \boldsymbol{\gamma}^{-}_{m}(\rho_a,\rho_b)\mathbf{Q}^{+}_{m}(\rho_b)\boldsymbol{\gamma}^{+}_{m}(\rho_a,\rho_b) \tag{2.55}$$

where

$$\boldsymbol{\gamma}^{+}_{m}(\rho_a,\rho_b) = e^{-j\boldsymbol{\Lambda}_m(\rho_b-\rho_a)}\frac{\widehat{\mathbf{H}}^{(1)}_{n}(\boldsymbol{\Lambda}_m\rho_b)}{\widehat{\mathbf{H}}^{(1)}_{n}(\boldsymbol{\Lambda}_m\rho_a)} \tag{2.56}$$

$$\boldsymbol{\gamma}^{-}_{m}(\rho_a,\rho_b) = e^{-j\boldsymbol{\Lambda}_m(\rho_b-\rho_a)}\frac{\hat{\mathbf{J}}_{n}(\boldsymbol{\Lambda}_m\rho_a)}{\hat{\mathbf{J}}_{n}(\boldsymbol{\Lambda}_m\rho_b)} \tag{2.57}$$

For the magnetic dipole oriented in the wellbore direction and when $\rho' = \rho_{\mathrm{TX}} = \rho_{\mathrm{RX}}$:

$$\mathbf{b}_h = \frac{jM_{\mathrm{TX}}}{4p_{h,1}(z_{\mathrm{TX}})}\widehat{\mathbf{H}}^{(1)}_{n}\left(\boldsymbol{\Lambda}_{h,1}\rho'\right)\hat{\mathbf{J}}_{n}\left(\boldsymbol{\Lambda}_{h,1}\rho'\right)\boldsymbol{\Lambda}^{2}_{h,1}\mathbf{C}^{t}_{h,1}\mathbf{g}_{h,1}(z_{\mathrm{TX}}) \tag{2.58}$$

and magnetic field will be given by:

$$H^{\mathrm{inc}}_{z} = \frac{1}{p_{h,1}(z_{\mathrm{RX}})}\mathbf{g}^{t}_{h,1}(z_{\mathrm{RX}})\mathbf{C}_{h,1}\mathbf{b}_h \tag{2.59}$$

$$H^{\mathrm{sca}}_{z} = \frac{1}{p_{h,1}(z_{\mathrm{RX}})}\mathbf{g}^{t}_{h,1}(z_{\mathrm{RX}})\mathbf{C}_{h,1}\mathbf{Q}^{+}_{h,1}\mathbf{b}_h \tag{2.60}$$

As in the previous method, Eq. 2.59 and 2.60 are solved for different excitation points.

2.3.2. Numerical Validation

The simulated orthogonal fracture model is a circle with the outer radius of 8 m, inner radius of 10 cm, thickness of 5 mm and conductivity of 333 S/m. The background (rock) formation has a uniform conductivity of 0.333 S/m. The tool is operated at 1 kHz frequency with 1500 A · m^2 magnetic dipole moment on the transmitter coil. The receiver coil has 30 cm^2 cross-sectional area and 600 turns. The spacing between transmitter and receiver coils is 1.2 m for the short spacing and 17.8 m for the long coil spacing. For the

method of moments, the total computation time is 70 seconds with 8220 unknowns and 82 sampling points.

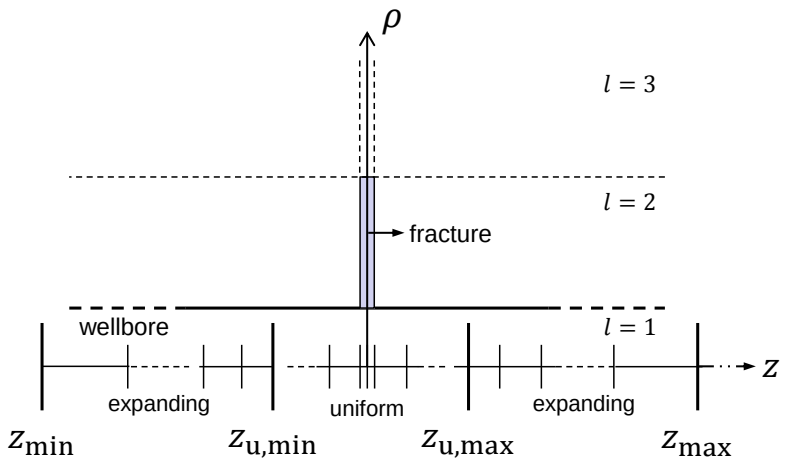

Figure 2.13: Meshing and radial layering scheme used in the axial hybrid method for the computation of fracture scattering in an open-hole completion.

The gridding scheme used in the mode matching technique is shown in Fig. 2.13. A uniform grid is implemented between -2 and 2 m with an element size of 10 cm. The 5 mm thickness of fracture is an additional orthogonal layer. The domain is truncated at 150 m on both expanding parts of the grid with a 1.25 length ratio between two adjacent elements. The total number of basis functions is 274. The solution with 82 sampling points and with this gridding schemes is obtained in 10 seconds.

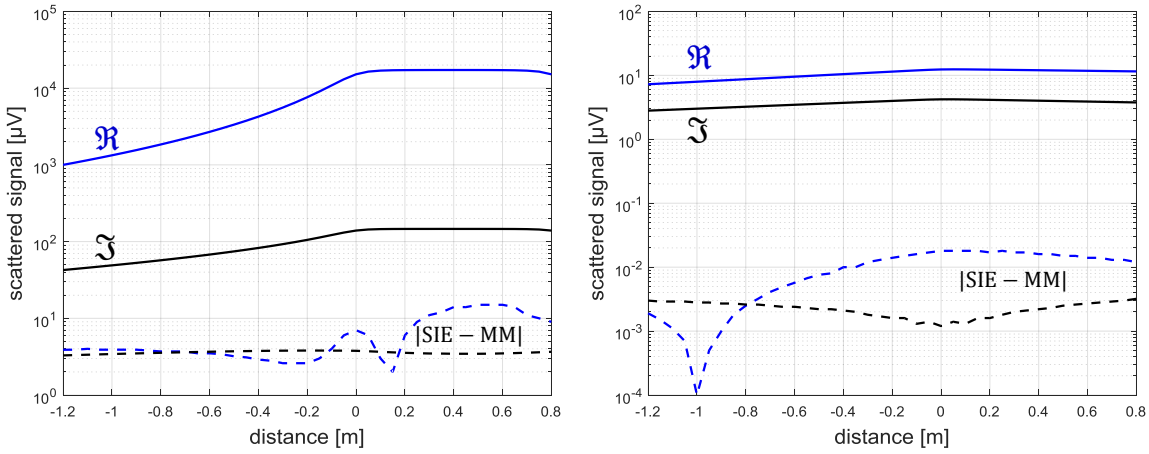

Figure 2.14: Comparison of MM and SIE solution of fracture scattering measured with short spacing (left plot) and long spacing (right plot) couples; solid lines show the real (blue) and imaginary (black) components of absolute secondary (scattered) signals for the SIE solution; dashed lines show the absolute difference between both solutions.

Numerical results are shown in Fig. 2.14 where signal levels are shown with a solid line for the solution of surface integral equations (SIE) and absolute differences with the mode matching (MM) are shown with dashed lines. For the real (blue) and imaginary (black) component of secondary signals, Fig. 2.14 shows very good agreement for both short and long spacing couples, with a maximum discrepancy of less than 3% for the peak signals.

2.3.3. Effect of Electromagnetic Properties of Casing on Differential Signals

An additional radial layer is added to the previously used scheme to include production casing material properties. Fig. 2.15 shows the meshing and layering scheme used for understanding the effect of the casing electrical conductivity and magnetic permeability on the scattered field from the fracture. The fracture is an additional layer orthogonal to the wellbore axis with the radius of 8 m, thickness of 5 mm and conductivity of 333 S/m (conductivity anywhere else is 0.333 S/m). The inner and outer

radius of the casing pipe is 6.2 and 7 cm, respectively. The wellbore axis is discretized from -15 and 15 m, where the uniform part of the meshing is between -2 and 2 m with the ratio of element size of 1.25 in the expanding part. The total number of basis functions is 230. The tool operating frequency is 1 kHz and the transmitter magnetic dipole moment is $1500\,\mathrm{A}\cdot\mathrm{m}^2$. The number of turns on the receiver is 600 with 30 cm^2 cross-sectional area. The spacings between the transmitter and receiver coils are 1.2 and 1.5 m.

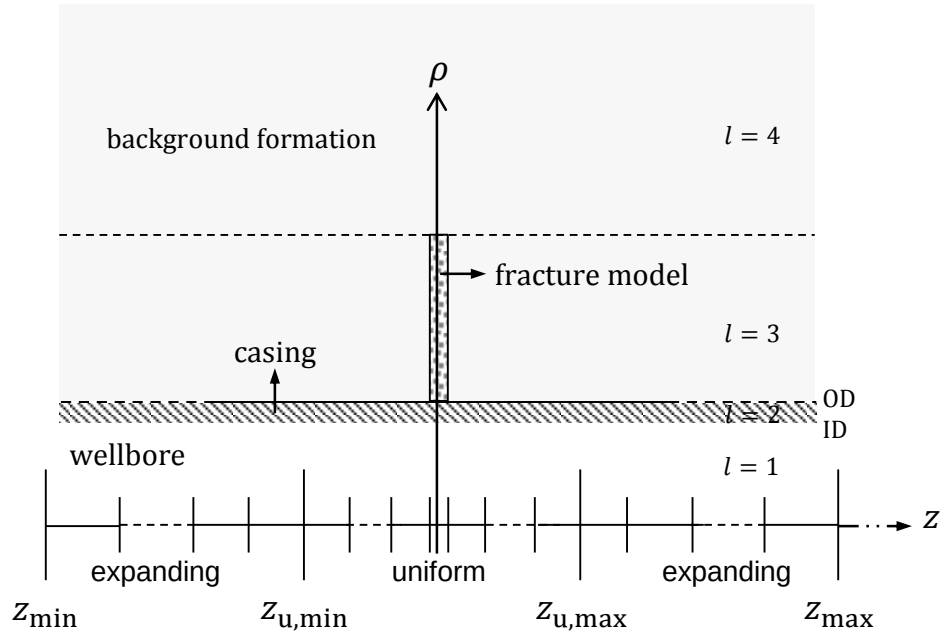

Figure 2.15: Meshing and radial layering scheme used in the axial hybrid method for the computation of fracture scattering in a cased-hole completion.

Fig. 2.16 shows the short spacing differential signals when the electrical conductivity of the casing pipe increases from 10^1 to 10^5 S/m, and the relative magnetic permeability is one. Fig. 2.17 shows the same signals when the relative magnetic permeability of the casing pipe increases from 1 to 30, and the electrical conductivity is 10^5 S/m. The left column plots show the differential signals from the casing (no-frac case), and the right column plots show the differential signals from the fracture

(subtraction of frac and no-frac cases). For the given tool parameters and 0.333 S/m background (rock) conductivity, the real and imaginary components of incident signals are ~$4.4 \cdot 10^3$ μV and $3.4 \cdot 10^6$ μV, respectively.

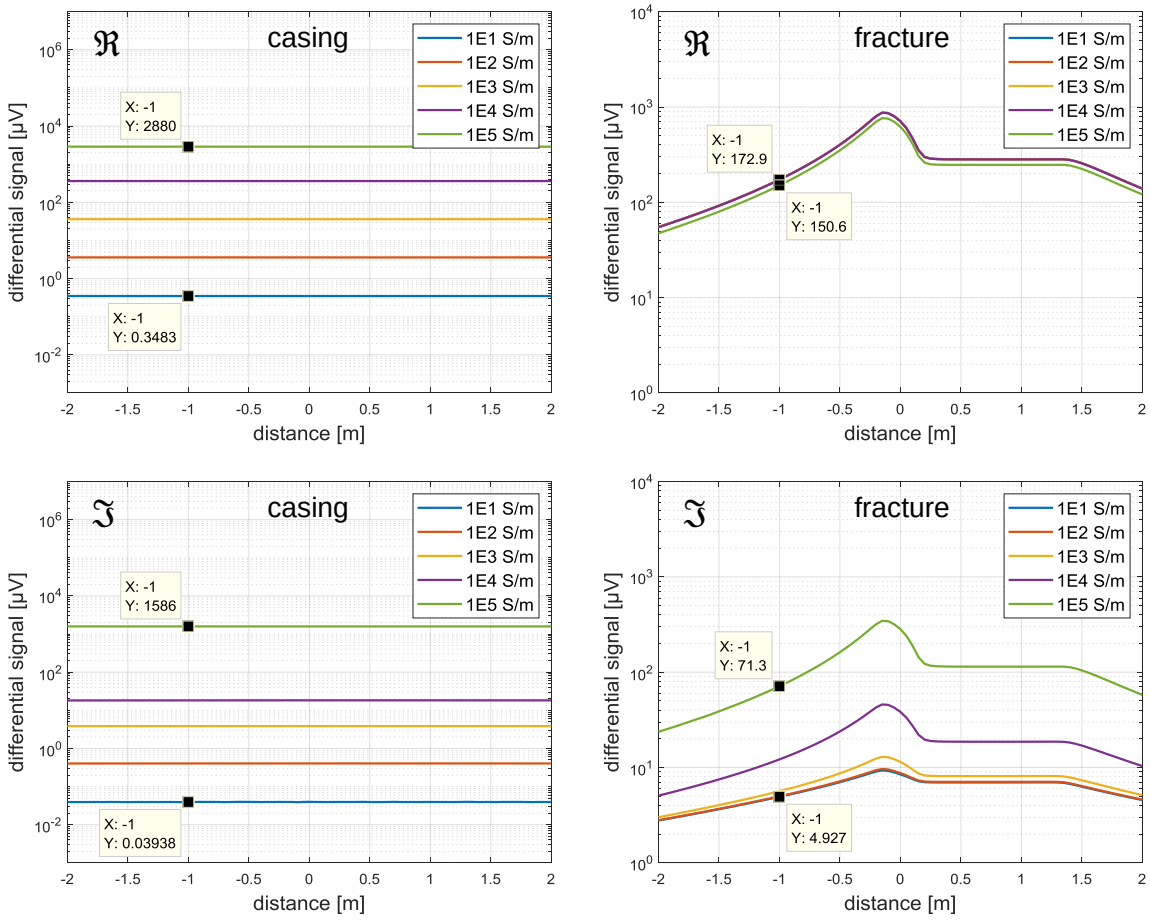

Figure 2.16: The effect of electrical conductivity of casing on the differential signals: left and right columns show differential signals for casing and fracture; and upper and lower plots show real and imaginary components of differential signals, respectively.

The increase in the electrical conductivity causes the scattered voltages from the casing to increase significantly suppressing the comparatively small fracture scattered voltages. For the 10^4 times increase in the electrical conductivity, real and imaginary

components of primary signals increase ~10^4 and ~$4{\cdot}10^4$, respectively. The real components of the differential signals due to scattering by the fracture, however, are not affected by the increase. The imaginary components of fracture differential signals are increased ~15 times and get closer to the level of the real components.

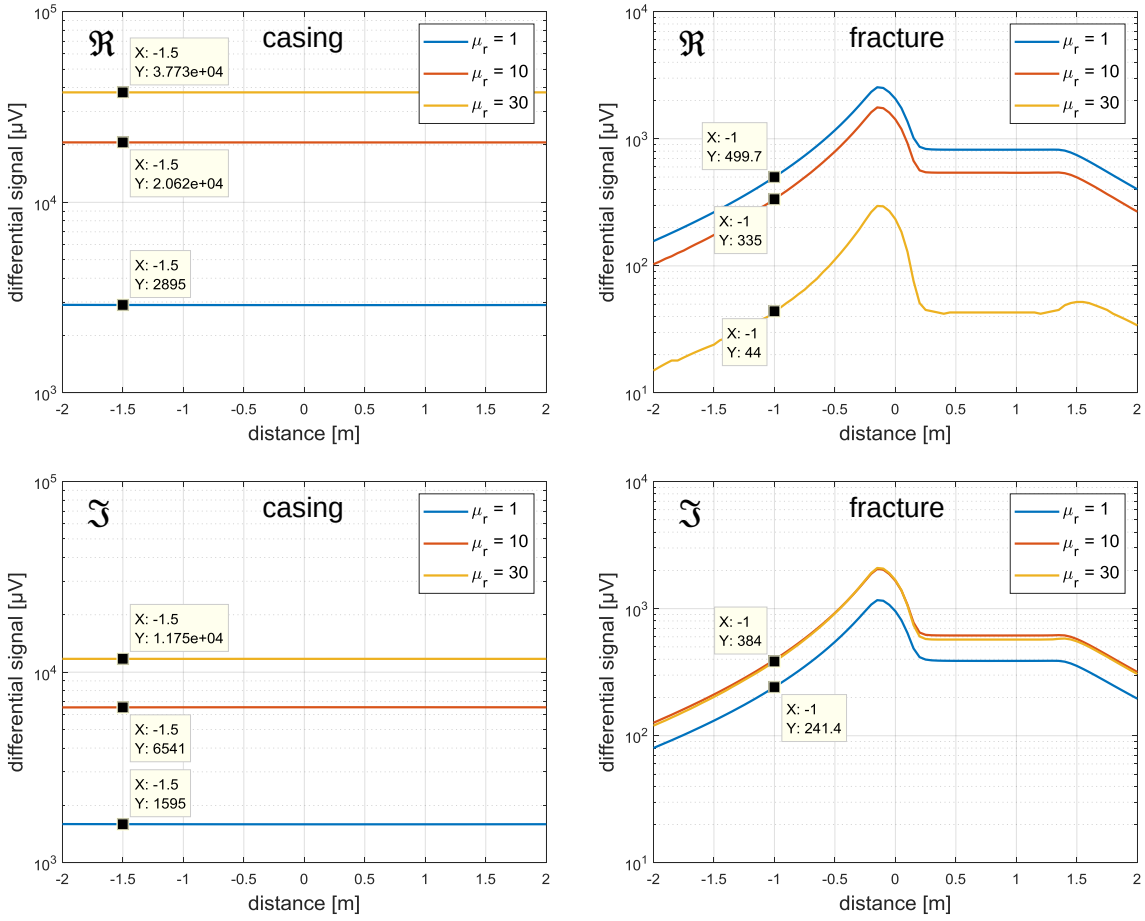

Figure 2.17: The effect of magnetic permeability of casing on the differential signals: left and right columns show differential signals for casing and fracture; and upper and lower plots show real and imaginary components of differential signals, respectively.

The same observation is made for the relative magnetic permeability increase which causes a significant increase in the primary signals. For the 30 times increase in the

relative magnetic permeability, real and imaginary components of primary signals are increased ~15 and ~8 times, respectively. The real components of the differential signals due to the fracture scattering, however, are decreased ~11 times and there is only a slight increase (~1.6 times) in the imaginary components.

2.3.4. Computational Time

In this section, the computational time required for different runs are reported. Fig. 2.18 shows the time requirement for the solution steps of axial hybrid method for the different number of basis functions. The first step is the solution of the generalized eigenvalue problem; the second is the calculation of the generalized refraction matrix; and the third step is the solution for the scattered signals at different sampling points. As indicated previously, a typical run can be completed with a few hundred basis functions.

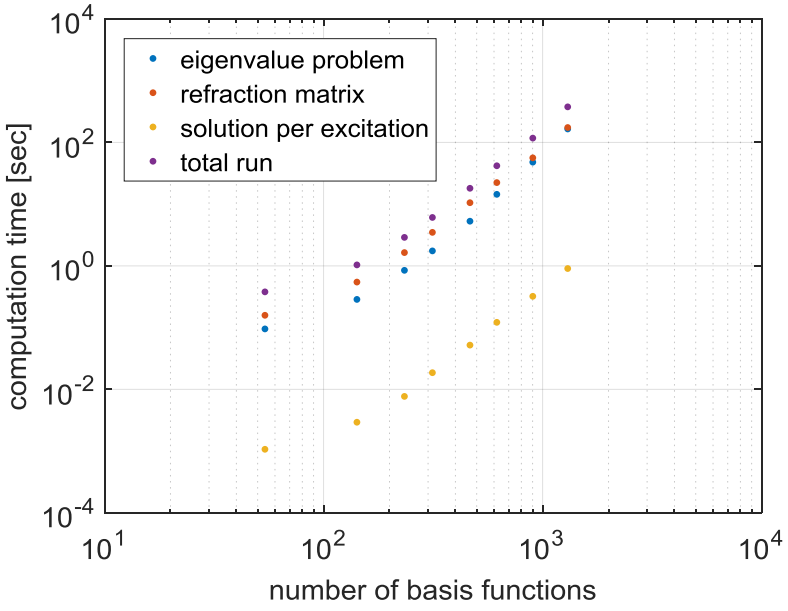

Figure 2.18: Computation time for different number of basis functions: blue dots show the generalized eigenvalue solution time for all layers; red dots show the generalized refraction matrix solution time; orange dots show the solution time for each sampling point and purple dots show the total run time for all 41 sampling points.

2.4. CONCLUSION

In this chapter, the formulation and numerical schemes are presented. The numerical results are validated and the computational requirements for a typical fracture simulation are reported. The models allow us to include all the possible variations in electromagnetic properties inside and outside the fracture. An open-hole application of the induction tool can be best modeled with integral equations where the effect of fracture shape factor and rotation about the wellbore axis can be captured. A hybrid method can provide very time efficient results when the induction tool is logged inside the casing. The model development was done using Matlab and the codes are provided in the appendix of this dissertation. The key findings are:

- The method of moment solution of surface integral equations provides very accurate results with the node spacing less than ten and a typical run takes about one minute when a single core is used for the computation.
- The fracture is simulated as an impedance sheet and all the permittivity and conductivity variation can be handled using this simulation. Since it is fast and includes all relevant fracture parameters, it is better suited for use with the inversion analysis presented in Chapter 4.
- The axial hybrid method may easily include the variation in all electromagnetic properties of the media; heterogeneous background formation conductivity and production casing properties can be handled. A typical run can be conducted with a few hundred basis functions and the total run-time is a few seconds.
- The scattered fracture signals at 10^5 S/m casing conductivity and 30 relative magnetic permeability is tiny compared to the scattered casing signals making it very challenging to detect fractures in cased-hole applications when using induction tools.

2.5. NOMENCLATURE

Symbol	definition	Unit
$\mathbf{E}$	electric field	V-m
$\mathbf{H}$	magnetic field	A-m
$\mathbf{J}$	electric current density	A-m^2
$\mathbf{J}_s$	surface electric current density	A-m
$\mathbf{M}$	magnetic current density	V-m^2
$\hat{\mathbf{n}}$	unit normal vector	-
$\mathbf{r}$	observer point	M
$\mathbf{r}'$	source point	M
A	area	m^2

G	conductance	S
G_{R}	Green's function	1-m
M_{TX}	magnetic dipole moment of transmitter coil	$\mathrm{A{\cdot}m^2}$
N	number	-
S	surface	$\mathrm{m^2}$
U, V	voltage	V
Z_s	surface impedance	Ω
g_η	one dimensional basis function	
j	complex number	-
k	wave number	1-m
l	length, distance	M
t	thickness	M
Λ	RWG basis function defined over the triangle	-
Λ_η	eigenvalues	-
γ	propagation constant	-
ε	permittivity	F-m
ε_{o}	free space permittivity	F-m
ε_{r}	relative permittivity	-
$\tilde{\varepsilon}$	complex permittivity	F-m
η	wave impedance	Ω
η_{o}	free space wave impedance	Ω
λ	node spacing factor	-
μ	magnetic permeability	H-m
μ_{o}	free space magnetic permeability	H-m
μ_{r}	relative magnetic permeability	-
ρ_{e}	electric charge density	$\mathrm{C\text{-}m^3}$
ρ_{m}	magnetic charge density	$\mathrm{Wb\text{-}m^3}$
σ	conductivity	S-m
φ	electric scalar potential	V
ω	angular frequency	Hz
$\widehat{H}_n^{(1)}$	normalized Hankel function of the first kind	
$H_n^{(2)}$	regular Hankel function of the second kind	
$\breve{H}_n^{(2)}$	spherical Hankel function of the second kind	

J_n	regular Bessel function
$\hat{J}_n$	normalized Bessel function
$\check{J}_n$	spherical Bessel function
P_n	Legendre polynomial
P_n^1	associated Legendre polynomial
$\Re$	real component of complex number
$\Im$	imaginary component of complex number
x, y, z	Cartesian coordinate system
r, θ, ϕ	spherical coordinate system

SI derived unit	**definition**	**SI base units**
C	Coulomb	s·A
F	Farad	$s^4 \cdot A^2$-$m^2 \cdot kg$
H	Henry	$kg \cdot m^2$-$s^2 \cdot A^2$
Hz	Hertz	1-s
S	Siemens	$s^3 \cdot A^2$-$kg \cdot m^2$
V	Volt	$kg \cdot m^2$-$s^3 \cdot A$
Wb	Weber	$kg \cdot m^2$-$s^2 \cdot A$
Ω	Ohm	$kg \cdot m^2$-$s^3 \cdot A^2$

u and v show the coil orientation in the equation of U_{uv}

u	orientation of receiver coil
v	orientation of transmitter coils

Chapter 3: TESTING A PROTOTYPE TRI-AXIAL INDUCTION LOGGING TOOL IN-AIR AND IN A NEAR SURFACE TRENCH

This chapter[2] introduces a new prototype tool which is tested with scaled down fracture models. First, a review is provided on the physics of coil design, the essentials of the measurement set-up, and the theory of electromagnetic scaling. Then, the detailed specification of a developed field-sized prototype induction tool is shown and the design of two main experimental setups is presented. The tool works at the same operational frequency as in the field, and the tool sizes are selected based on the actual wellbore dimensions.

The study comprises experiments in two different environments: (i) a laboratory environment where in-air measurements are performed, (ii) a field environment where measurements are performed near (below) the earth's surface. The first experimental setup enables easy calibration of the tool, as well as the insertion and removal of targets, thus, facilitating the gathering of data for a range of targets with various parameters. Fracture models of various sizes, shapes, and dip-angles are tested. This set-up was built in the laboratory of E-Spectrum Inc. in San-Antonio, TX. The second setup enables measurement in a horizontal well close to the surface, in a lossy and more realistic earth background. This experiment was carried out in a test site in a ranch in Blanco County, TX. The measurements in both cases are compared to a numerical simulator introduced in the previous chapter. The results and set of conclusions are provided while discussing the potential capabilities of the current tool.

[2] The experimental results shown in this chapter were first presented in Shiriyev et al. (2018). Shiriyev used the simulation results to obtain specifications for the induction coils, built an experimental setup to test the tool in a laboratory setting, demonstrated that the experiments and the model agree very well with each other, established the detectability and differentiability of signal levels with realistically sized tri-axial coils that can be deployed in a downhole tool and demonstrated the feasibility of the EM measurements for fracture diagnostics in a shallow earth experiment.

3.1. LITERATURE REVIEW

In this section, three main questions are answered: 1) how to design the most efficient low frequency transmitter and receiver coils which will work in a typical oil well, 2) how to test them in a controllable environment, and 3) how to represent large field scale fractures in a relatively small lab environment.

3.1.1. Induction Coil Design

The magnetic dipole moment (or torque) is the main characteristic of a transmitter coil and determines the strength of induced magnetic fields. It is defined as:

$$M = \mu_{\mathrm{r,core}} NAI \tag{3.1}$$

given that the cross-sectional area of windings is small compared with the coil diameter, inductance is ignored and the operation frequency is low (Frischknecht, 1988). The emphasis is usually placed on achieving large moments to obtain detectable signals on a receiving component. This can be accomplished by increasing any component in the right-hand side of the equation above, and in the following three paragraphs, we discuss each one of them.

A typical transmitter coil does not have much flexibility in the cross-sectional area selection. It will be elongated along the wellbore direction (z-axis) to provide high magnetic dipole moments in restricted wellbore sizes (~4 inches). The elongations of x- or y-oriented transmitter coils allow an increase in the cross-sectional area of the coil. For the z-oriented coil, the elongation allows us to increase the number of turns.

The amount of current that can be driven through a wire at any frequency is limited by thermal considerations. To assure the endurance of a coil in a given environment, the minimization of power loss is essential. This is defined as:

$$P_{\text{coil}} = \frac{1}{2} R_{\text{coil}} |I_{\text{coil}}|^2 \tag{3.2}$$

The minimization of power loss also limits increasing the number of turns by decreasing the cross-sectional area of the wire; the overall resistivity will increase limiting the maximum current. It can be avoided by sharing the current among parallel connected wires:

$$I_{\text{coil}} = I_{\text{coil},1} + \cdots + I_{\text{coil},n} \tag{3.3}$$

where n represents the number of wires connected in parallel. Assuming that all coils are identical to each other, the total resistivity will be decreased in an amount equal to the number of parallel connections:

$$R_{\text{coil}} = \frac{R_{\text{wire},i}}{n} \quad \text{where} \quad R_{\text{wire},i} = \frac{\rho_{\text{wire},i} l_{\text{wire},i}}{A_{\text{wire},i}} \tag{3.4}$$

When the relative magnetic permeability of a core is equal to one, the coil is referred as an air-core coil. It describes an inductor that uses plastic, ceramic or other nonmagnetic forms as a core, as well as those that have only air inside the winding. These types of coils are often used at high frequencies because they are free from energy (or core) losses that occur in ferromagnetic cores due to hysteresis and eddy currents in the core material. The losses increase with an increase in the frequency. To increase the dipole moment of transmitter coils at low frequency we use, a core with a relative magnetic permeability more than one can be used. In general, long and slender shapes of coils allow the effective use of a magnetic core material (Frischknecht, 1988).

The transmitter coil suggested by Heagy and Oldenburg (2013) is a magnetically permeable core wrapped with several hundred turns of wire and has a magnetic dipole moment of 5,000 $\text{A} \cdot \text{m}^2$ in the frequency range of 1-100 Hz, and only several hundred $\text{A} \cdot$

m^2 at frequencies above 500 Hz. Lastly, the best practice for the use of transmitter coils in wells requires the monitoring of input currents to take into account any possible changes in coil parameters. Factors that are likely to cause changes are temperature or humidity that may cause an expansion or contraction of coil windings and proximity to a conductive material that may cause electrical loading.

Design criteria to be used for transmitter coils can be applied to receiver coils in the same way. The main factors to consider in the design of receiving loops are the size, sensitivity and stability of loop characteristics, insensitivity to extraneous electric fields and disturbance of normal fields due to the loop itself. Correct measurements are not obtained if the probe significantly disturbs the fields in the vicinity of the model media; that is if the probe behaves as a secondary source. Receiver coils suggested in Heagy and Oldenburg (2013) are the magnetically permeable core wrapped with several thousand turns of wire. Magnetic fields in the order of 10^{-8} A/m can be detected with these coils. These receiver coils are directly connected to the recording apparatus which also contains an amplifier board to increase the power of a received signal. At low frequencies, this direct connection is not expected to introduce major errors (Frischknecht, 1988).

3.1.2. Experimental Set-up

In modeling moving source methods with targets placed in air, the coils can be fixed and the target may be placed on a moving carriage which moves by the coils. To avoid extraneous EM responses, large metallic parts or other conductive materials should not be used in the construction of mechanical parts that are within or near the working region. It is a good practice to construct carriages, tracks and other structures mostly of wood, plastic, concrete and other insulating materials. Measuring instruments should be placed far enough from the region so that their metal cases and chassis do not produce a

response. In our experiment, we conduct frequency domain measurements. Therefore, several of the required functions used in the measurement circuit can be combined in one unit known as a lock-in-amplifier. The frequency range of most lock-in-amplifiers is below 100-200 kHz which suits for our application well (Frischknecht, 1988).

3.1.3. Electromagnetic Scaling

Both the laboratory and field experimental environments have space limitations for the electromagnetic targets. They must be of a significantly reduced size compared to the ones likely to be detected in an actual oil and gas formation while the tool parameters, such as coil size and operation frequency, are kept similar to those expected in the field. Following the theory of EM scaling (Sinclair, 1948), it can be shown that similar signal magnitudes can be obtained only if the induction number defined as:

$$N^{\mathrm{i}} = \sigma\mu\omega l^2 \tag{3.5}$$

is kept invariant for all electric conductivities σ, magnetic permeabilities μ and spatial dimensions l in the system operated at an angular frequency of ω. For some components, however, this requirement can be relaxed. For example, the dimensions of coils do not need to be scaled if their radii are smaller than one-tenth of the distance between them (and neglecting the mutual interactions between the coils). This condition is satisfied for the coils in this work; l_1 and l_2 in Fig. 1.1 are kept more than ten times larger than the radius of coils. The conductivity of the background, if sufficiently lower than that of the propped fracture, has little effect on the resulting secondary fields. As for the propped fracture's conductivity, if the skin depth given as:

$$\delta = \sqrt{\frac{2}{\sigma\omega\mu}} \tag{3.6}$$

is sufficiently larger than the thicknesses of both the original and scaled propped fractures, it is sufficient to only scale the propped fracture's conductance, rather than its conductivity or thickness separately, to maintain similar signal levels (Frischknecht, 1988, Eq. 3.5 becomes $N^{\mathrm{i}} = G\mu\omega l$). At the operation frequency of 1 kHz and effective proppant conductivity of 333 S/m (Zhang et al., 2016), the skin depth is 872 mm – several times larger than the expected propped fracture thickness of 5 mm (Sharma and Manchanda, 2015). In this study, the propped fracture models are made of industrial aluminum foil with a mean conductivity of 34.6 MS/m at 20 ˚C temperature and a mean thickness of 25.4 μm. The skin depth of aluminum at an operating frequency of 1 kHz is 2.7 mm – much larger than the foil's thickness.

3.2. BUILDING A PROTOTYPE TOOL

In the design of the prototype tool, the goal is to keep the main characteristics the same as in the field deployable tool. Firstly, the operation frequency is selected to be 1 kHz, low enough to detect fractures a few tens of meters away from the wellbore. Secondly, transmitter and receiver coils are designed based on the physical constraints of wellbores. Lastly, the prototype tool can be carried and tested in different environments, especially in conductive backgrounds.

3.2.1. Transmitter and Receiver Coils

This sub-section describes the induction tool and the measurement equipment that were used in the experiments. Solenoidal coils are used for transmitting and receiving (Fig. 3.1). The coils are designed to operate at the frequency of 1 kHz without overheating. The transmitter coils are made using a 16 AWG (American wire gauge) magnet wire and carry a nominal current of 2.3 A (x, y-oriented coil) and 4 A (z-oriented

coil) which was sufficient to provide detectable differential signals. To enable the tool's passage in a narrow well, the coils are designed to be long in the wellbore direction: the *z*-oriented coil has a circular profile and a larger number of turns while the (*x*, *y*)-oriented coil is rectangular with a high aspect ratio. The *z*-oriented coil uses a magnetic core to provide an increased magnetic dipole moment. Table 3.1 summarizes the remaining properties of the transmitter coils. Note that, while the *x*- and *y*- oriented coils are single wires, *z*-oriented coil's current is distributed among three wires wound in parallel.

Orientation	***x*** and ***y***	***z***
Number of parallel connection	1	3
Total number of turns	90	114
Cross-sectional area [cm^2]	256	40
Height [cm]	40.4	32
Relative core permeability	air core	14

Table 3.1: Summary of the transmitter (Tx) coil properties.

As for the receiver coils, these are identical regardless of their orientation, made with an air core and 600 turns of a 32 AWG magnet wire. Their cross-sectional area and height are 30 cm^2 and 1.3 cm, respectively.

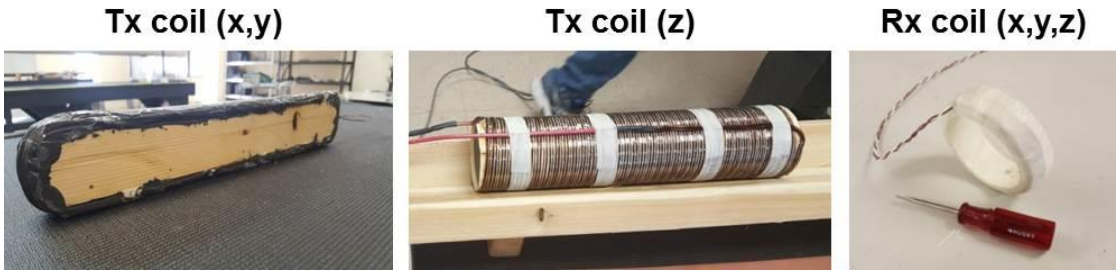

Figure 3.1: Tri-axial transmitter (Tx) and receiver (Rx) coils.

3.2.2. Measurement System

The circuit system used for the experiments is described schematically in Fig. 3.2. The Pre-Amp PCB (printed circuit board) connected to receiver coils (Rx_1 and Rx_2) includes the bucking and amplification of received signals. A bucking coefficient of $l_1^3/l_2^3 = 1/2$ is hardwired. The lengths l_1 and l_2 are fine-tuned during the tool's calibration to minimize the received signal when operated in air with no target. The bucked signals are amplified by a factor of 100. The set-up allows having a single receiver measurement without any amplification factor.

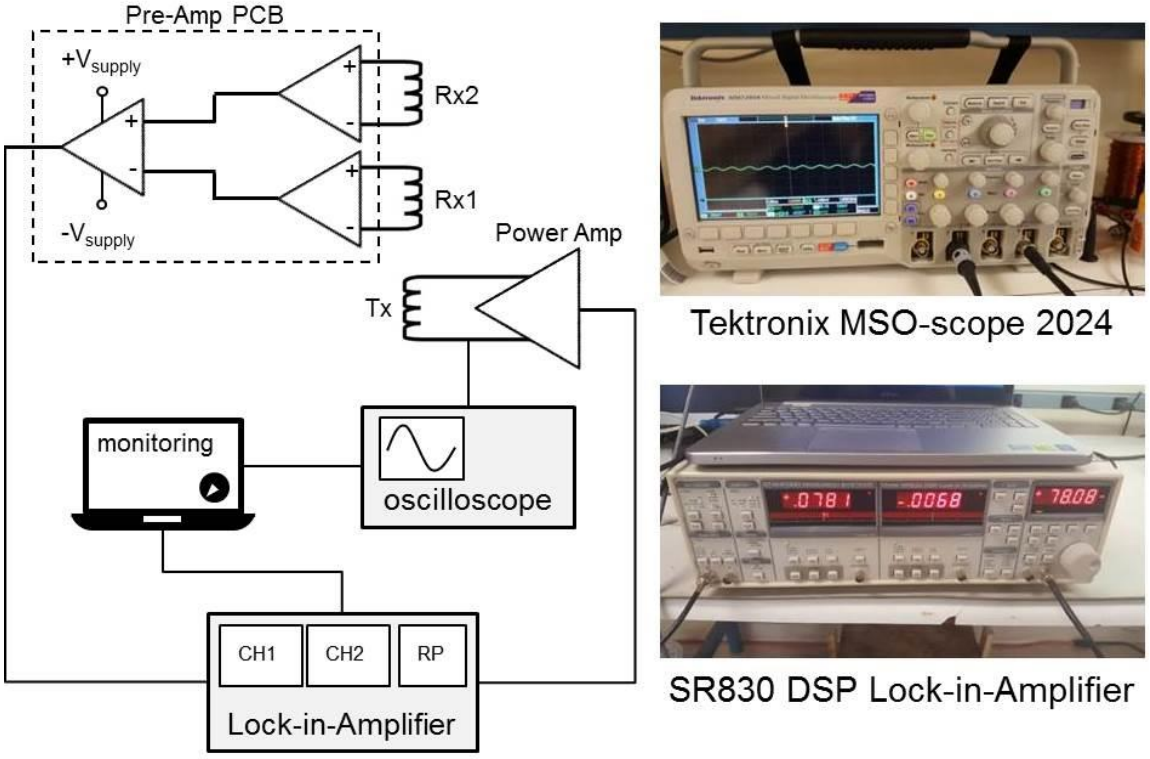

Figure 3.2: Block diagram of the prototype tool: transmitter (Tx) and receiver (Rx1 and Rx2) coils; pre-amp circuit board shown with dashed rectangle; monitoring laptop with full control over the circuit; oscilloscope for measuring the transmitter coil input current; and lock-in-amplifier for signal referencing and decomposition.

The lock-in-amplifier receives amplified bucked signals, with the voltage on the transmitter coil being its reference signal (Fig. 3.2). It outputs, in two separate channels, the bucked signal's in-phase and quadrature components with respect to the reference signal. If we assume the input current of the transmitter coil to be real ($\mathfrak{R}$) then the following rotation matrix multiplication can be used:

$$\begin{bmatrix} \mathfrak{R} \\ \mathfrak{J} \end{bmatrix} = \begin{bmatrix} -\sin\theta & -\cos\theta \\ \cos\theta & -\sin\theta \end{bmatrix} \begin{bmatrix} X \\ Y \end{bmatrix} \tag{3.7}$$

where θ is the reference phase. The transmitter coil input current is measured with an oscilloscope. At selected time instances the monitoring unit continuously displays and records: the time, reference signal, reference frequency, phase with respect to the reference signal and the two output channels (X and Y).

3.2.3. Coil Positioning

Data were collected to see how close the receiver coils can get to the transmitter coil. Fig. 3.3 shows the results both for the receiving and bucking coils in a co-axial coil configuration and data were gathered by measuring the voltage on a single receiver coil for two minutes (30 data at least) as a function of distance from the transmitter. Both receiver coils exist in the setup during the recordings; however, one is disconnected from the circuit board (Fig. 3.2) when the measurements are made for the other coil. The results showed half a meter to be a minimum distance to get the noise sufficiently low.

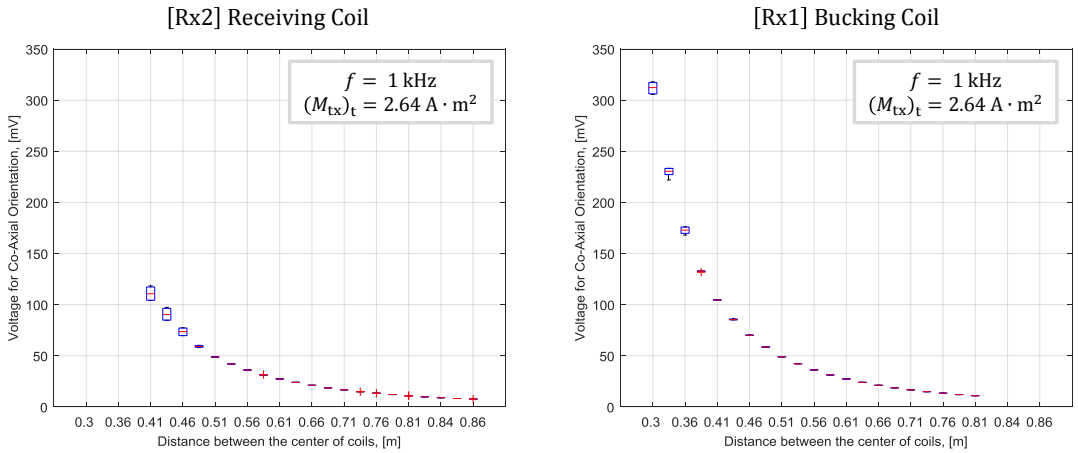

Figure 3.3: Box charts for measured incident signals at different transmitter-receiver coil spacing; left and right plots show results for receiving and bucking coils, respectively. Transmitting magnetic dipole moment is calculated using coil properties and measured input current.

3.2.4. Verification of Coil Parameters

The effective magnetic induction properties of the transmitter and receiver coils both for co-axial and co-planar coil configurations are estimated to be used as an input into the numerical simulation results. By measuring the voltage on a single receiver coil as a function of distance from the transmitter, for a given (measured) transmitter current, and fitting it to the theoretically expected curve, the multiplication of the receiver area and turn number by the transmitter's magnetic dipole moment ($A_{\mathrm{RX}}N_{\mathrm{RX}}M_{\mathrm{TX}}$) is calculated. In this setup, only one receiver coil exists at a time.

The theoretical curve is calculated from the field equation (Balanis, 2005) of a small circular loop. For a given source and sink points, voltages of co-axial configuration can be calculated with the following equation for free space:

$$U_{zz}(z,z') = -j\omega\mu_o A_{\mathrm{RX}} N_{\mathrm{RX}} H_z(z,z') \tag{3.8}$$

where

$$H_z(z,z') = M_{\mathrm{TX}} \frac{jk}{2\pi(z-z')^2}\left[1+\frac{1}{jk(z-z')}\right]e^{-jk(z-z')} \tag{3.9}$$

z is an arbitrary point where the field is calculated (the center of a receiver coil) and z' (the center of a transmitter coil which is assumed to be the origin of the coordinate system) is the location of a point source oriented in the z-direction. For the co-planar coil configuration, voltages will be calculated for free space with:

$$U_{yy}(z,z') = -j\omega\mu_o A_{\mathrm{RX}} N_{\mathrm{RX}} H_y(z,z') \tag{3.10}$$

where

$$H_y(z,z') = -M_{\mathrm{TX}} \frac{k^2}{4\pi(z-z')}\left[1+\frac{1}{jk(z-z')}-\frac{1}{k^2(z-z')^2}\right]e^{-jk(z-z')} \tag{3.11}$$

Here, sampling is again along the z-direction and coils are oriented in the y-direction. The value of $A_{\mathrm{RX}}N_{\mathrm{RX}}M_{\mathrm{TX}}$ minimizing the error between measured and calculated data is selected as an input into the numerical model:

$$\sum_i \left[w_i\left(U_i - U_i^{\exp}\right)\right]^2 = 0 \tag{3.12}$$

where w is the weight factor and is larger for the middle part of the data because both short spacing data and long spacing data are not as reliable as the data at middle distances. For the short spacing, more deviation is expected because of noise (see the previous sub-section). For the long spacing receiver, the sensitivity of measurements may decrease because of the low signal levels.

In the measurements, signals are sampled at a rate of one sample per second, over a period of 30 seconds and averaged (shown as dots in Fig. 3.4). The magnetic dipole moments were extracted from the theoretical curves (solid line) such that the coefficient $A_{\mathrm{RX}}N_{\mathrm{RX}}M_{\mathrm{TX}}$ is ~21.7 Am^4 and ~13.5 Am^4 for the co-axial and co-planar configurations, respectively. These calculated values match the coil specifications very well.

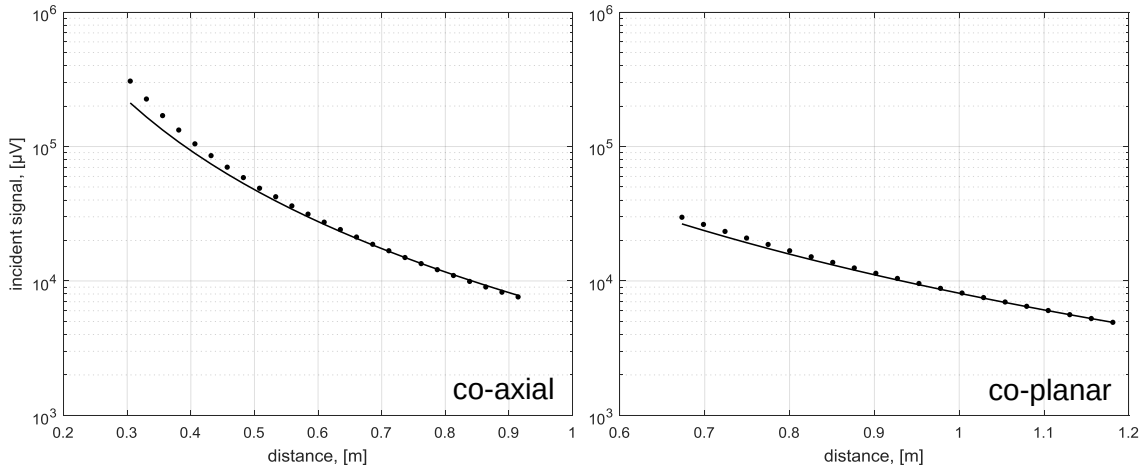

Figure 3.4: Estimation of transmitting and receiving moments: dots show measurements for co-axial (left) and co-planar (right) coil configurations; and solid line is the analytical solution with the best calculated moment coefficient.

3.2.5. Primary Bucked Signal

In this section, results are shown for the measurements before the fractures are in place. At each configuration, two receiver coils are placed inside the tool's inner shell (PVC pipe with a nominal size of 3 in. (~8 cm)) in a bucking configuration, at nominal distances l_1 and l_2 from the transmitter coils. The distance l_2 is tuned to minimize the magnitude at the lock-in amplifier's output. This tuning process is repeated for every test and if there is no other limitation l_1 and l_2 are not changed significantly. Once a minimum is obtained, the coils are fixed in place and the inner shell is inserted into an outer shell PVC pipe with a nominal size of 4 in. (~10 cm). No adjustments are made for centralizing the inner shell inside the outer shell. The test is conducted in a closed lab with a floor area of ~100 m^2 and a height of ~4 m during the daytime. Surrounding materials are all made of wood and plastic; metallic targets are at least 3 meters away both from the transmitter and receiver coils.

The transmitter coil input current (Fig. 3.5) and primary bucked signal (Fig. 3.6) are monitored over 10 minutes. Signals are sampled at a rate of one sample for every 5 seconds. No significant drift was observed during this period and the variation in the primary bucked signal which is normalized with respect to transmitter coil input current was not more than 1 μV in the co-axial and co-planar configurations and not more than 0.2 μV in the cross-polarized configuration.

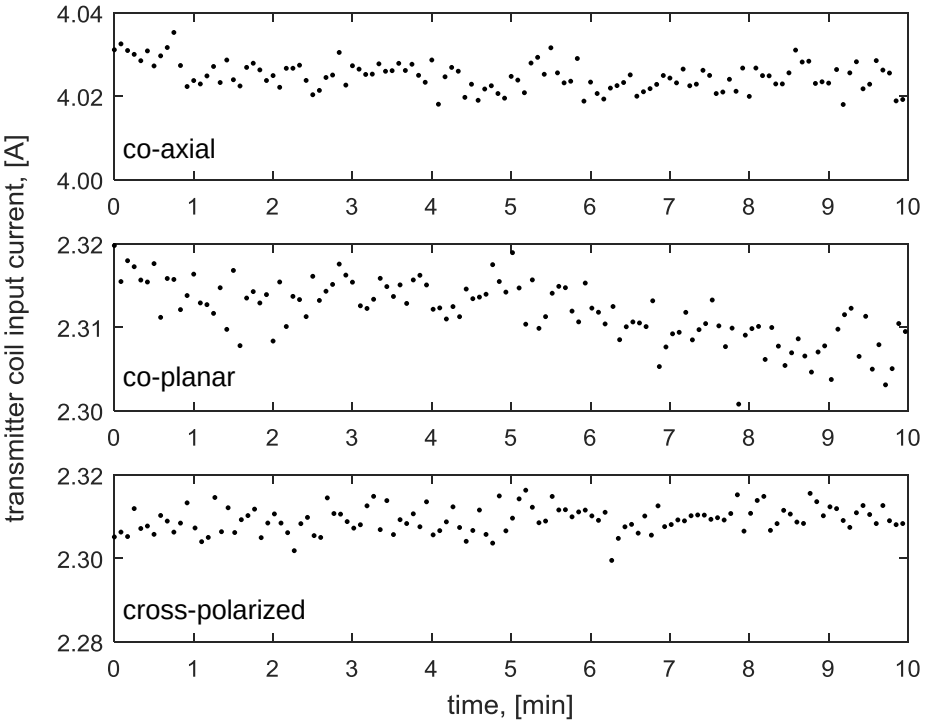

Figure 3.5: The variation in the measured transmitter input current over time; presented for the co-axial (upper), co-planar (middle) and cross-polarized (lower) coil configurations before the measurements with fracture models.

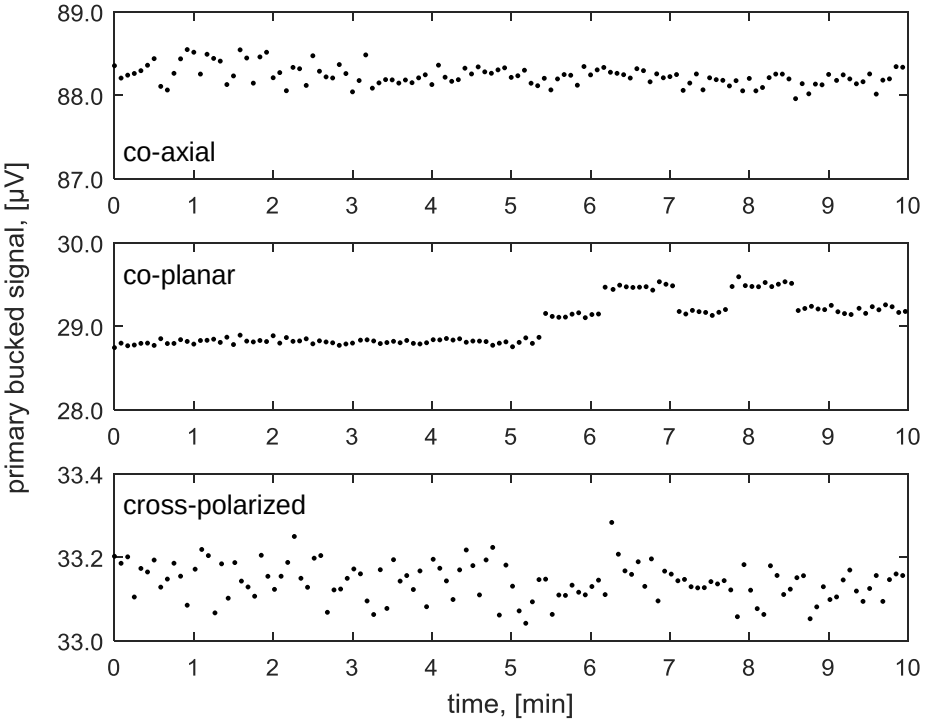

Figure 3.6: The variation in the measured primary bucked signal over time; presented for the co-axial (upper), co-planar (middle) and cross-polarized (lower) coil configurations before the measurements with fracture models; the data are normalized with respect to transmitter coil input current.

3.3. PROTOTYPE TOOL TESTING

In this section, the design of small scale and highly conductive targets, intended to produce a response close in magnitude to that of realistic field propped fractures, is explained. The set-ups used in the lab-air and shallow near-surface experiments are discussed.

3.3.1. In-Air Experiment

The laboratory in-air experiments include primary and total bucked signal measurement for various targets. To emulate various hydraulic fracture geometries in the

lab, three sets of propped fracture models are used for the in-air experiments, Fig. 3.7: (a) circular fractures of three different radii, (b) elliptical fracture of three different aspect ratios, and (c) circular fractures with five different dip-angles.

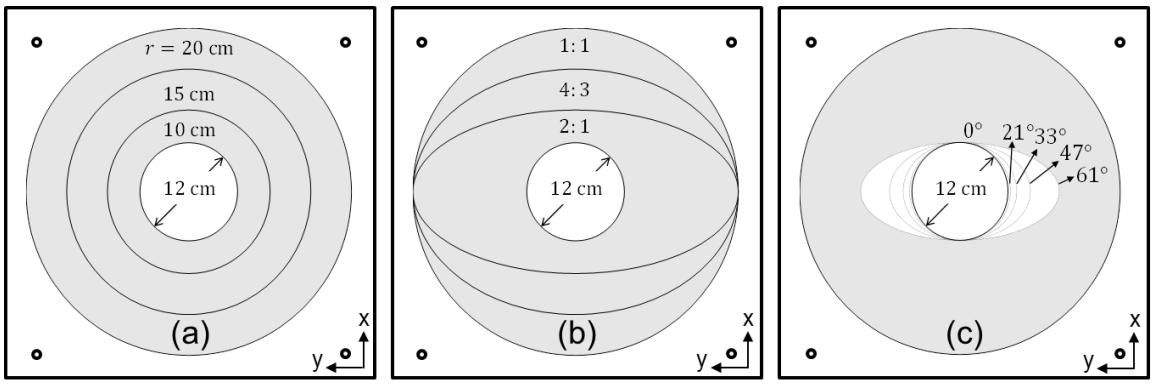

Figure 3.7: Fracture models used for laboratory experiments: (a) orthogonal fractures of various areas; (b) orthogonal fractures with various aspect ratios, the major radius is 20 cm; and (c) fractures of various dips rotated about the *x*-axis.

Measurements are acquired on a test bench at a height of roughly 1 m above the ground. The outer shell of the tool is held, by non-conductive (plastic) boxes, above the test bench (Fig. 3.8 and 3.9). Model targets are sandwiched between acrylic sheets that enable fixing them in a prescribed orientation and centralized with respect to the outer shell. After the tuning, the distances between the center of receivers and the center of the transmitter coil are $l_1 = 0.96$ m and $l_2 = 1.21$ m for all coil configurations. Throughout the measurement, the tool is kept stationary and the signal is first measured without model fractures. A typical response for different configurations of coils is shown in Section 3.2.5. Then, the fracture model is moved within a range of [-0.4, 0.4] m with respect to the midpoint between the receiver coils, in 2.5 cm intervals. At each model target position, signals are sampled at a rate of one sample per second, over a period of

30 seconds and the mean signal value measured without the fracture is subtracted to obtain the differential signal.

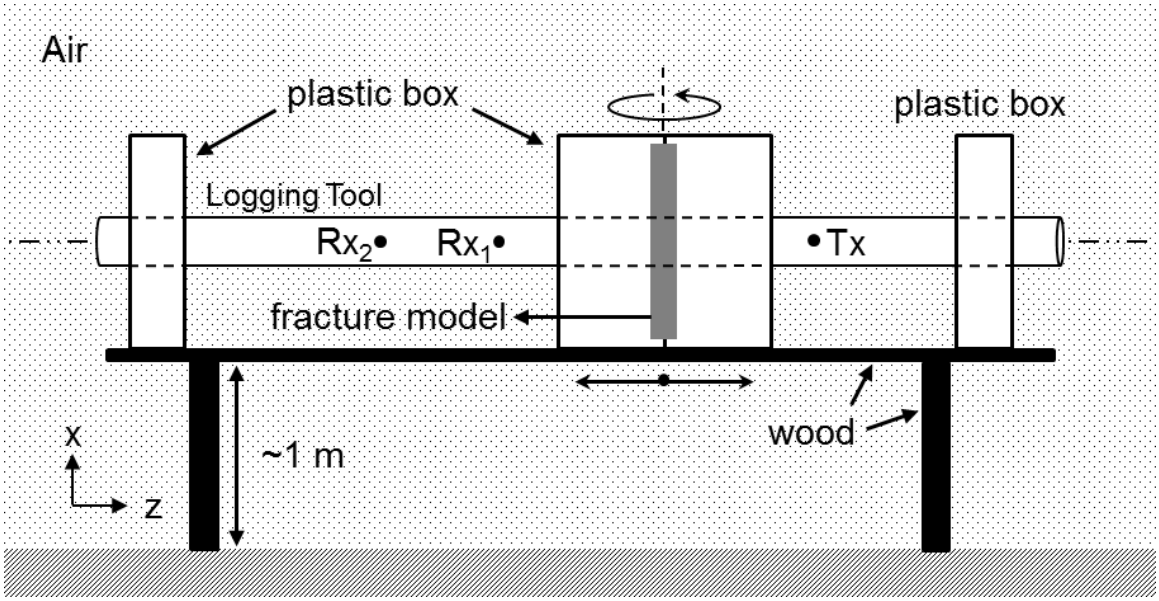

Figure 3.8: Laboratory experimental setup: an outer shell backbone (horizontal pipe) containing coils, fracture model inside a holder (middle box), and two outer shell backbone holders (left and right boxes).

Figure 3.9: Laboratory experimental setup: top picture shows main set-up which allows moving fracture models across the center of receivers; during the tests, the surrounding of the tool was kept free of metal; bottom-left picture shows the plastic box which keeps fracture model in a given orientation; and bottom-right picture shows centralization of the fracture model with respect to the outer shell of the tool.

3.3.2. Near Surface Experiment

To evaluate the performance of the tool in a more realistic medium, experiments were conducted in a shallow subsurface site as well. The field experiment includes a tuning stage similar to that in the laboratory experiment and uses the magnetic inductance properties measured in those tests. After the tuning, the distances between the center of receivers and the center of the transmitter coil are $l_1 = 0.96$ m and $l_2 = 1.21$ m. Following the tuning, the tool is used underground, but near the surface, to detect a

buried target. A single elliptical fracture model was placed at a certain dip-angle. This simulated fracture model was designed specifically for the near-surface field experiment, Fig. 3.10.

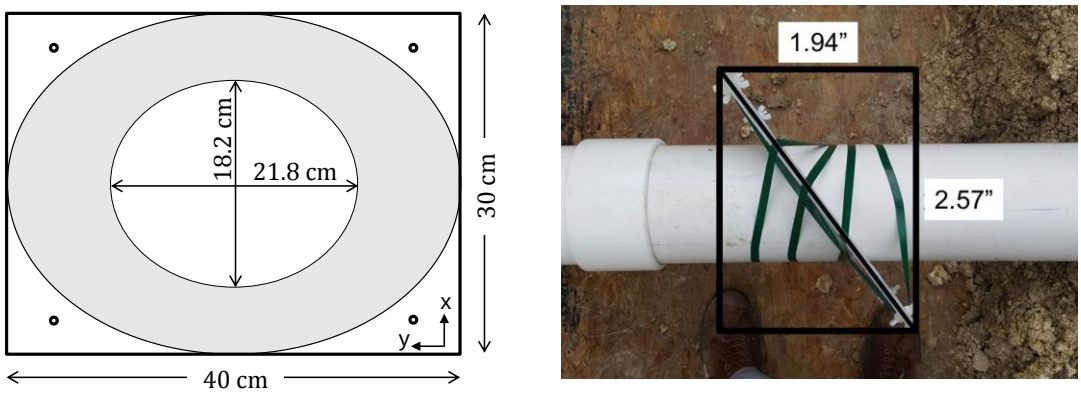

Figure 3.10: Fracture model used for near surface experiment: left figure is the elliptical fracture model which is designed to be 37˚ rotated about the *x*-axis; right figure is field taken picture to verify the dip-angle.

For this experiment, a 6 inch PVC pipe of 12 m length (serving as a well) was buried horizontally at a depth of 1 m below the surface (Fig. 3.11). An aluminum foil target (Fig. 3.10), sandwiched between acrylic sheets, was placed around and centralized with respect to the buried pipe at a dip-angle of 37˚ about the vertical axis (*x*-axis). While designed to be placed at the prescribed dip-angle, the positioning was also geometrically verified using an image taken at the test site. Here, the target is stationary and the tool (outer shell) is moved inside the buried pipe. The tool is lowered into a trench through an opening at the end of the buried pipe and is pushed such that the midpoint between receivers moves in the range [-0.5, 0.5] m with respect to the fracture’s center. No adjustments are made for centralizing the outer shell inside the buried pipe. Data is recorded at intervals of 5 cm and sampled in the same manner as in the laboratory experiment. Then, the primary signal (a measurement far away from the fracture model)

is subtracted to obtain differential signals. The background formation conductivity is independently measured with an earth/ground tester (Fluke, 2006).

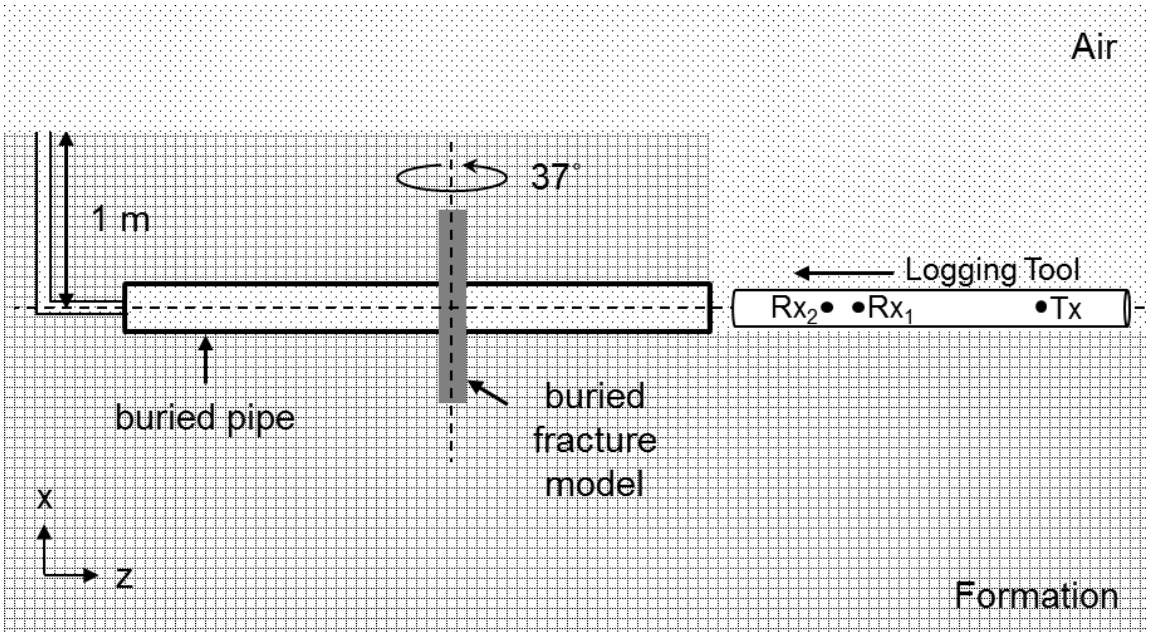

Figure 3.11: Near-surface field-experiment setup illustration: 6" PVC pipe buried together with the fracture model (Fig. 3.10); the tool is pushed and pulled inside the well with the plastic string attached from the transmitter coil end; and all cable connections are attached from the same end.

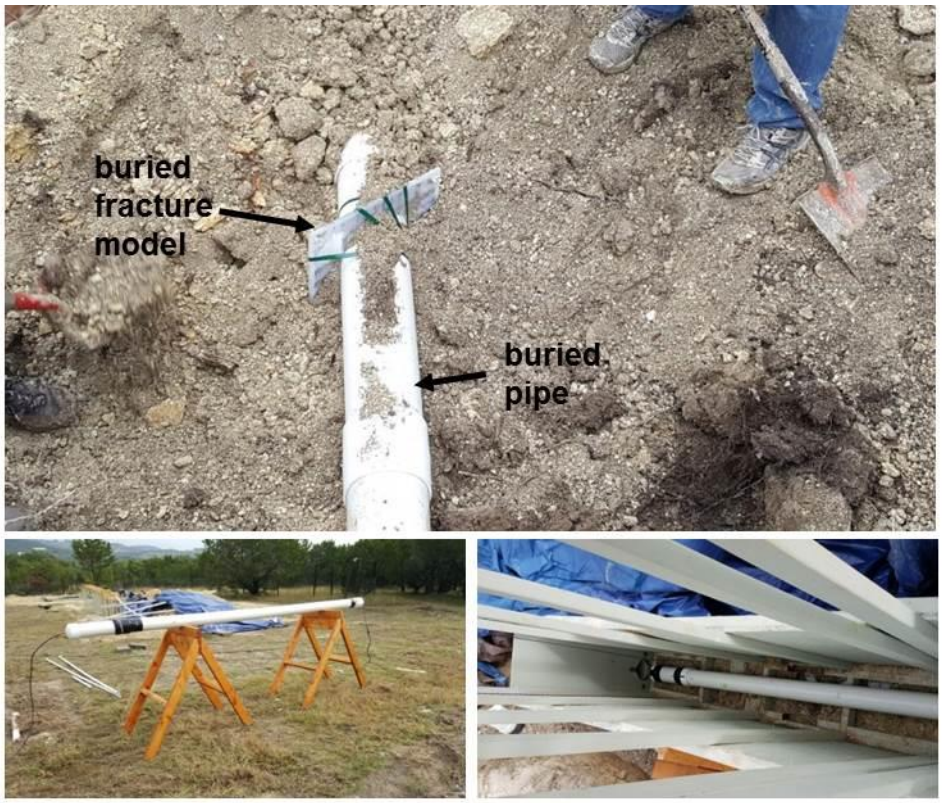

Figure 3.12: Near-surface field-experiment setup illustration: Top picture shows the 6" PVC pipe and fracture model before the hole is covered with soil; bottom-left picture shows the prototype tool on the surface before logging the well; and bottom-right picture shows the prototype tool just before it was pushed into the well.

3.4. RESULTS AND DISCUSSION

In the previous sections, details of a prototype tool, experiment set-ups, fracture model targets and measurements performed were discussed. In this section, the results of these experiments are summarized for different coil configurations, fracture parameters, and surrounding properties in magnitude and phase plots.

3.4.1. Investigation of Different Model Parameters

The differential signals obtained for the various coil configurations are summarized in Table 3.2 which lists typical signal levels observed around a fracture model for each coil configuration (table columns) and for the different parameter of fractures sets in Fig. 3.7 (table rows). It should be noted that, while the results are time averaged at each tool position, deviations from the average of up to 10 μV for strong signals (>100 μV) and 1 μV for weak signals (>10 μV) were observed and that signals weaker than 0.1 μV were not detectable.

Parameter	Co-axial	Co-planar	Cross-polarized
Surface Area	>100 μV	>10 μV	<1 μV
Aspect Ratio	>100 μV	>10 μV	<1 μV
Dip Angle	>100 μV	>100 μV	>100 μV

Table 3.2: Summary of maximum differential signal levels obtained for different fracture parameters and coil configurations.

In the following subsections, the signal magnitudes are plotted as a function of the distance between the location of the fracture model and the midpoint of receivers for the five cases corresponding to the: {co-axial, surface area}, {co-axial, aspect ratio}, {co-planar, aspect ratio}, {co-axial, dip-angle}, and {cross-polarized, dip-angle}. For each of the cases, the plots show both simulated (solid line) and the measured (circles) results. Excellent agreement between the signal magnitudes are observed for all the cases tested. The maximum error observed was less than 10% with most cases showing less than 1% error.

3.4.1.1. Circular Fracture Models

Beginning with the co-axial coil configuration, for which the measured signal levels are the largest (Table 3.2), Fig. 3.13 presents the signals measured for the model targets in Fig. 3.7(a). This configuration's sensitivity to the target's area is evident from the increase in the signal magnitude with the fracture area; however, fractures of greater aspect ratio can potentially produce similar signal levels in this coil configuration.

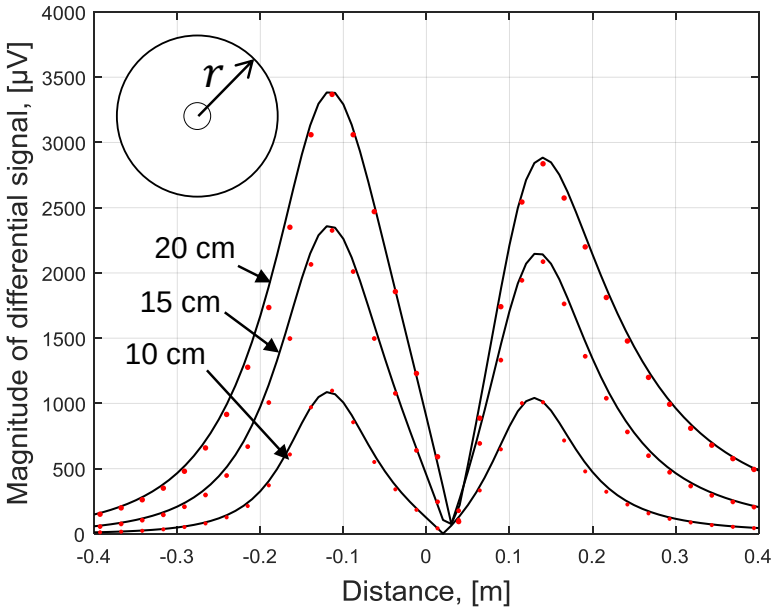

Figure 3.13: In-air test results for the co-axial (*zz*) coil configuration and for the fracture model targets in Fig. 3.7(a). Solid lines mark the simulated results, and red dots mark the measured signals.

3.4.1.2. Elliptical Fracture Models

Only the co-planar configuration measurements were shown to be sensitive to the symmetry of a fracture, Yang et al. (2015). Hence, additional information from this configuration can be used for the determination of the fracture aspect ratio. First, in Fig. 3.14, co-axial signals are shown for the targets of Fig. 3.7(b). As can be seen from the

plot, the magnitude of signals is strong; however, symmetric fractures of an equivalent size can potentially produce similar signal levels in this coil configuration. In Fig. 3.15, co-planar signals are shown for the same target where the signals are much weaker than those in the co-axial configuration. It is evident that these signals are sensitive to the aspect ratio of the fractures.

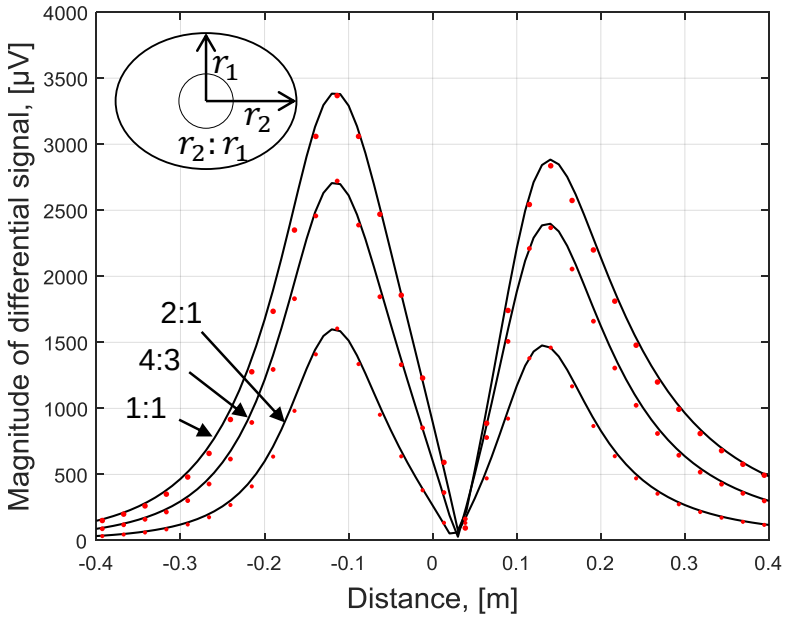

Figure 3.14: In-air test results for the co-axial (*zz*) coil configuration and for the fracture model targets in Fig. 3.7(b). Solid lines mark the simulated results, and red dots mark the measured signals.

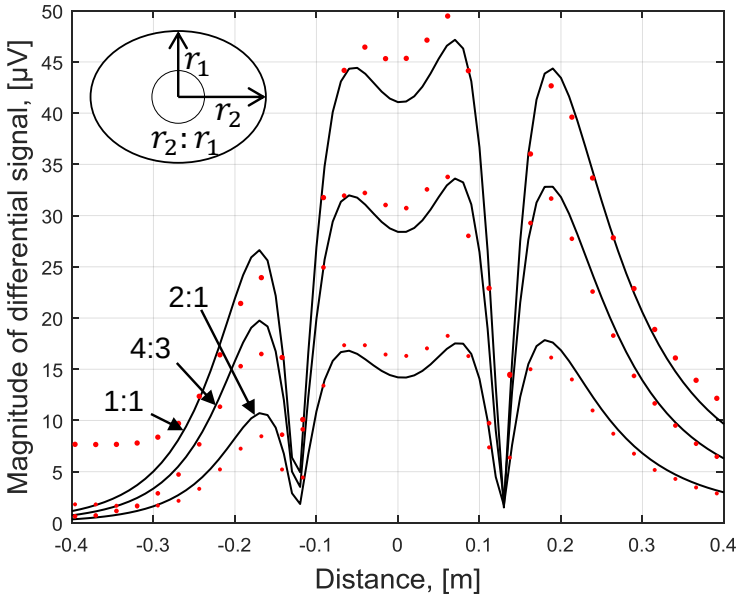

Figure 3.15: In-air test results for the co-planar (*yy*) coil configuration and for the fracture model targets in Fig. 3.7(b). Solid lines mark the simulated results, and red dots mark the measured signals.

3.4.1.3. Rotated Fracture Models

The response to the fracture's dip-angle (models are shown in Fig. 3.7-c) is demonstrated for both co-axial (Fig. 3.16) and cross-polarized configurations (Fig. 3.17). As the dip-angle increases, the received signals get weaker for the co-axial configuration and stronger for the cross-polarized configuration. It should be noted that all three configurations show strong sensitivity to the dip-angle (Table 3.2).

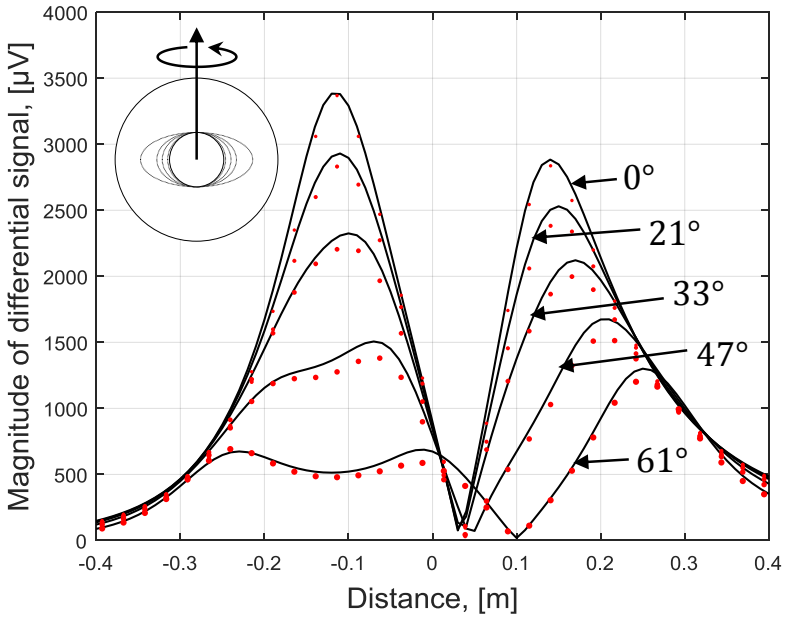

Figure 3.16: In-air test results for the co-axial (*zz*) coil configuration and for the fracture model targets in Fig. 3.7(c). Solid lines mark the simulated results, and red dots mark the measured signals.

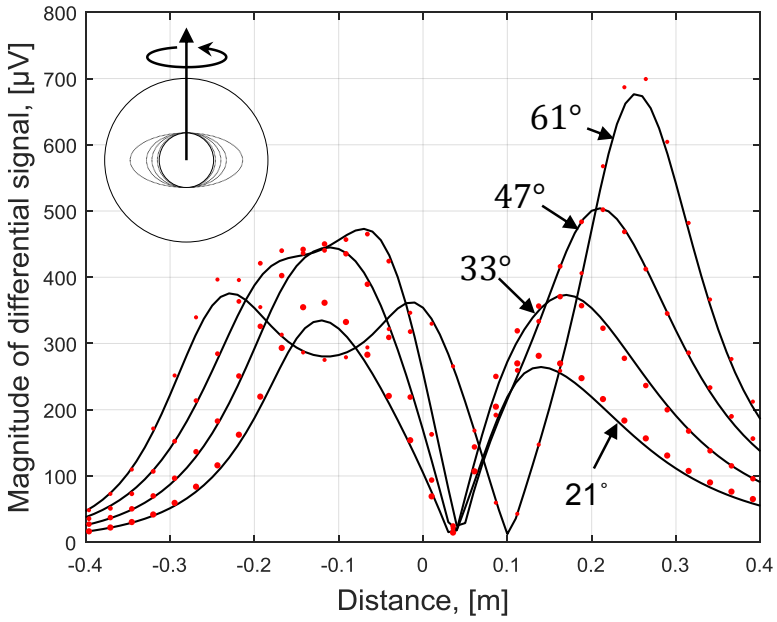

Figure 3.17: In-air test results for the cross-polarized (*zy*) coil configuration and for the fracture model targets in Fig. 3.7(c). Solid lines mark the simulated results, and red dots mark the measured signals.

3.4.2. Near Surface Field Experiment: Effect of Conductive Background

The signal magnitudes measured in the near-surface field experiment are presented next. During the measurements, soil conductivity in the range of 15-20 mS/m was measured (computed signals showed little dependence to the background conductivity). Only the co-axial configuration was used to produce the magnitude plot in Fig. 3.18. Once again, good agreement can be observed (<10 % of relative error) between the numerical and experimental results.

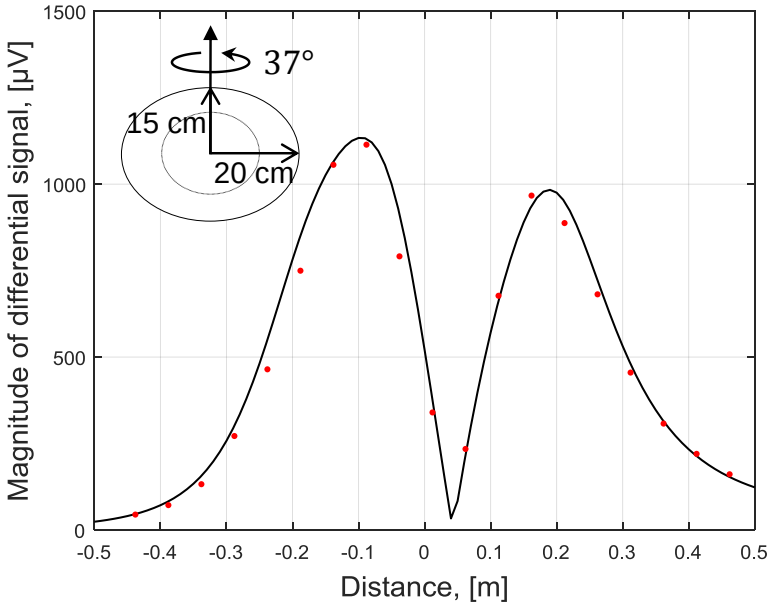

Figure 3.18: Near-surface buried target test results for the co-axial (*zz*) coil configuration and for the fracture model target in Fig. 3.10. Solid lines mark the simulated results, and red dots mark the measured signals.

3.4.3. Phase Plots

Finally, Fig. 3.19 presents the signals for all in-air lab and near-surface field tests (simulation – black dots, measurement – red dots) as polar plots. Examination of each of the sub-figures indicates that, while good agreement between the simulation and measurements was obtained for the magnitude, there is a phase mismatch between simulated and measured signals. The mismatch remains roughly constant across all measurements of a given coil configuration, and it can be attributed to the referencing; the simulated signals are referenced to the transmitter coil current while the measured signals are referenced to its voltage. Ideally, this should result in a phase difference of 90˚; however, the plots suggest that this mismatch ranges between 92˚ and 102˚, depending on the coils. This might not be an issue; as Fig. 3.19 shows that, for all studied

cases, the in-phase (real) components with coil current dominate the quadrature (imaginary) components.

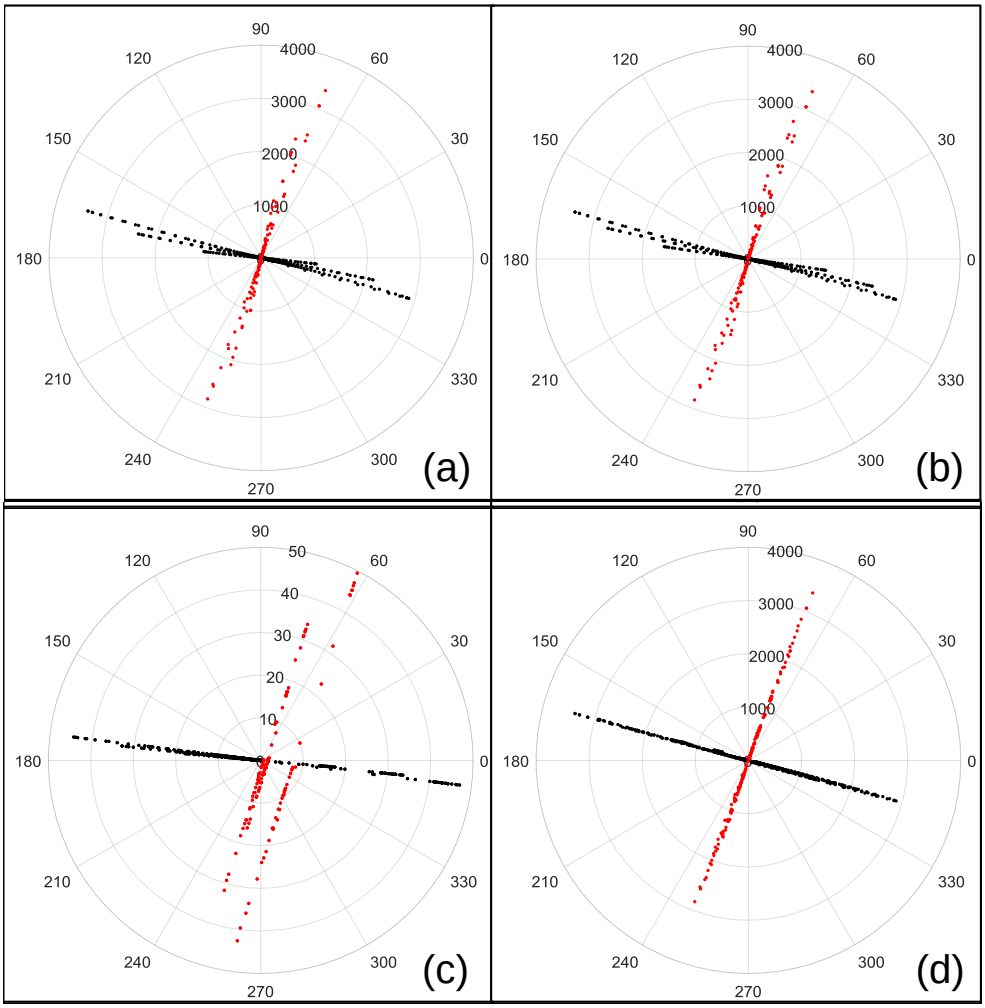

Figure 3.19.

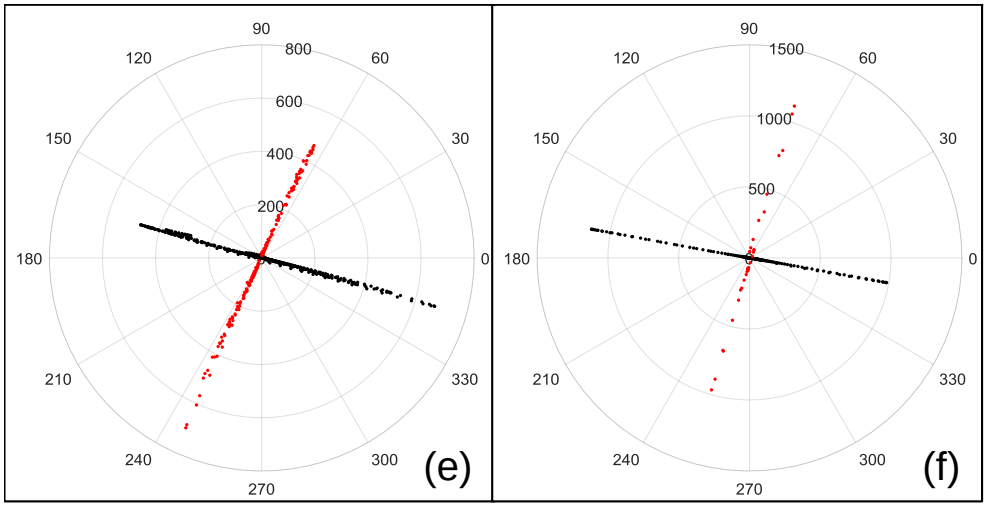

Figure 3.19: Phase plots for the air-tests: (a) co-axial coils with orthogonal fractures of different areas, (b) co-axial coils with orthogonal fractures of different aspect ratio, (c) co-planar coils with orthogonal fractures of different aspect ratio, (d) co-axial coils with different orientation of fractures, (e) cross-polarized coils with different orientation of fractures, and for the near-surface test (f) co-axial coils with the orthogonal fracture. Black and red dots identify the numerical simulations and field measurements, respectively.

3.4.4. Signal to Noise Ratio

In the previous magnitude plots, results are shown with average values at each sampling point. In this section, the variation of total signals with respect to their magnitude is shown for some specified cases (Fig. 3.20).

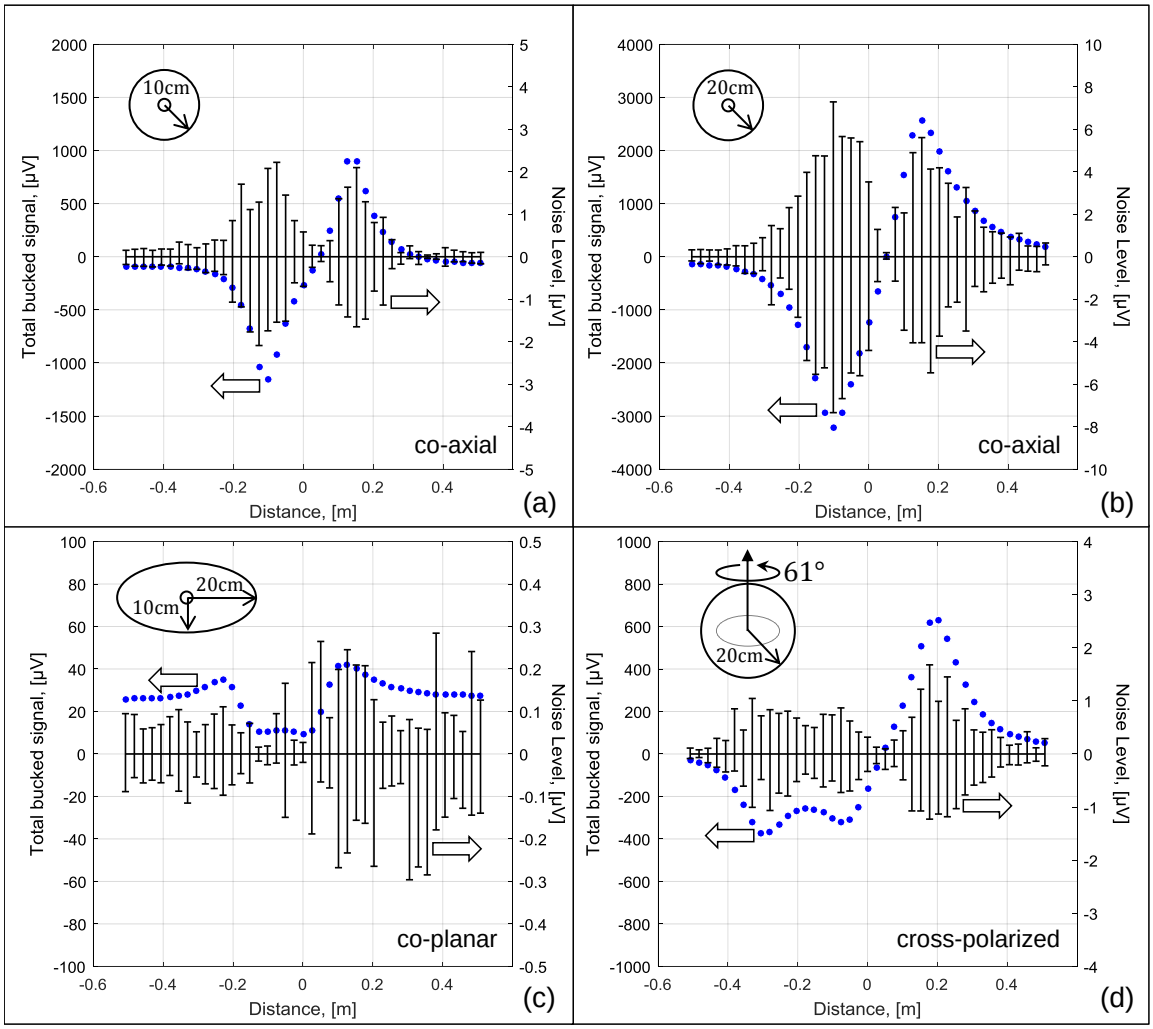

Figure 3.20: Signal to noise ratio of air tests: (a) co-axial measurements with 10 cm radius symmetric and orthogonal fracture model; (b) co-axial measurements with 20 cm radius symmetric and orthogonal fracture model; (c) co-planar measurements with 20 cm major and 10 cm minor radius elliptical and orthogonal fracture model; and (d) cross-polarized measurement with 20 cm radius and 61˚ rotated fracture model; the magnitude of total bucked signals is shown on the left axis and the variation of magnitude on the right axis.

As can be seen from Fig. 3.20, the variation of total signals is dependent on its magnitude. As the magnitude of the signal increases, the variation increases as well with the signal to noise ratio being more than 100 for all coil configurations. The same type of

plot for the near surface field test is shown in Fig. 3.21 where the signal to noise ratio is more than 100 again. Based on the results of this section, we will include one percent noise in the inversion analyses presented in the next chapter.

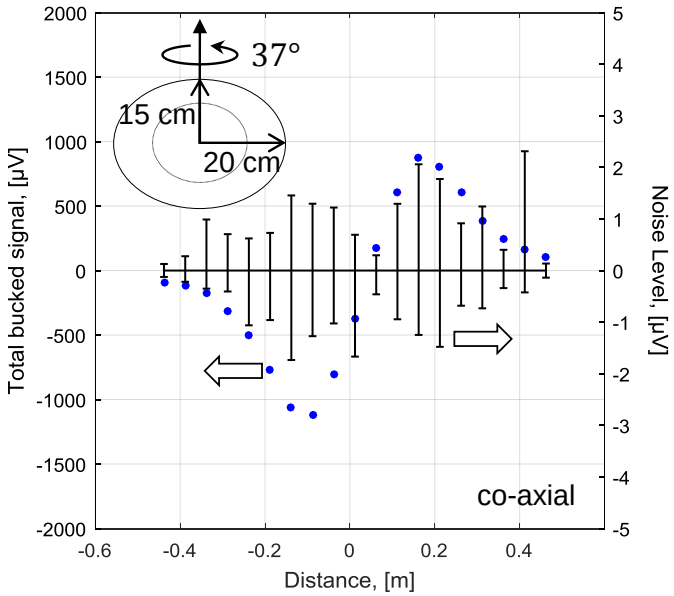

Figure 3.21: Signal to noise ratio of near-surface field test: co-axial measurements with the fracture model shown in Fig. 3.10; the magnitude of total bucked signals is shown on the left axis and the variation of magnitude on the right axis.

3.5. CONCLUSION

A prototype fracture diagnostics tool, consisting of co-axial, co-planar, and cross-polarized configurations of transmitter and receiver coils operated at 1 kHz, was built. Initial tests have been conducted to confirm the component properties and detectability range. Then, the prototype tool was tested in-air using a specially designed experimental setup with scaled targets that emulate propped hydraulic fractures. Tests were also conducted with the target buried underground in a near-surface trench. The measured results for both in-air and near-surface tests were in excellent agreement with those

simulated by the integral equation-based numerical model (average relative differences of less than 3% with a maximum difference of 10%). This agreement increases the confidence in the results of existing numerical studies which also cover conditions beyond those considered in the experiments. The high signal to noise ratios (over 100) of the measured signals indicate that, indeed, an EM induction tool can be used to extract the propped length (or area), orientation and height of propped hydraulic fractures in open-hole applications.

Each pair of transmitters and receivers exhibits sensitivity to different properties of conductive fractures. The co-axial coil configuration signals are strong (>100 μV) and highly sensitive to the fracture's surface area (or length). A combination of signals from the co-axial and cross-polarized configurations (both >100 μV) can enable estimation of the fracture's dip-angle. The co-planar configuration signals, however, are of relatively lower magnitude (only >10 μV) and, while theoretically are sensitive to the fractures' aspect ratios, might be too low to be sensed in a realistically noisy environment. While the design of (x, y)-oriented transmitter coils that can deliver greater power is challenging, due to geometrical constraints and heating considerations, improved sensitivity to the aspect ratio may be obtained by modifying the tool's design and operating mode, as will be explored in Chapter 5. Further research in Chapter 4 is dedicated to the development of parametric inversion techniques tailored to such tools.

Lastly, for the largest tested fracture model (circular model with 20 cm radius and orthogonal orientation), the scattered differential signals are approximately 100 times stronger than those produced by a circular hydraulic fracture of 1 m radius, 5 mm thickness (if the coil spacing is 1 meter, it can investigate fractures of ~1 meter radius) and the effective conductivity of 333 S/m (Zhang et al., 2016). However, the tool is expected to be operated downhole with a larger power supply, several hundred $A \cdot m^2$

(Heagy and Oldenburg, 2013) giving rise to greater currents. As a result, in the field, signal levels for short spacing coil couples are going to be close to those obtained in this experiment.

3.6. NOMENCLATURE

Symbol	definition	unit
A	cross-sectional area	m^2
B	magnetic field	mG
G	conductance	S
H	magnetic flux density	A-m
I	peak current	A
M	magnetic dipole moment	$A \cdot m^2$
N	number of turns	-
N^i	induction number	-
P	power	W
R	resistance	Ω
U, V	voltage	V
X, Y	lock-in amplifier readings	V
$\Re$	real component of detected signal	V
$\Im$	imaginary component of detected signal	V
d	diameter	m
f	frequency	Hz
h	the height of a coil	m
j	complex number	-
k	wave number	1-m
l	length	m
r	radius	m
t	thickness	m
u	orientation of receiver coil	-
w	weight factor	
v	orientation of transmitter coils	-
δ	skin depth	m
μ	magnetic permeability	H-m
μ_r	relative magnetic permeability	-
μ_o	free space magnetic permeability	H-m
ρ	resistivity	Ω·m
σ	conductivity	S-m

ω	angular frequency	Hz
SI derived unit	**definition**	**SI base units**
F	Farad	$s^4 \cdot A^2\text{-}m^2 \cdot kg$
T	Tesla	$kg\text{-}A \cdot s^2$
H	Henry	$kg \cdot m^2\text{-}s^2 \cdot A^2$
Hz	Hertz	1-s
Ω	Ohm	$kg \cdot m^2\text{-}s^3 \cdot A^2$
S	Siemens	$s^3 \cdot A^2\text{-}kg \cdot m^2$
V	Volt	$kg \cdot m^2\text{-}s^3 \cdot A$
W	Watt	$kg \cdot m^2\text{-}s^3$
CGS unit	**definition**	**SI base units**
G	Gauss	$1E\text{-}4[kg\text{-}A \cdot s^2]$

Chapter 4: INVERSION OF EM DATA TO OBTAIN FRACTURE GEOMETRY AND CONDUCTIVITY

In this chapter, we develop an inversion algorithm for the estimation of fracture geometry and conductivity. The main goal is to have a time efficient simulation tool where the same analysis can be carried out with real field data. The knowledge of the fracture geometry and conductivity will help to improve the efficiency of fracturing operations, and in the long run, it will help completion engineers to design operations with the optimum number of stages and clusters. The results presented in this chapter also provide insight into the resolution obtained with the low frequency induction tool.

We developed a simulated annealing and neighbor-approximation based stochastic inversion algorithm, and first, examined it with a testing function to tune the optimization parameters. Then, several cases were run to invert the "measured data" and appraise the estimation of different fracture parameters such as conductivity, size, dip-angle, etc. An approximation-based direct inversion technique is also proposed for orthogonal fractures to minimize the computation time. Lastly, the effect of neighbor fractures is evaluated, and the inversion algorithm is utilized to recover the fracture distribution along the well for different stages. In the computations, nominal values are used for the tool. Our inversion results are shown to be robust and in agreement with the true values. The hybrid inversion algorithm is shown in the Appendix of this dissertation.

4.1. LITERATURE REVIEW

After logging the well with the induction tool, information on the proppant distribution in the fracture can be extracted in two different ways. The more practical and computationally less intensive approach is the parametrization of fractures. Yang et al. (2016) used circular (or elliptical) fractures to characterize the hydraulic fractures and

utilized parametric inversion technique where the model parameters are evaluated independently in each iteration. This technique leads to a small number of model parameters increasing time efficiency. The other approach is the generation of a conductivity map which provides information about the secondary fracture branches. In this case, one challenge is the intensive computational time required for the 3D volumetric solution of Maxwell's equations. The other challenge is the solution of the inherently under-determined problem where the number of model parameters will be dependent on the resolution requirements. In this chapter, we have selected the first approach with the main difference from the previously mentioned study (Yang et al., 2016) being our application of the multidimensional stochastic inversion technique which is based on a simulated annealing and a neighbor-approximation methods.

Typically, stochastic inversion techniques randomly select a starting point in the model space and moves are decided based on control parameters. Simulated annealing (Fouskakis and Draper, 2002; Sen and Stoffa, 1995) uses temperature as a control parameter for the search direction and jump distance which decreases the randomness of movements. In this study, we start with multiple models, and we use the neighbor approximation (Sambridge, 1999) to benefit from the data history and to avoid additional forward model runs. The tuning parameters are 1) the cooling schedule, 2) the model population and 3) the number of iterations.

4.1.1. Tensor of Detected Signal

In previous studies, Yang et al. (2015) and Zhang et al. (2016), it was shown that any electromagnetic induction tool aimed at fully diagnosing hydraulic fractures requires the use of a tri-axial transmitter and receiver coil system where a 3×3 tensor is measured for the scattered voltage at each sampling point:

$$\begin{bmatrix} V^{xx} & V^{xy} & V^{xz} \\ V^{yx} & V^{yy} & V^{yz} \\ V^{zx} & V^{zy} & V^{zz} \end{bmatrix}_i \tag{4.1}$$

where i is the index of the sampling point. The following model parameters: conductance, area, aspect ratio (shape), and dip-angle are sensitive to the different coil orientations. Co-axial measurements (V_{zz}) are sensitive to the fracture cross-sectional area until a certain saturation point but cannot differentiate fractures of the same area with different shapes or dip-angles. The short spacing can detect small fractures but cannot distinguish large ones. The signals on the long spacing receiver are inherently weak but can distinguish large fractures. The saturation limits for the short and long coil spacings were shown to be 10 m^2 and 1000 m^2, respectively. Co-planar measurements (V_{xx} or V_{yy}) can differentiate axially symmetric fractures from asymmetric ones, but they were found to be weak in the previous chapter. Cross-polarized measurements (off-diagonal components) can quantify fracture dip-angle and become more pronounced as the dip-angle increases (Yang et al., 2015). For an accurate estimation of all model parameters, we suggest using a combination of various orientations. In this study, we define an objective function in such a way that it includes all the signals from different coil spacings and configurations.

4.2. INVERSION TECHNIQUES

In this chapter, we will show results for a mono-axial transmitter (axis oriented in the wellbore direction) and tri-axial receiver coils. Two strong signals are obtained from this transmitter-receiver coupling: co-axial and cross-polarized signals. They are used in the cost function as follows:

$$E = \left(E_{zz} + E_{yz}\right)^{\text{short}} + \left(E_{zz} + E_{yz}\right)^{\text{long}} \tag{4.2}$$

This cost function combines all four signals effectively and enables a global search on the fracture parameters. The signal levels in the long coil spacing are inherently weaker than that of short spacing. Therefore, signals are normalized as follows to get an equal weight on the cost function for the short and long spacing:

$$E_{uv} = \sum_i \left(\frac{\Delta U_{uv}^{\mathrm{sca},i} - \Delta \widetilde{U}_{uv}^{\mathrm{sca},i}}{\Delta \widetilde{U}_{uv}^{\mathrm{sca},i}} \right)^2 \tag{4.3}$$

The tilde refers to the measured (true or observed) data. Fig. 4.1 shows the error map for a fracture with 8 m radius, 100 S/m conductivity and 30˚ dip-angle calculated with Eq. 4.2 where it is clearly seen that there is a global minimum at the true model parameters. For all our presentations here, "calculated data" (differential signal without tilde in Eq. 4.3) is generated using coarser surface meshes, a node spacing factor of four (ref. Chapter 2). For the "measured data", finer surface mesh, a node spacing factor of ten, is used with an additional one percent random noise.

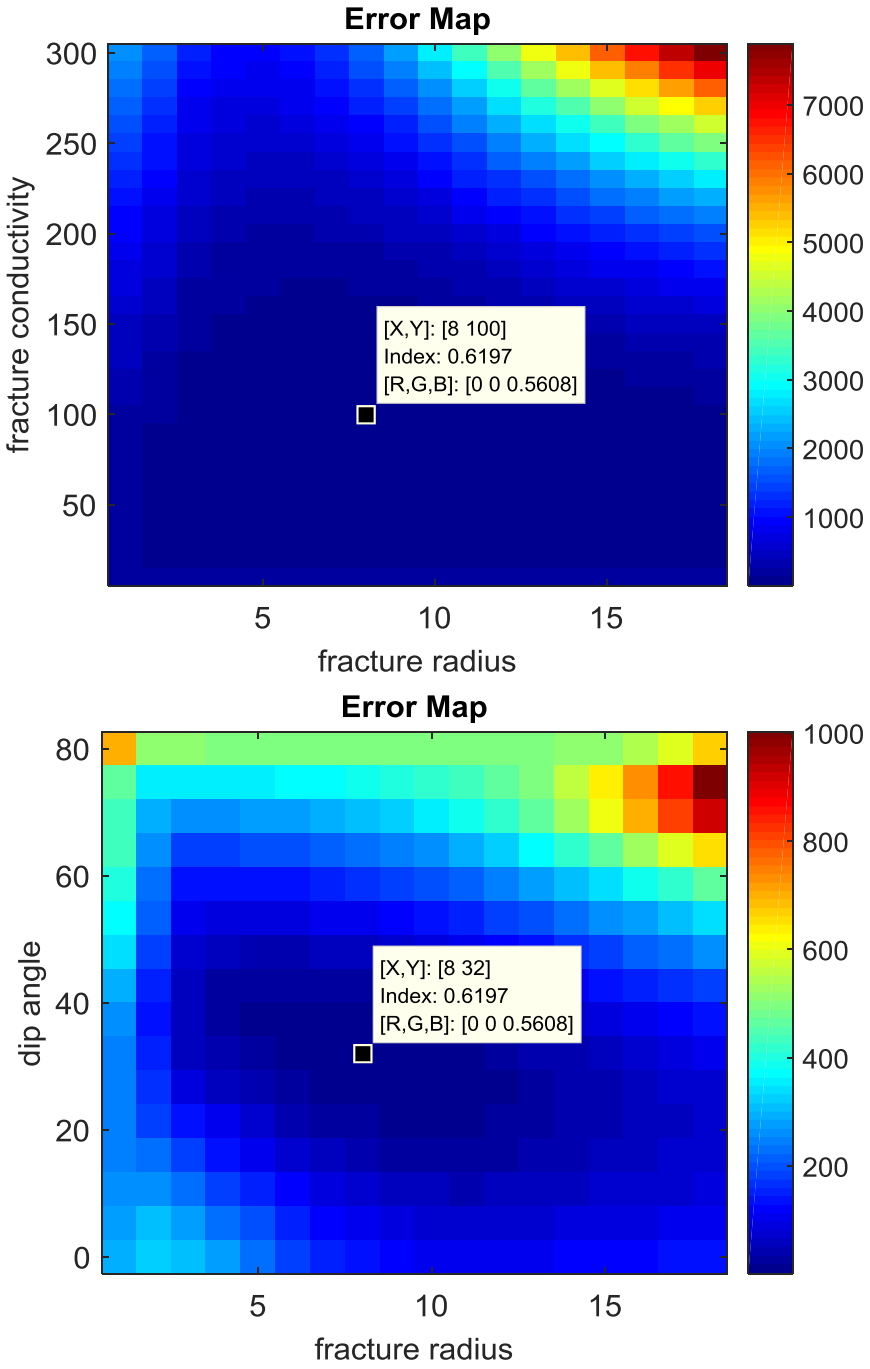

Figure 4.1: Error map calculated for the 8 m radius fracture with a thickness of 5mm, conductivity of 100 S/m and dip-angle of 30˚: upper plot is the fracture conductivity vs. fracture radius, and lower plot is the fracture dip-angle vs. fracture radius.

4.2.1. Derivative Free Directional Search

The main goal of the inversion algorithm is to minimize the error calculated using Eq. 4.2, and the work flow is outlined in Fig. 4.2. First, we define the limits for each individual model parameter. The lower bound is defined as $\mathbf{m}^{\min}$ and upper bound as $\mathbf{m}^{\max}$. Then the first population of models is randomly generated as follows:

$$\mathbf{m}^1 = \mathbf{m}^{\min} + r_{\mathrm{u}} \cdot \left(\mathbf{m}^{\max} - \mathbf{m}^{\min}\right) \tag{4.4}$$

where r_{u} is the random number generated from the uniform distribution. Errors for the population are then evaluated, and the production of new parameters for each model in the population is carried out as follows:

$$m_i^{\mathrm{new}} = m_i^{\mathrm{old}} \mp r_u \cdot T \cdot \Delta m_i \tag{4.5}$$

where T is the control temperature which gradually decreases according to the predefined schedule:

$$T = 0.01^{(i-1)/(N-1)} \tag{4.6}$$

When the iteration number, i is one, T is 1 and approaches 0.01 when i is equal to the maximum number of iterations which is shown with N in the equation above. The cooling schedule allows larger jumps at the beginning of the search and smaller jumps toward the end of the search. As a general rule, a faster cooling schedule may cause the solution to be stuck in a local minimum. A slower cooling schedule is more likely to find a global minimum at the cost of increasing the computation time.

To avoid additional forward model runs, due to the one-dimensional search, data history is used to approximate error to the closest neighbor point. The distance from the point of interest is calculated with the following equation:

$$\|m_{\mathrm{a}} - m_{\mathrm{b}}\| = \sqrt{\left((m_{\mathrm{a}} - m_{\mathrm{b}})^{\mathrm{T}} \cdot C \cdot (m_{\mathrm{a}} - m_{\mathrm{b}})\right)} \tag{4.7}$$

$$C_{ii} = \left(m_{i,max} - m_{i,min}\right)^{-2} \tag{4.8}$$

The condition of accepting a new point is defined as follows:

$$E(\mathbf{m}^{\text{new}}) \leq E\left(\mathbf{m}^{\text{old}}\right) \quad \text{or} \quad T > r_{\text{u}} \tag{4.9}$$

Here, the temperature (T) is used to decide whether to keep a larger error model or not. At the beginning of the search, we have a high chance of accepting new models with larger errors which decreases almost to zero toward the end of the search. Finally, the algorithm is terminated when the maximum number of iterations is achieved.

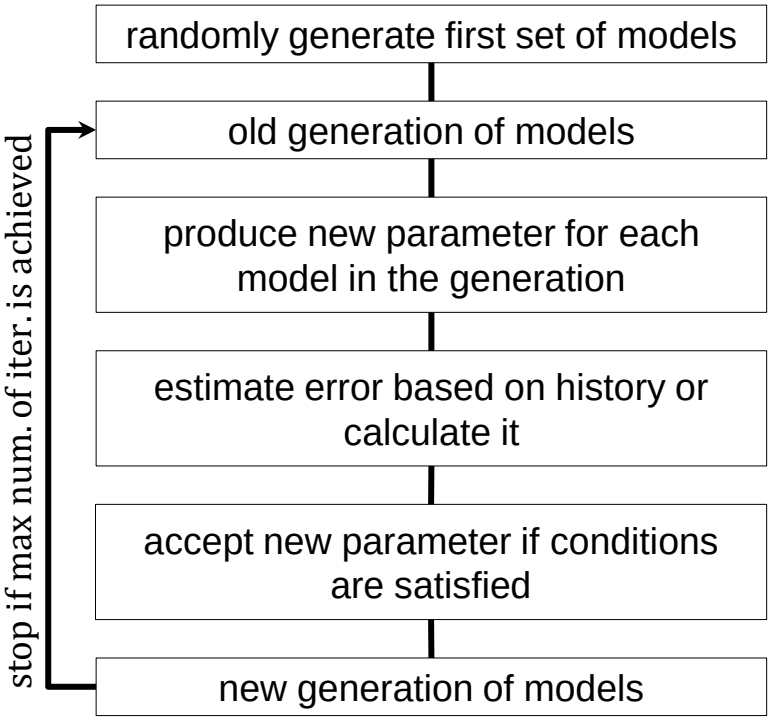

Figure 4.2: Flow diagram of simulated annealing and neighbor approximation based hybrid inversion algorithm.

To test the model the following equation is used as a testing function:

$$E = \left(1 - \prod_{i=1}^{N} \text{sign}\left(\text{sinc}(m_i)\right) \sqrt[4]{|\text{sinc}(m_i)|}\right)^2 \tag{4.10}$$

This testing function allows having a different number of model parameters, and Fig. 4.3 shows error plots for a one- and two-dimensional problem domain.

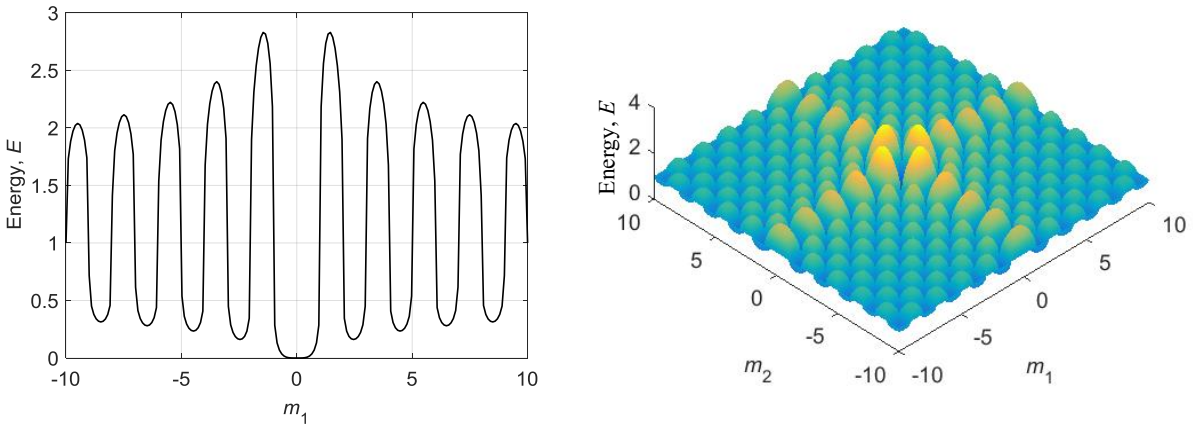

Figure 4.3: One- and two-dimensional plot of the testing function shown in Eq. 4.10.

The output of the algorithm for the test function is shown in Fig. 4.4. We start the search with 10 model samples. In the given iteration, the open black circles show errors for all models and the red filled circle is a model with the minimum error. In all dimensions, one to four, results converge to the global minima within 200 iterations. For the inversion analysis on synthetic data, we will use a smaller population and iterations to lower the computation time.

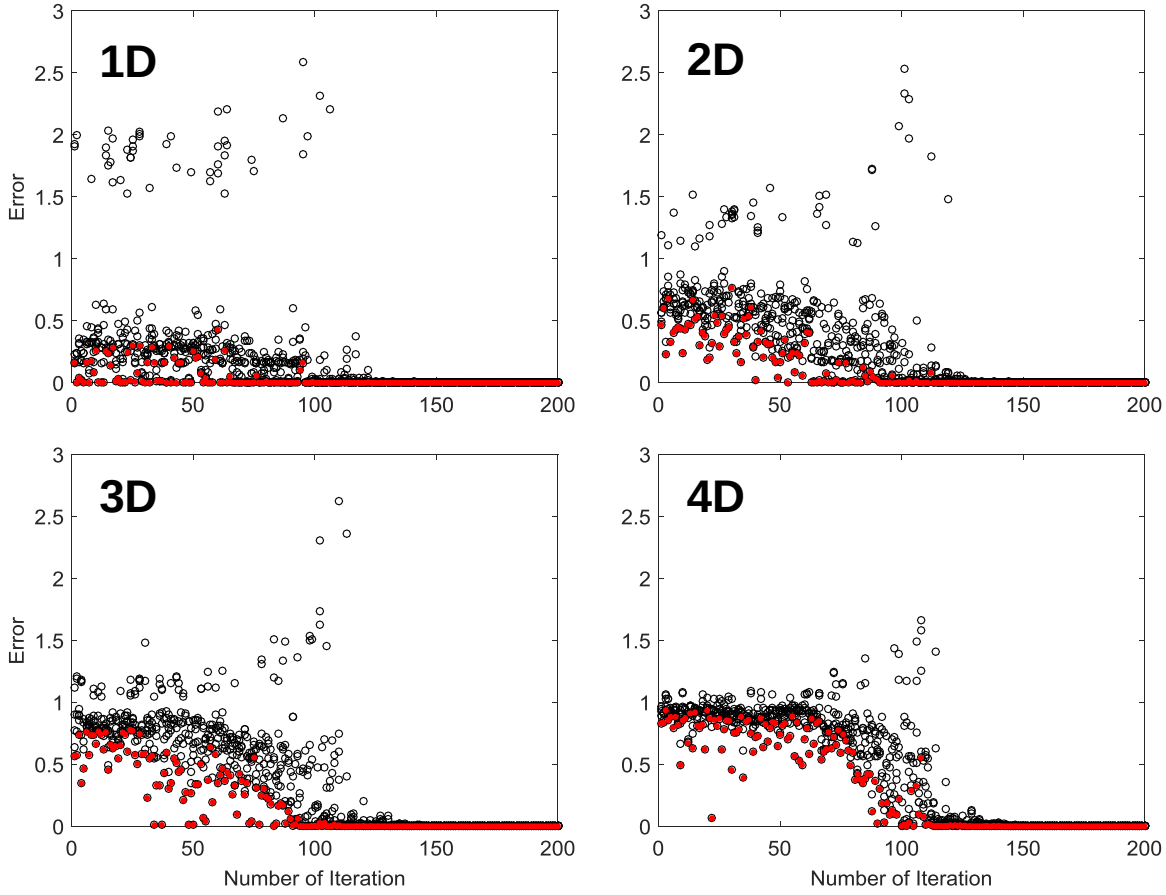

Figure 4.4: Inversion results for the test function in one, two, three, and four dimensions: open circles show errors for all models and red filled circles show a model with the minimum error in the given iteration.

4.2.2. Approximation Based Linear Regression

As discussed in Chapter 2, the approximation introduced in Eq. 2.36 has a linear relationship with the conductance. Implementing this equation into Eq. 2.25 and then into Eq. 1.1, the dependence of the received signal on the conductance for a given location of the tool will be as follows:

$$U_{zz,n}^{\mathrm{sca}} = -j\omega\mu_{\mathrm{o}} N_{\mathrm{rx}} A_{\mathrm{rx}} G \iint_{S} \nabla G_{\mathrm{R}}(\mathbf{r}_n, \mathbf{r}') \times \mathbf{E}^{\mathrm{inc}}(\mathbf{r}')\, dS' \tag{4.11}$$

where n is the receiver number and the differential signal is calculated by subtracting the two receiver signals. If we change the error function to:

$$E_{zz} = \sum_i \left(\Delta U_{zz}^{\mathrm{sca},i} - \Delta \tilde{U}_{zz}^{\mathrm{sca},i}\right)^2 \tag{4.12}$$

and if we take the derivative with respect to conductance, then we can calculate the conductance for the given geometry as follows:

$$G = \sum_i \left(\Delta \tilde{U}_{zz}^{\mathrm{sca},i} \frac{\partial \Delta U_{zz}^{\mathrm{sca},i}}{\partial G}\right) \Big/ \sum_i \left(\frac{\partial \Delta U_{zz}^{\mathrm{sca},i}}{\partial G}\right)^2 \tag{4.13}$$

Here, i is the sampling point number. This approach will be limited to orthogonal fractures and can be used to reduce the computation time required for the inversion analysis.

4.3. HYDRAULIC FRACTURE IMAGING

In this section, the proposed inversion algorithms are applied to single fracture models, and then an inversion strategy is proposed for use in the presence of neighbor fractures. For all results, the number of iterations is 100, the population is 5, and the number of model parameters is either 2 or 3 depending on the fracture under consideration. The first two model parameters are fracture conductivity and radius. If the observed data has significant signal levels on the cross-polarized configuration, the model parameters include dip-angle as well. Gaussian noise with a mean of one percent of the signal level is added to the "measured data" after calculating them with a node spacing factor of ten. In the inversion analyses, meshes are coarsened by selecting the node spacing factor to be four. Typical single- and multi-cluster analyses take 10 minutes and 10 hours, respectively.

4.3.1. Single Cluster Analysis

The stochastic inversion results for a single fracture inversion are shown in error figures and box charts. The figures show error values calculated with Eq. 4.2: at the given iteration number, the open circles show errors for all evaluated models, and the red filled circle shows a model with the minimum error. The box plots show the statistical information for the fifty lowest error models. In each box, the central mark indicates the median, and the bottom and top edges of the box indicate the 25th and 75th percentiles, respectively. The whiskers extend to the lower and upper adjacent values, and outliers are shown with the '+' symbol. The approximation based linear regression results are shown only for orthogonal fractures; lines of conductivity values calculated with Eq. 4.13 for short and long coil spacings is shown where the intersection point of lines refers to the estimated result.

4.3.1.1. Circular Fracture

In the first example, the true fracture model is an orthogonal circle with a radius of 8 m and a conductivity of 100 S/m. Fig. 4.5 shows the error and box plots: errors show a decreasing trend with the number of iterations, and the whiskers of both box plots cover the interval which includes the true parameters. The best inversion result (model with the lowest error) has a radius of 8.08 m and a conductivity of 100 S/m.

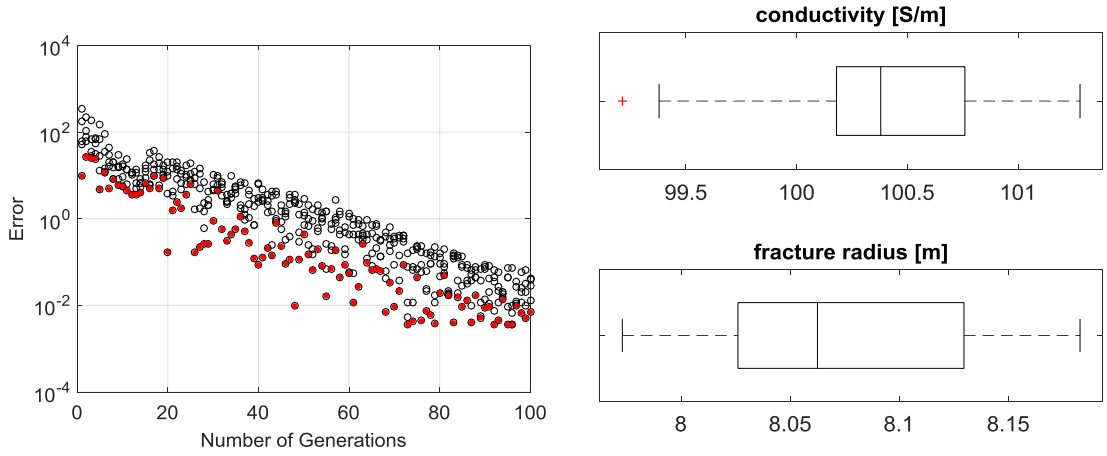

Figure 4.5: Inversion results for a circular and orthogonal fracture: true fracture model has the radius of 8 m and uniform conductivity of 100 S/m. Left figure shows a change in the error with the number of iterations: open circles show errors for all models and red filled circles show a model with the minimum error in the given iteration; and right figures show calculated conductivity and radius box plots for the best 50 cases.

Fig. 4.6 shows a comparison of the differential signals calculated for the true and best inverted models in both short and long coil spacings. As it can be seen in the plots, the curves are essentially indistinguishable showing an excellent agreement for both real and imaginary components.

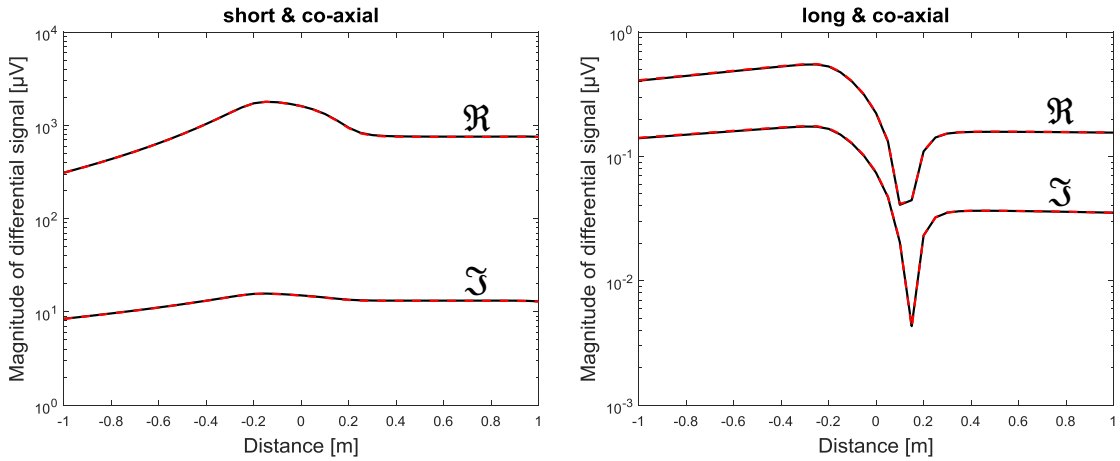

Figure 4.6: The comparison of true (solid black line) and the best inverted (dashed red line) differential signals for a circular and orthogonal fracture with uniform conductivity distribution: true fracture model has the radius of 8 m and constant conductivity of 100 S/m; differential signals are shown for a co-axial coil configuration in short (left) and long (right) coil spacings.

Fig. 4.7 shows results for an approximation based linear regression. The short and long spacing regression lines intersect at a radius of 8.1 m and a conductivity of 100 S/m, and these results are in a good agreement with the stochastic inversion results.

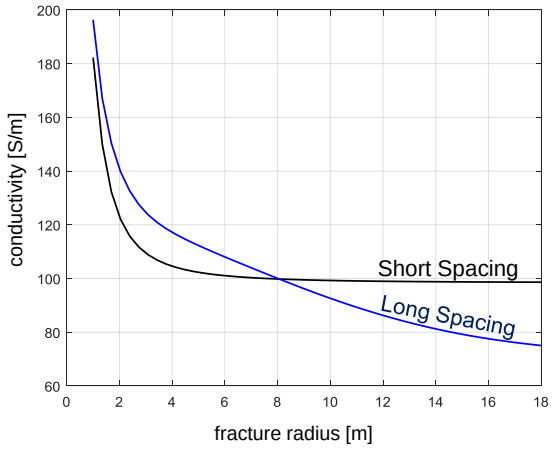

Figure 4.7: Approximation based inversion for a circular and orthogonal fracture: true fracture model has a radius of 8 m and a constant conductivity of 100 S/m; calculated conductivity values are shown for short (red) and long (blue) coil spacings.

4.3.1.2. Rotated Fracture

In this example, the true fracture model is a circle with a radius of 8 m, a constant conductivity of 100 S/m and a dip-angle of 30˚ (rotated about the vertical axis). Fig. 4.8 shows the error and box plots: errors show the same decreasing trend with the number of iterations, and the whiskers of all box plots cover the interval which includes the true parameters. The best inversion result (model with the lowest error) has a radius of 8.09m, a conductivity of 100S/m and a dip-angle of 30.2˚.

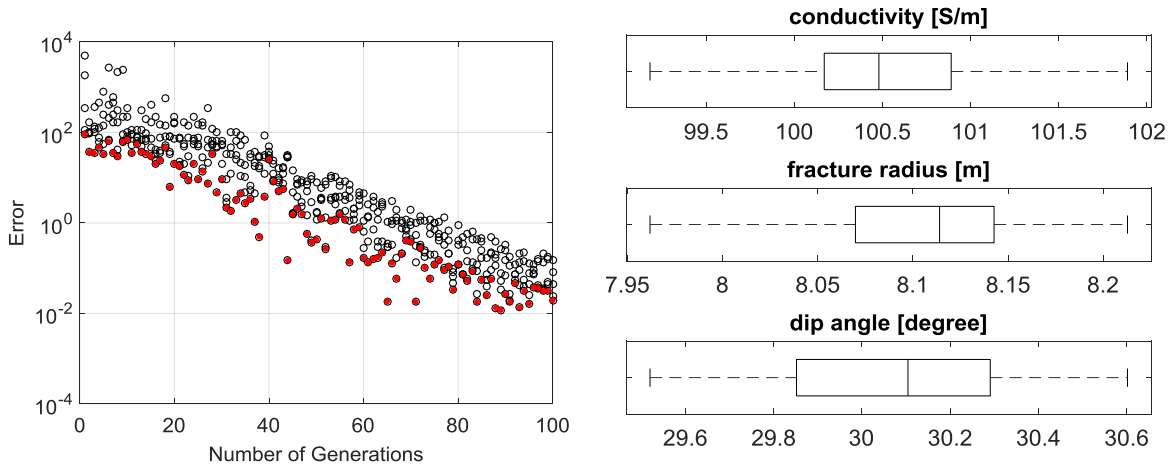

Figure 4.8: Inversion results for a circular and rotated fracture: true fracture model has a radius of 8 m, a uniform conductivity of 100 S/m and a dip-angle of 30^{o}. Left figure shows a change in the error with the number of iterations: open circles show errors for all models and red filled circles show a model with the minimum error in the given iteration; and right figures show calculated conductivity, radius and dip-angle box plots for the best 50 cases.

Fig. 4.9 shows a comparison of the differential signals calculated for the true and best inverted models for both short and long coil spacing including both co-axial and cross-polarized configurations. As can be seen in the plots, the curves are in good agreement for both real and imaginary components for all spacings and configurations.

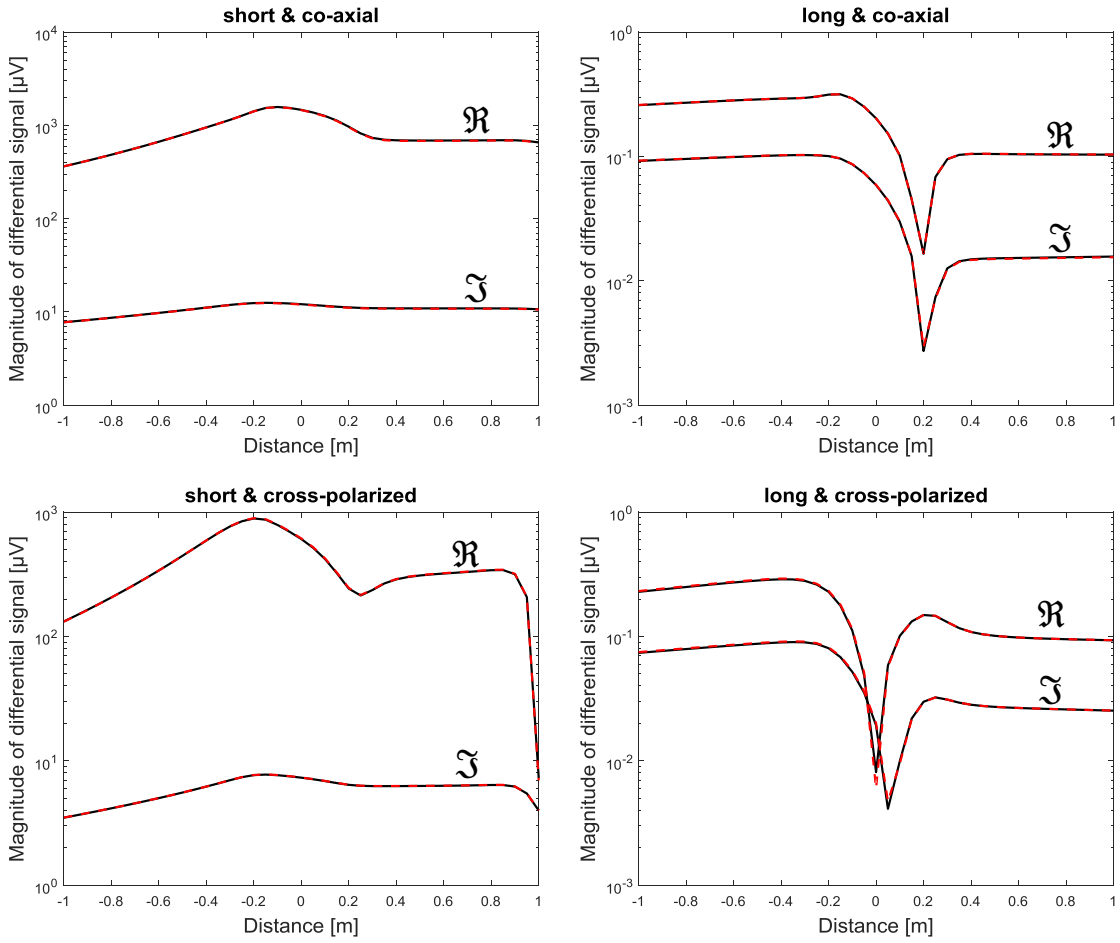

Figure 4.9: The comparison of true (solid black line) and the best inverted (dashed red line) differential signals for a circular and rotated fracture with uniform conductivity distribution: true fracture model has a radius of 8 m, a constant conductivity of 100 S/m and a dip-angle of 30°; differential signals are shown for co-axial (upper row) and cross-polarized (lower row) coil configurations in short (left column) and long (right column) coil spacings.

4.3.1.3. Elliptical Fracture

In this example, the true fracture model is an orthogonal ellipse with a major radius of 8 m, an aspect ratio of 1.5 and a conductivity of 100 S/m. Fig. 4.10 shows the error and box plots: errors show a decreasing trend with the number of iterations, and the whiskers of the conductivity box plot cover the interval which includes the true

parameter. For the box plot of fracture radius, however, whiskers include the effective radius which is defined as the square root of the product of major and minor radii. The model with the lowest error is a circle with a radius of 6.46 m and a conductivity of 100S/m.

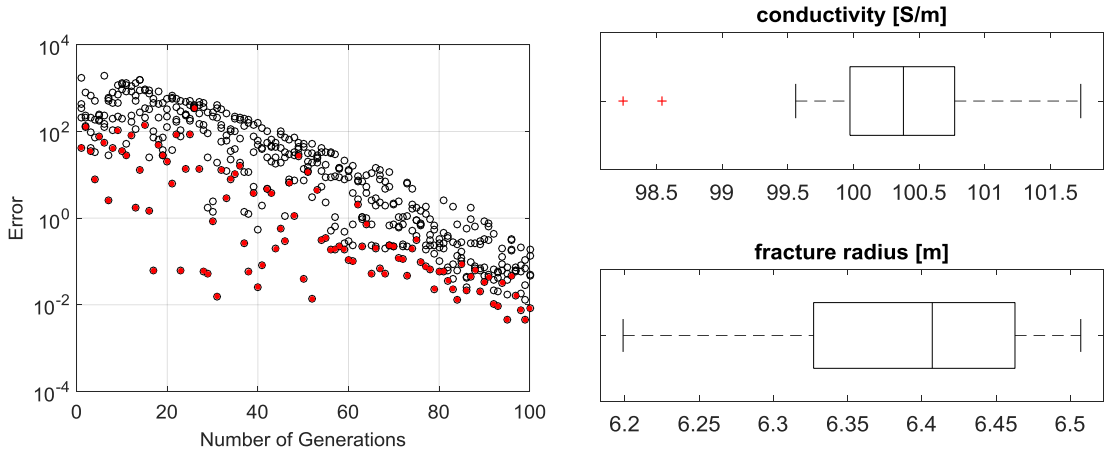

Figure 4.10: Inversion results for an elliptical and orthogonal fracture: true fracture model has a major radius of 8 m, an aspect ratio of 1.5 and a constant conductivity of 100 S/m. Left figure shows a change in the error with the number of iterations: open circles show errors for all models and red filled circles show a model with the minimum error in the given iteration; and right figures show calculated conductivity and radius box-plots for the best 50 cases.

Fig. 4.11 compares the differential signals calculated for the true and best inverted models in both short and long coil spacings. It shows very good agreement for both real and imaginary components.

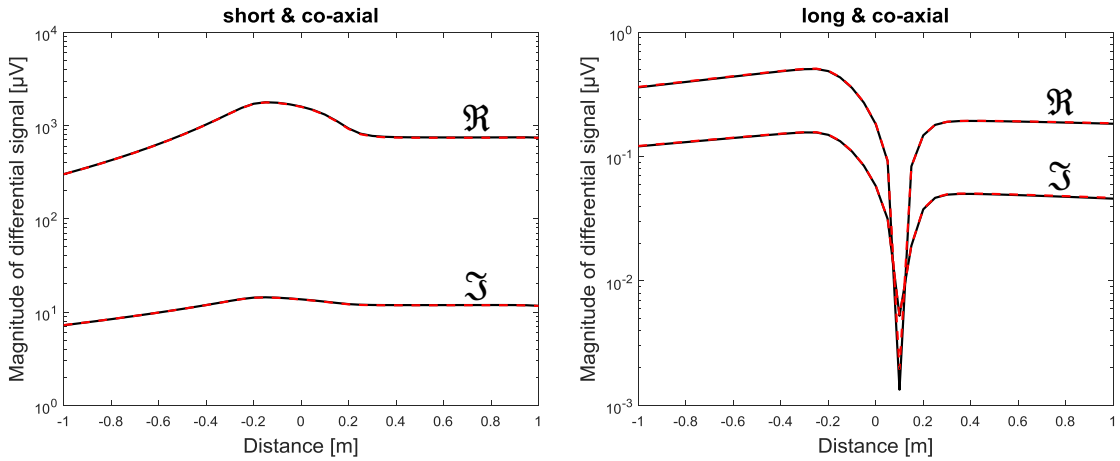

Figure 4.11: The comparison of true (solid black line) and the best inverted (dashed red line) differential signals for an elliptical and orthogonal fracture with uniform conductivity distribution: the true major radius is 8 m, the aspect ratio is 1.5 and the conductivity is 100 S/m. Differential signals are shown for a co-axial coil configuration in short (left) and long (right) coil spacings.

Fig. 4.12 shows results for the approximation based linear regression. The short and long spacing regression lines intersect at a radius of 6.4 m and a conductivity of 100 S/m, and these results are in a good agreement with the stochastic inversion results.

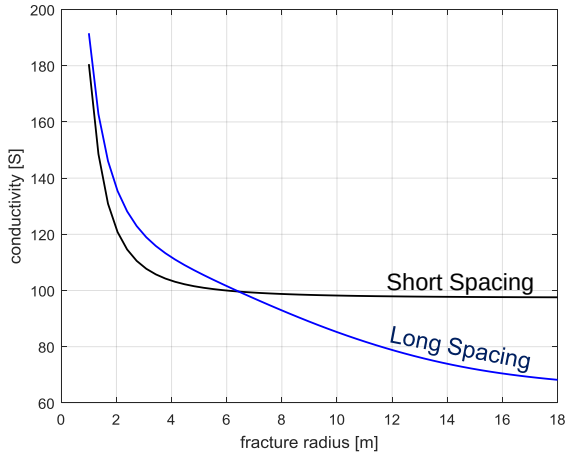

Figure 4.12: Approximation based inversion for an elliptical and orthogonal fracture: the true fracture model has a major radius of 8 m, an aspect ratio of 1.5 and a constant conductivity of 100 S/m; calculated conductivity values are shown for short (red) and long (blue) coil spacings.

To see the effect of rotation in the inversion of elliptical fractures, we run the true model with a major radius of 8 m, an aspect ratio of 1.5, a conductivity of 100 S/m and a dip-angle of 30˚ (rotated about the *x*-axis). Fig. 4.13 shows the error and box plots: errors show a decreasing trend with the number of iterations, and the whiskers of conductivity and dip-angle box plots cover the interval which includes the true model parameters. For the fracture radius box plot, however, whiskers cover the range for an effective radius. The model with the lowest error is a circle with a radius of 6.47 m, a conductivity of 102 S/m and a dip-angle of 31˚.

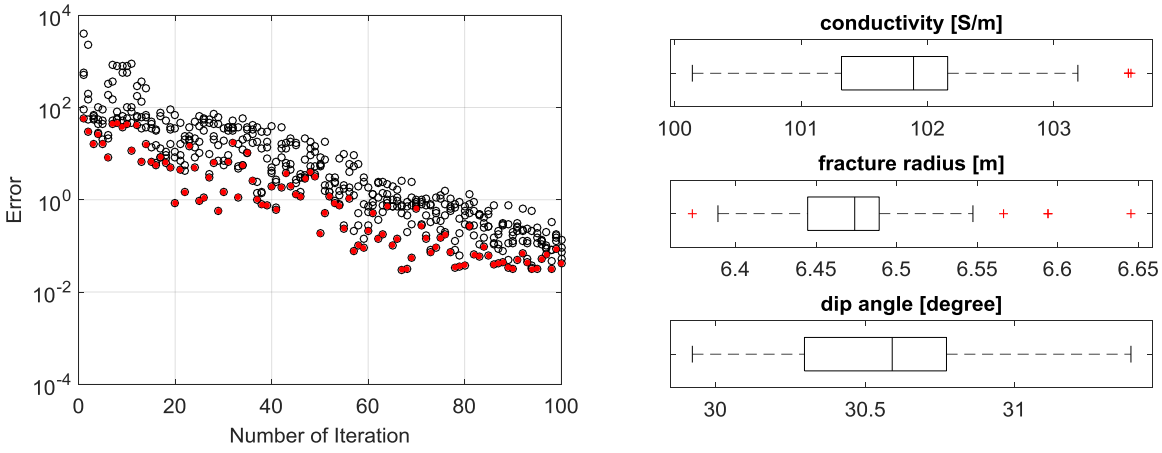

Figure 4.13: Inversion results for an elliptical and rotated fracture: the true fracture model has a major radius of 8 m, an aspect ratio of 1.5, a conductivity of 100 S/m, and a dip-angle of 30˚. Left figure shows a change in the error with the number of iterations: open circles show errors for all models and red filled circles show a model with the minimum error in the given iteration; and right figures show calculated conductivity, radius and dip-angle box plots for the best 50 cases.

Fig. 4.14 shows the comparison of the differential signals calculated for the true and best inverted models in both short and long coil spacings including both co-axial and cross-polarized configurations. It shows very good agreement for both real and imaginary components for all combinations.

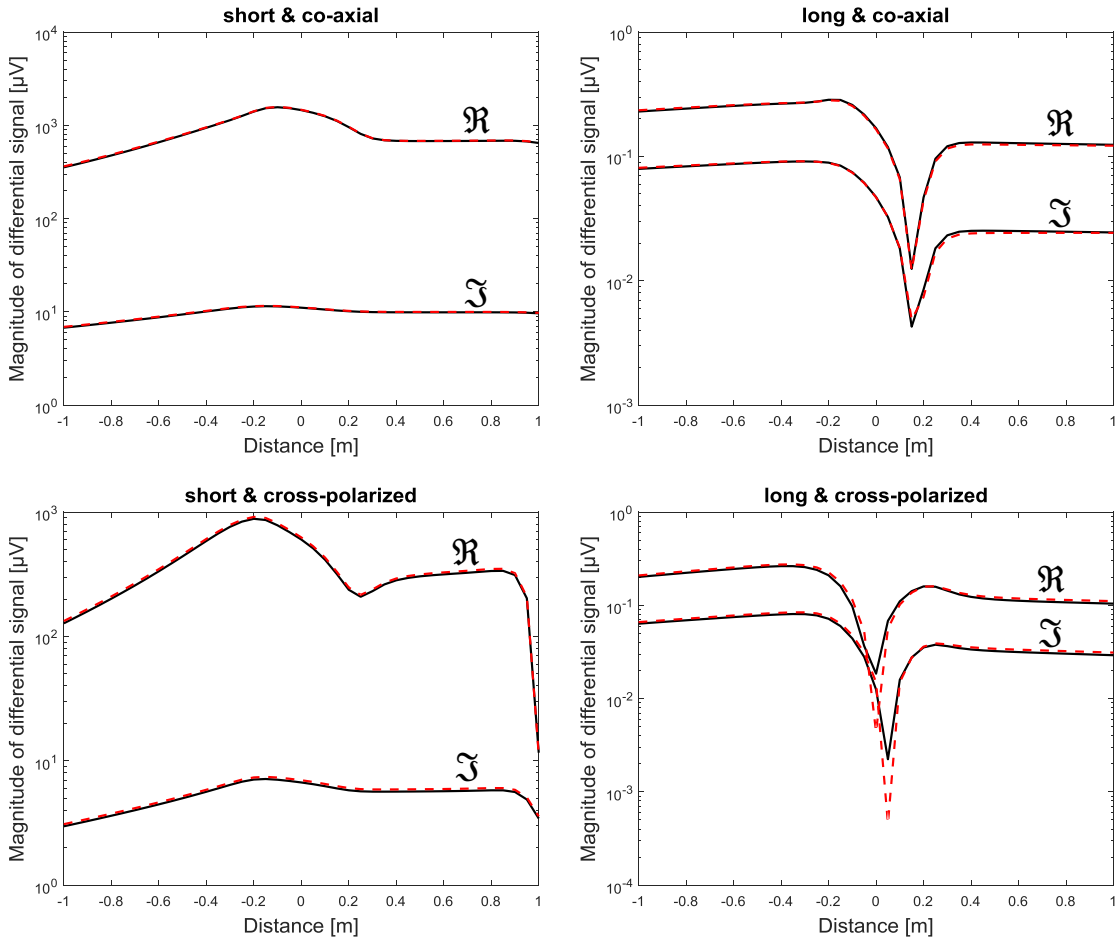

Figure 4.14: The comparison of true (solid black line) and the best inverted (dashed red line) differential signals for an elliptical and rotated fracture with uniform conductivity distribution: the true fracture model has a major radius of 8 m, an aspect ratio of 1.5, a constant conductivity of 100 S/m, and a dip-angle of 30˚; differential signals are shown for co-axial (upper row) and cross-polarized (lower row) coil configurations in short (left column) and long (right column) coil spacings.

4.3.1.4. Conductivity Distribution

In this example, the true fracture model is a circle with a radius of 8 m, and its conductivity decreases linearly in the radial direction (Fig. 4.15); the conductivity is 100 S/m at the wellbore and 0 S/m at the fracture tip.

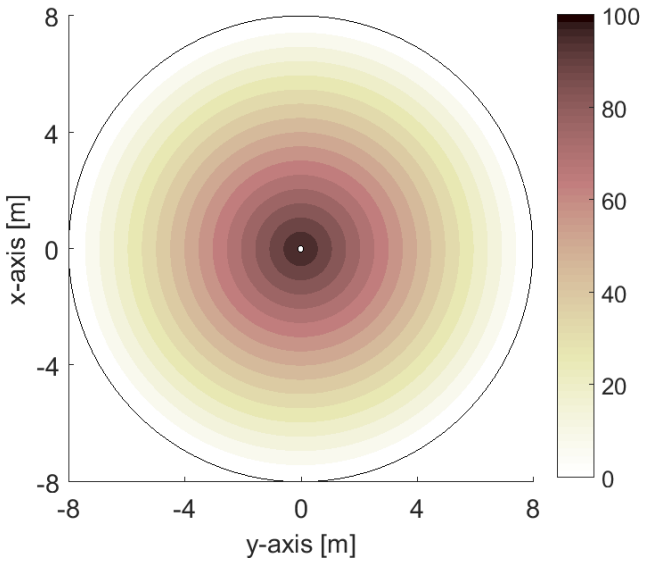

Figure 4.15: A fracture model with varying conductivity: conductivity at the wellbore is 100 S/m and 0 S/m at the fracture tip, decreasing linearly.

Fig. 4.16 shows the error and box plots: errors show a decreasing trend with the number of iterations, and the whiskers of box plots cover the interval which includes the effective parameters. The model with the lowest error is a circle with a radius of 4.37 m and a constant conductivity of 85 S/m.

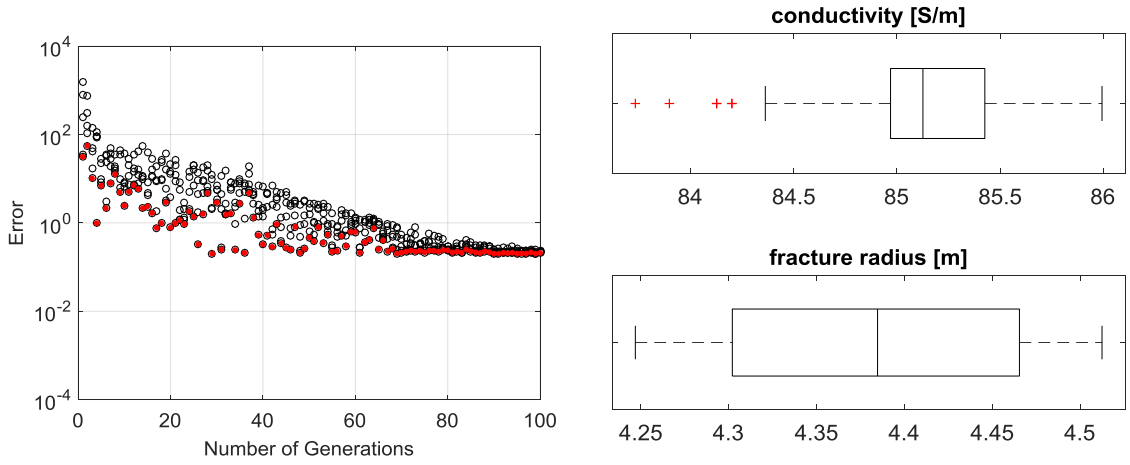

Figure 4.16: Inversion results for a circular and orthogonal fracture with varying conductivity: the true fracture model has a radius of 8 m, and the conductivity at the wellbore is 100 S/m and 0 S/m at the fracture tip, decreasing linearly. The left figure shows a change in the error with the number of iterations: open circles show errors for all models and red filled circles show a model with the minimum error in the given iteration; and right figures show calculated conductivity and radius box plots for the best 50 cases.

Fig. 4.17 shows a comparison of the differential signals calculated for the true and best inverted models in both short and long coil spacings. It shows a good agreement for both real and imaginary components.

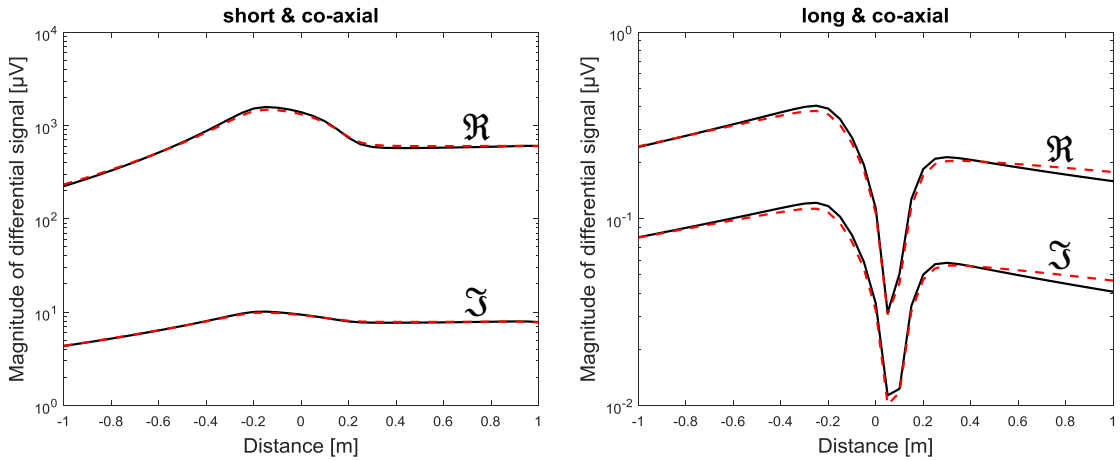

Figure 4.17: The comparison of true (solid black line) and the best inverted (dashed red line) differential signals for a circular and orthogonal fracture with varying conductivity: the true fracture model has a radius of 8 m, and the conductivity at the wellbore is 100 S/m and 0 S/m at the fracture tip, decreasing linearly. Differential signals are shown for a co-axial coil configuration in short (left) and long (right) coil spacings.

Fig. 4.18 shows results for the approximation based linear regression. The short and long spacing regression lines intersect at the radius of 4.5 m and conductivity of 86 S/m, and these results are in a good agreement with the stochastic inversion results.

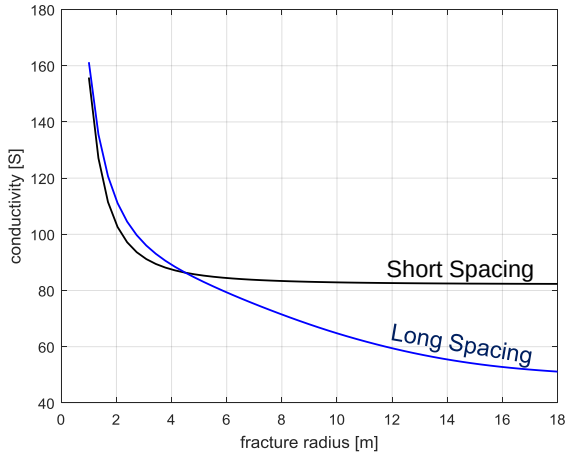

Figure 4.18: Approximation based inversion for a circular and orthogonal fracture with varying conductivity: the true fracture model has a radius of 8 m, and the conductivity at the wellbore is 100 S/m and 0 S/m at the fracture tip, decreasing linearly; calculated conductivity values are shown for short (red) and long (blue) coil spacings.

To see the effect of rotation in the inversion of fractures with varying conductivity, we ran the true circular fracture model with a radius of 8 m and a dip-angle of 30˚ (rotated about the *x*-axis). The conductivity at the wellbore is 100 S/m, and it is decreasing linearly to 0 S/m at the fracture tips. Fig. 4.19 shows the error and box plots: errors show a decreasing trend with iteration numbers, and the whiskers of the dip-angle box plot cover the interval which is very close to the true parameter. For the box plot of fracture radius and conductivity, however, whiskers cover the range which includes the effective parameters. The inverted model with the lowest error has a dip-angle of 29˚, a radius of 4.57 m and a constant conductivity of 84 S/m.

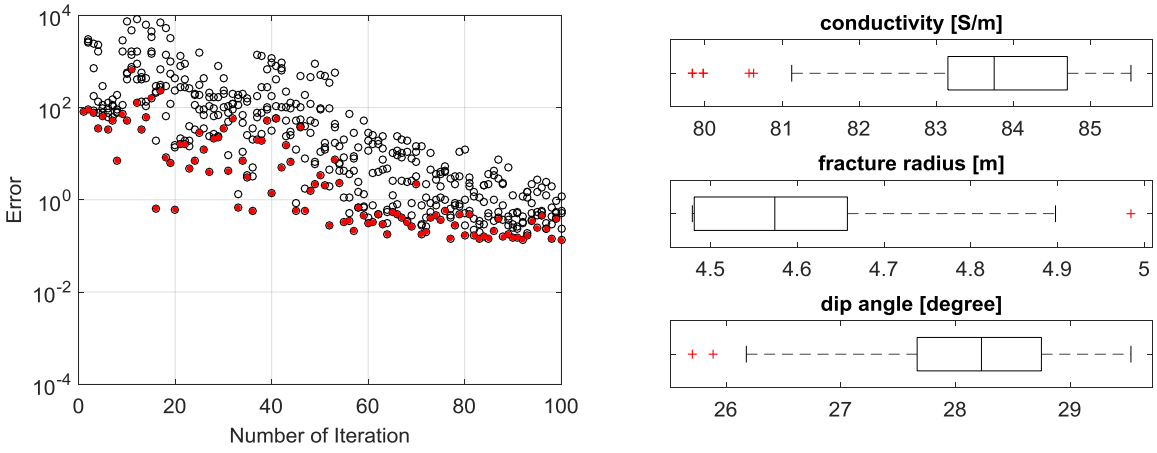

Figure 4.19: Inversion results for a circular and rotated fracture with varying conductivity: the true fracture model has a radius of 8 m and a dip-angle of 30˚, and the conductivity at the wellbore is 100 S/m and 0 S/m at the fracture tip decreasing linearly. The left plot shows a change in the error with the number of iterations: open circles show errors for all models and red filled circles show a model with the minimum error in the given iteration; and right figures show calculated conductivity, radius and dip-angle box plots for the best 50 cases.

Fig. 4.20 compares the differential signals computed for the true and best inverted models in both short and long coil spacings with both co-axial and cross-polarized configurations. The results of both models show very good agreement for both real and imaginary components.

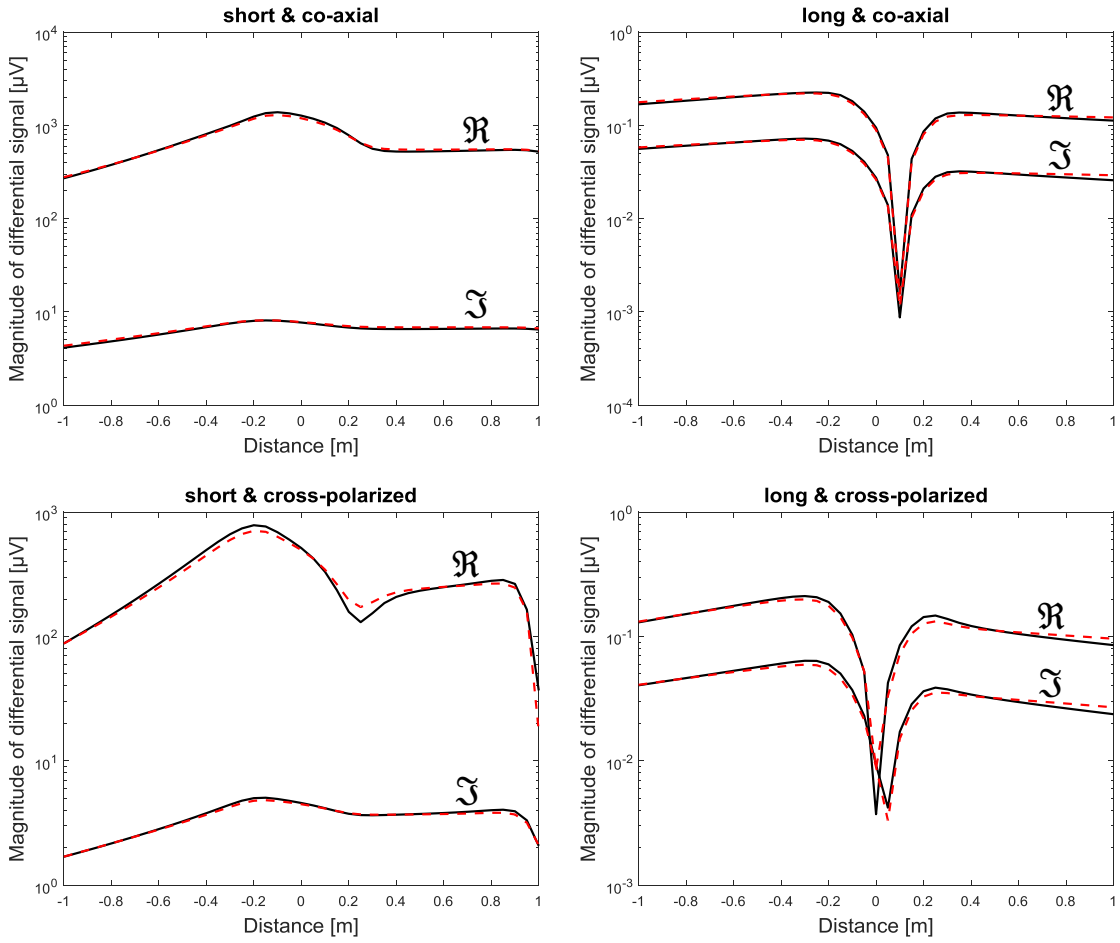

Figure 4.20: The comparison of true (solid black line) and the best inverted (dashed red line) differential signals for a circular and rotated fracture with varying conductivity: the true fracture model has a radius of 8 m and a dip-angle of 30˚, and the conductivity at the wellbore is 100 S/m and 0 S/m at the fracture tip, decreasing linearly; differential signals are shown for co-axial (upper row) and cross-polarized (lower row) coil configurations in short (left column) and long (right column) coil spacings.

4.3.1.5. Heterogeneous Background Conductivity

All the previous forward/inversion models were run with homogeneous background (rock) conductivity. In this section, we simulate heterogeneous background conductivity using the axial hybrid method. Adopting the layering and meshing scheme shown in Fig. 2.13, the uniform region of the mesh is selected between -1 and 1 m with

10 cm intervals. The computation domain is truncated at 100 m on both sides with the grid size ratio of 1.25 in the expanding region. At every grid, in each of the three layers, we use a randomly selected conductivity between 0 and 1 S/m where the overall mean conductivity is 0.49 S/m. Fig. 4.21 shows the primary signals for the formation with the described conductivity properties.

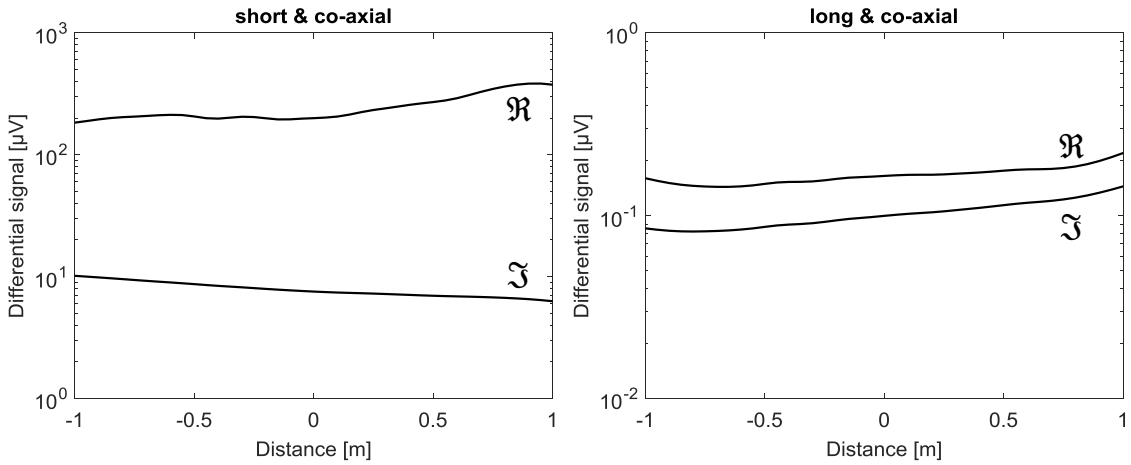

Figure 4.21: Tool response to the heterogeneous background formation; no-fracture case: real and imaginary components of primary signals are shown for co-axial coil configuration in short (left) and long (right) coil spacings.

After introducing a fracture model to the formation with the background conductivity properties described above, we simulate the tool response and subtract the non-fracture case response. The true model of the fracture is an orthogonal circle with a radius of 8 m and a conductivity of 100 S/m. We then run the inversion algorithm with the background (rock) formation conductivity of 0.49 S/m. Fig. 4.22 shows the error and box plots: errors show a decreasing trend with the iteration number, and the whiskers of both box plots cover the intervals which include the true parameters. The model with the lowest error has a radius of 8.1 m and a conductivity of 99.4 S/m.

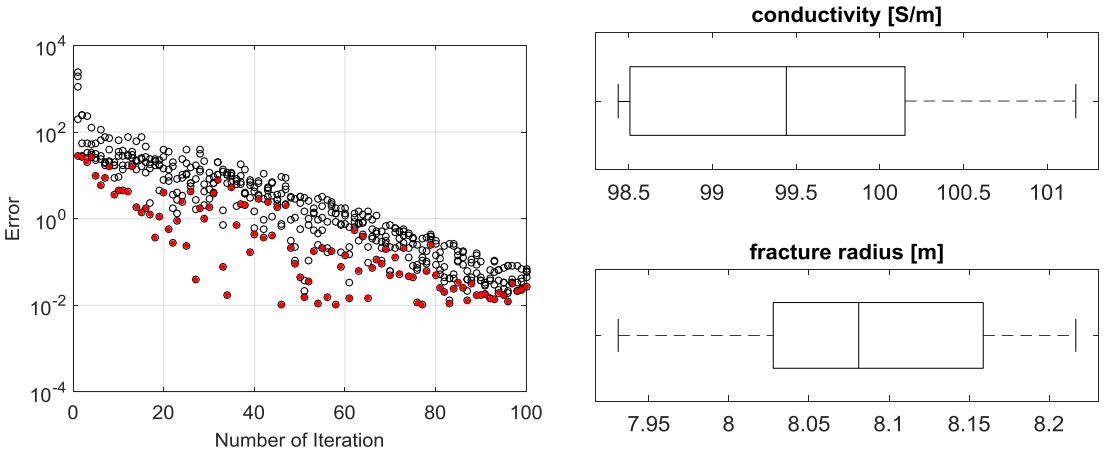

Figure 4.22: Inversion results for a circular and orthogonal fracture in the heterogeneous formation conductivity: true fracture model has a radius of 8 m and a uniform conductivity of 100 S/m. Left plot shows a change in the error with the number of iterations: open circles show errors for all models and red filled circles show a model with the minimum error in the given iteration; and the right figures show calculated conductivity and radius box plots for the best 50 cases.

Fig. 4.23 compares the differential signals computed for the true and best inverted models in both short and long coil spacings. The results show good agreement for both real and imaginary components.

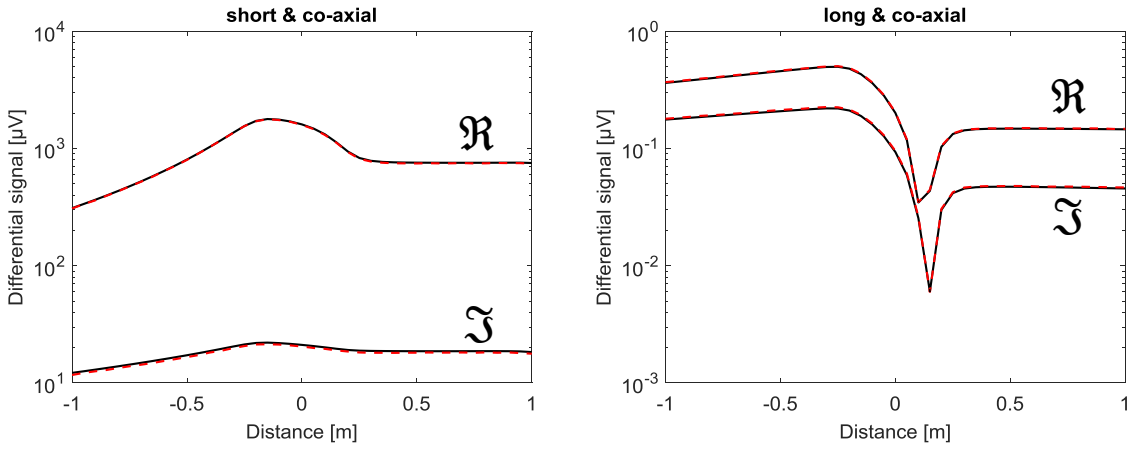

Figure 4.23: The comparison of true (solid black line) and the best inverted (dashed red line) differential signals for a circular and orthogonal fracture in a heterogeneous formation conductivity: true fracture model has the radius of 8 m and uniform conductivity of 100 S/m. Differential signals are shown for a co-axial coil configuration in short (left) and long (right) coil spacings. Measurements with and without fracture are subtracted for the true differential signals; and for the best inverted signals, average formation conductivity is used in the simulation.

This exercise shows the importance of an accurate subtraction of signals before and after fracturing. If we repeat the same analyses without the subtraction, the obtained accuracy is very poor; the result will be a circular fracture with the radius of 2 m and conductivity of 150 S/m.

4.3.2. Multi-Cluster Analysis

In a typical hydraulic fracturing operation, there are more than 20 stages and every stage includes 3 to 10 perforation clusters. Each of these fractures will affect the signals received by the tool. To evaluate this effect, we run many cases varying the number of fractures. Then, we implement a multi-fracture inversion algorithm to get the distribution of proppant in each fracture.

4.3.2.1. Effect of Neighboring Fractures

After completing the single fracture analysis, we ran simulations for a fracturing stage while varying the number of propped fractures to estimate how the neighboring fractures affect the signals coming from the fracture of interest. Fig. 4.24 shows the index number for each fracture.

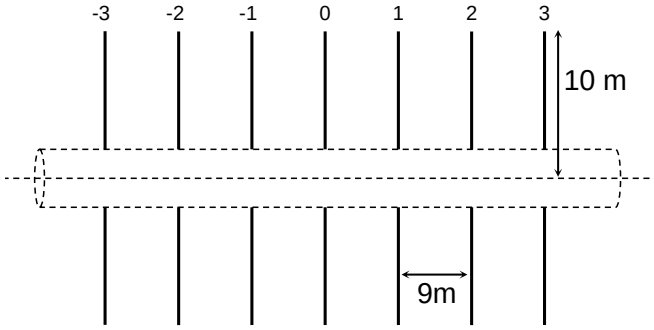

Figure 4.24: Wellbore model used for the evaluation of neighbor effects: fractures are circular and orthogonal with a radius of 10 m and a separation distance of 9 m; fractures are numbered with respect to the fracture of interest (middle fracture).

Fig. 4.25 plots three different cases: a) one neighboring fracture [-1 0 1], b) two neighboring fractures [-2 -1 0 1 2], and c) three neighboring fractures [-3 -2 -1 0 1 2 3]. The following plots show in-phase components of the received signals for short and long coil spacings.

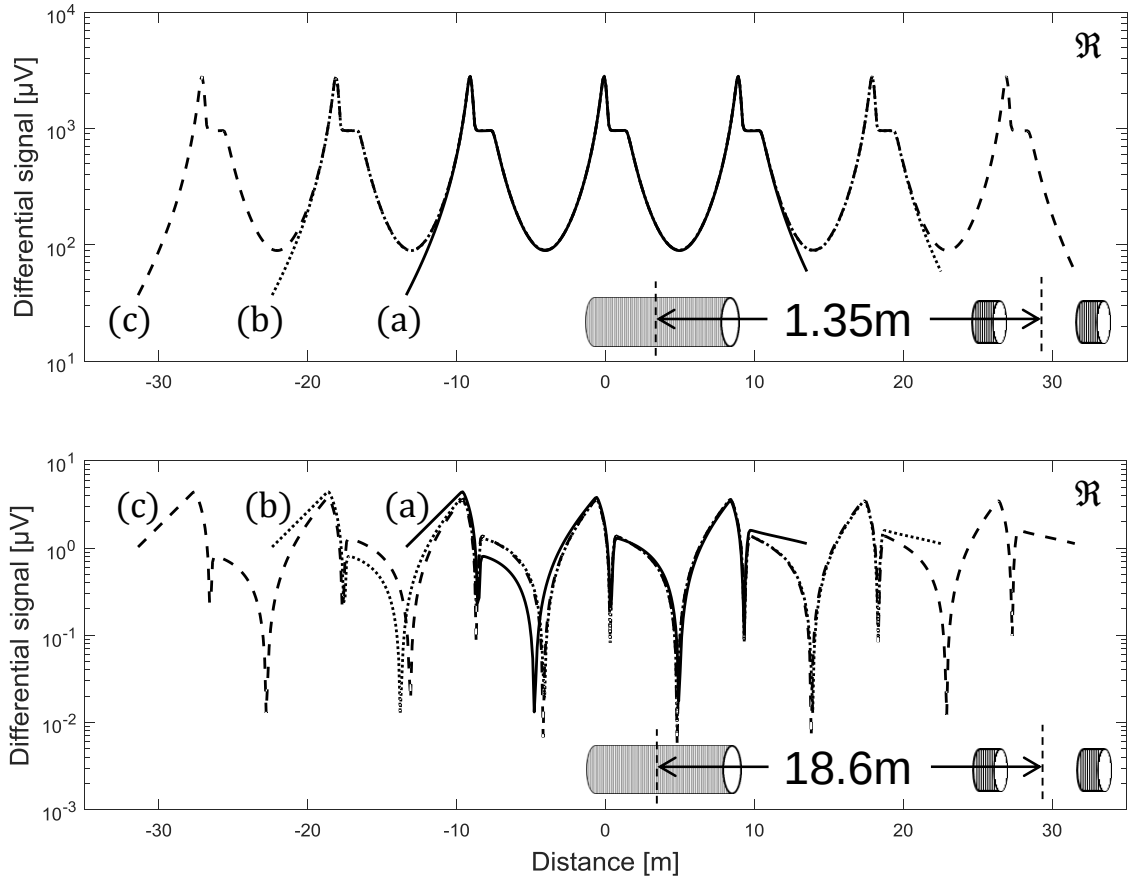

Figure 4.25: The effect of neighbors on the differential signals recorded in short (upper) and long (lower) coil spacings: fractures are shown in Fig. 4.24; plots show differential signals for one (a), two (b) and three (c) neighbors on both sides of the middle fracture.

In the short spacing receiver, we do not see any significant effect of the neighboring fractures. In the long spacing receiver, however, the two closest neighbors are interfering with the signal of interest. The cases with two and three neighbors give almost the same signals around the fracture of interest (with zero index number). Hence, in the next section, we include the effect of only the closest two neighboring fractures in the multi-fracture inversion to minimize the computation time.

4.3.2.2. Multi-Fracture Inversion

The technique used for the inversion is to first invert the data for each fracture assuming that it has no neighbors. Then, we use the best inverted parameters as an initial guess for the inversion with multiple fractures. In this second iterative step, we include the two closest neighbor fractures on both sides of the fracture of interest (maximum of five total fractures in each forward model). To demonstrate this procedure we use two true models shown in Fig. 4.26.

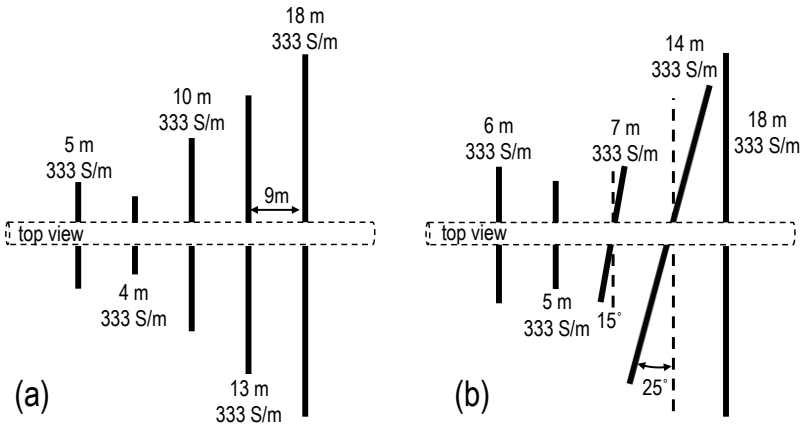

Figure 4.26: Two "true" fracture models used for the multi-fracture inversion analysis: (a) all fractures are orthogonal and (b) third and fourth fractures are tilted.

The differential signals for case (a) are shown in Fig. 4.27. It is not easy to distinguish the distribution of fracture sizes by visual inspection. First, for each fracture, we invert the signals in the interval of (-1, 1) m. Second, the results obtained in the previous step are used as initial guesses for the multi-fracture inversion. We are using two model parameters, fracture conductivity and size.

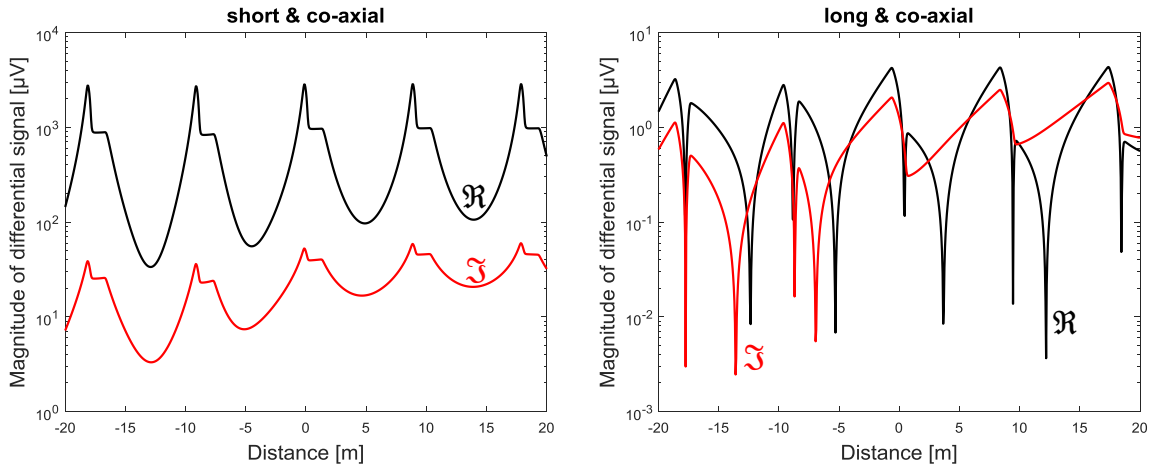

Figure 4.27: Differential signals for the case shown in Fig. 4.26(a): real (black) and imaginary (red) components are shown for co-axial configurations for short (left) and long (right) coil spacings.

After the single fracture inversion, we get the following error vs. iteration for each fracture in case (a). The increase in the error level, as we go from fracture number 1 to 5, can be related to the effect of neighboring fractures.

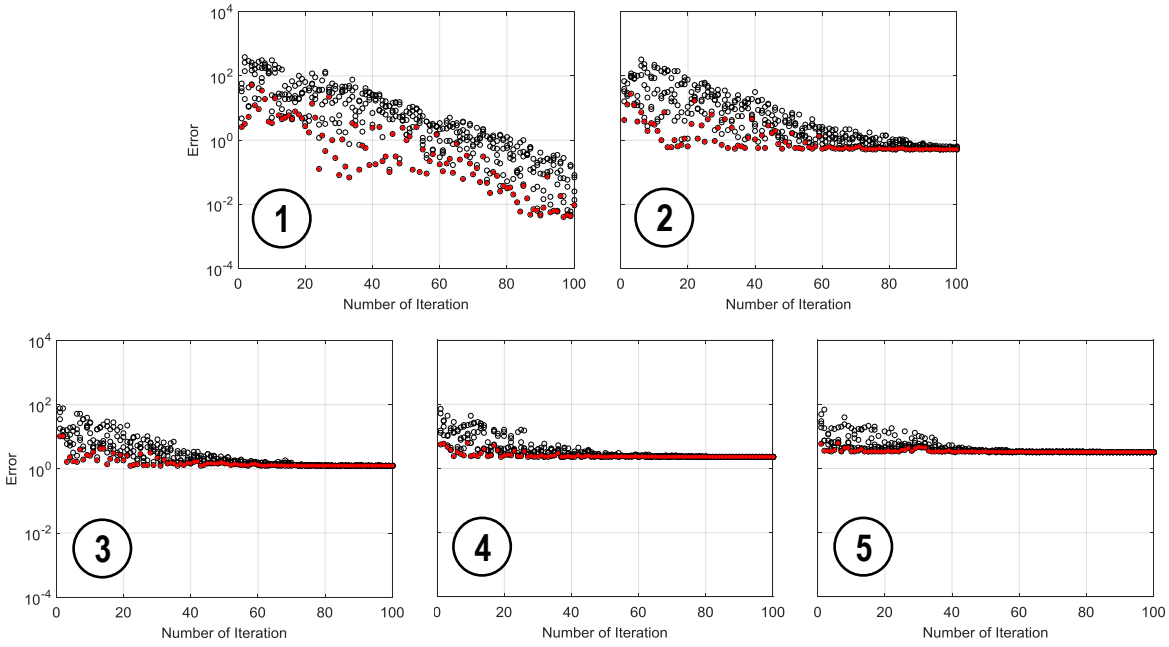

Figure 4.28: Single-fracture inversion results for the case shown in Fig. 4.26(a). A change in the error with the number of iterations is shown for each fracture numbered from left to right: open circles show errors for all models and red filled circles show a model with the minimum error in the given iteration.

The best results for the single fracture inversion (the models with the lowest error) are shown in Fig. 4.30 – middle figure. The evolution of errors after two iterations in the multi-fracture inversion is shown in Fig. 4.29. As can be seen in the plots, final errors are less than the errors in the first step. The final output is shown in Fig. 4.30 – right plot. The calculated fracture parameters are in a sufficiently good agreement with the true parameters.

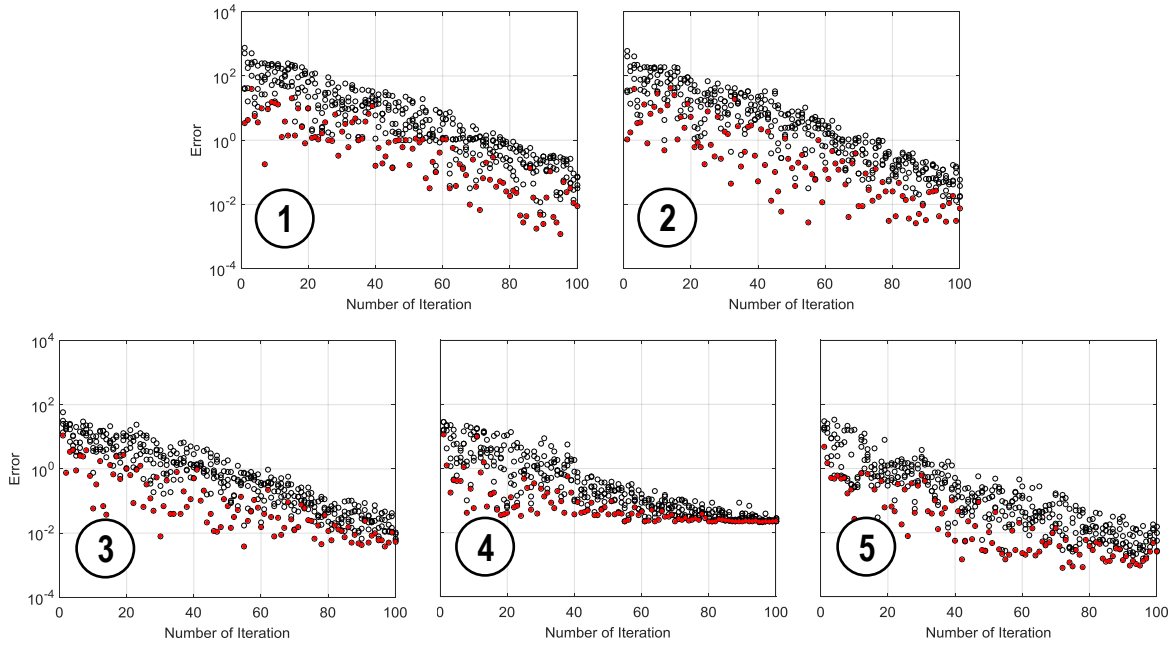

Figure 4.29: Multi-fracture inversion results after two iterations for the case shown in Fig. 4.26(a). A change in the error with the number of iterations is shown for each fracture numbered from left to right: open circles show errors for all models and red filled circles show a model with the minimum error in the given iteration.

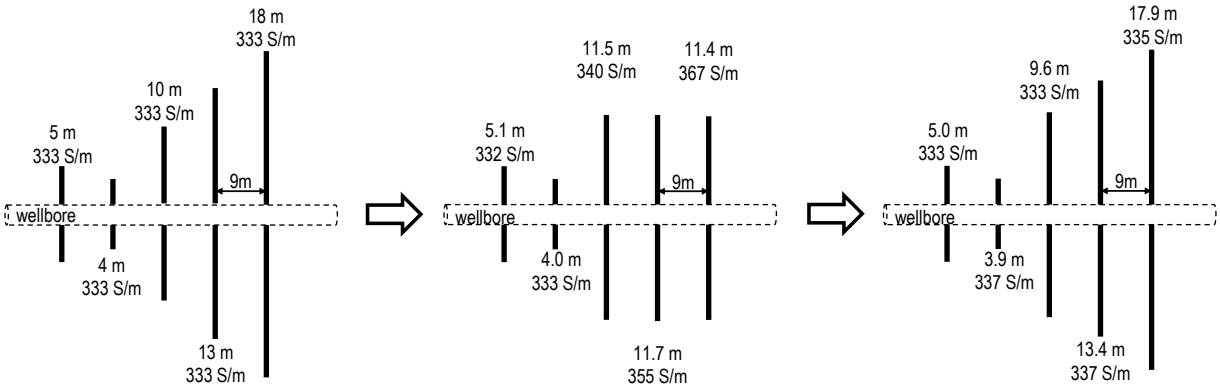

Figure 4.30: Multi-fracture inversion analysis for the model shown in Fig. 4.26(a): left figure shows the true model; middle and right figures show the best result after single- and multi-fracture inversions, respectively.

The differential signals for case (b) are shown in Fig. 4.31. Again, it is not easy to distinguish the distribution of fracture sizes by visual inspection. Based on two peaks in the signal observed in the cross-polarized configuration of short coil spacing (lower-left plot), we use three model parameters (conductivity, size and dip-angle) for the third and fourth fractures and two parameters (conductivity and size) for the rest. We apply the same inversion strategy as in the previous case.

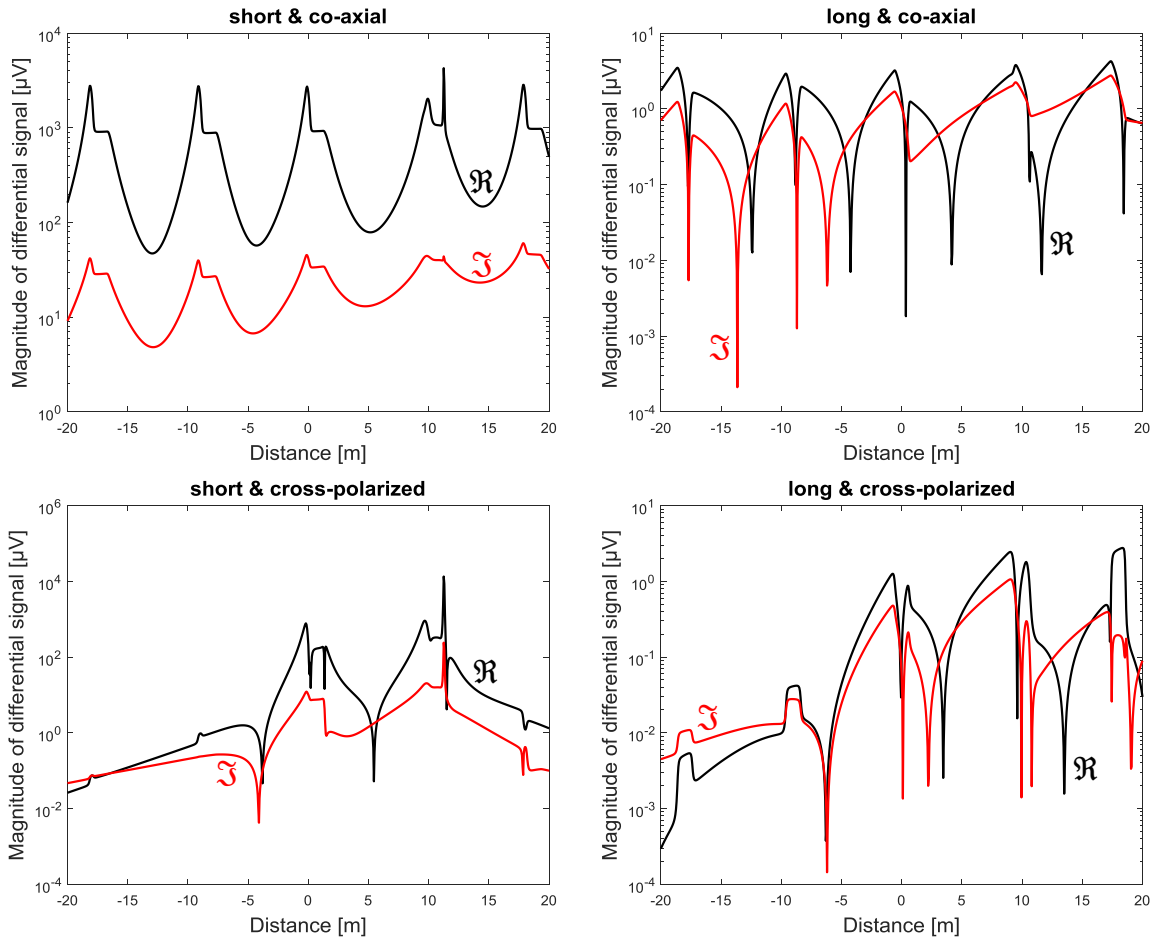

Figure 4.31: Differential signals for the case shown in Fig. 4.26(b): real (black) and imaginary (red) components are shown for co-axial (upper row) and cross-polarized (lower row) configurations for short (left column) and long (right column) coil spacings.

After the single fracture inversion, we get the following error vs. iteration for each fracture in case (b). The high levels of error for all cases can be attributed to the effect of neighboring fractures.

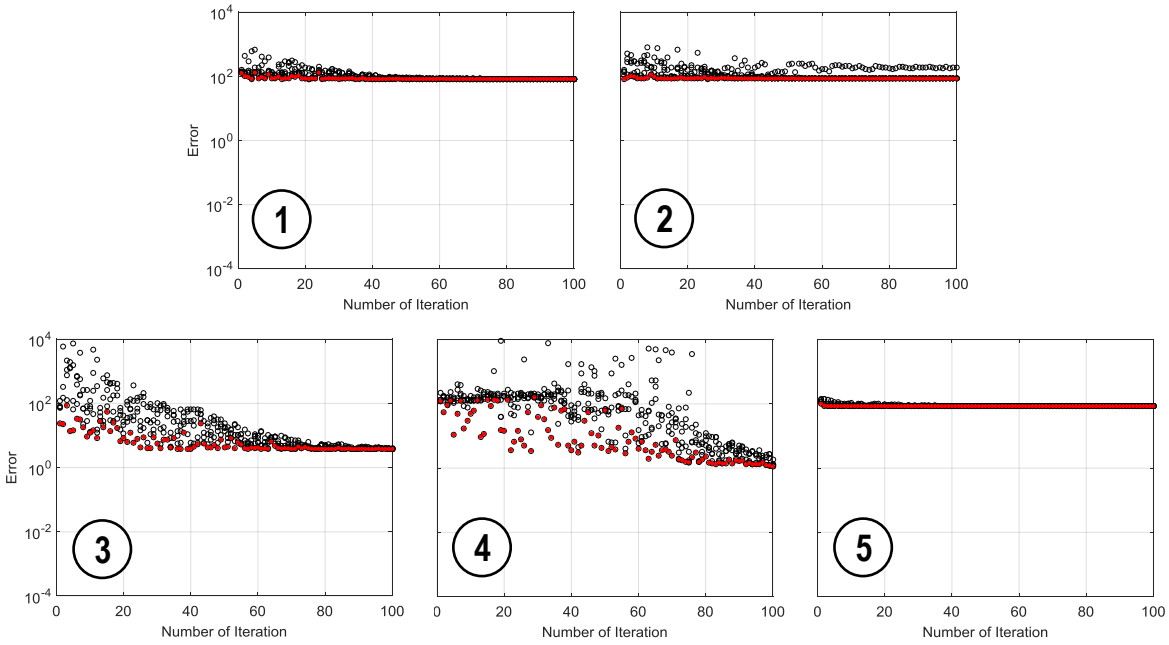

Figure 4.32: Single-fracture inversion results for the case shown in Fig. 4.26(b). A change in the error with the number of iterations is shown for each fracture numbered from left to right: open circles show errors for all models and red filled circles show a model with the minimum error in the given iteration.

The best results for the single fracture inversion (the models with the lowest error) are shown in Fig. 4.34 – middle figure. The evolution of errors after two iterations in the multi-fracture inversion is shown in Fig. 4.33. As can be seen in the plots, final errors are much less than the error of the first step. The final output is shown in Fig. 4.34 – right plot. The calculated fracture parameters are in a sufficiently good agreement with the true parameters.

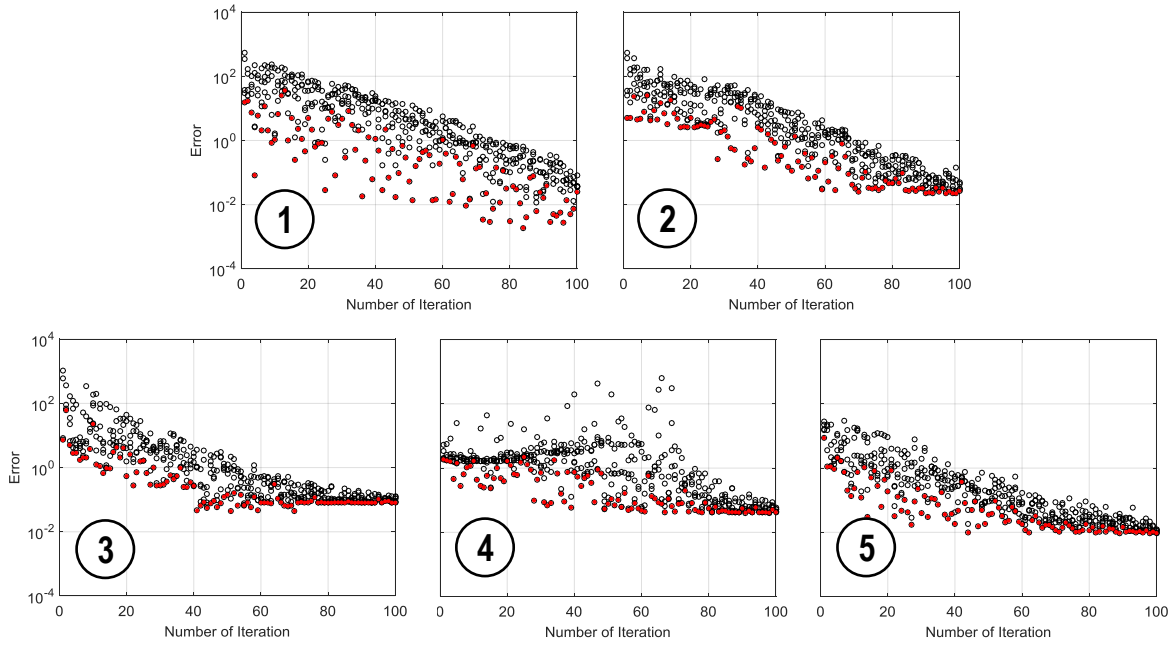

Figure 4.33: Multi-fracture inversion results after two iterations for the case shown in Fig. 4.26(b). A change in the error with the number of iterations is shown for each fracture numbered from left to right: open circles show errors for all models and red filled circles show a model with the minimum error in the given iteration.

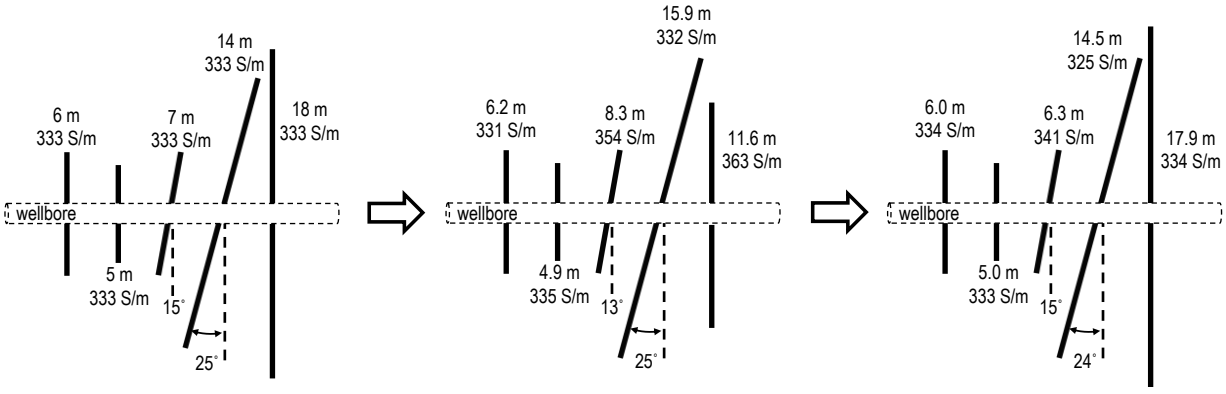

Figure 4.34: Multi-fracture inversion analysis for the model shown in Fig. 4.26(b): left figure shows the true model; middle and right figures show the best result after single- and multi-fracture inversions, respectively.

4.4. CONCLUSIONS

In this chapter, we developed a hybrid stochastic inversion algorithm to process tri-axial induction data to estimate the geometry and conductivity of hydraulic fractures. It is shown that this inversion analysis can successfully provide good estimates of fracture length, conductivity and dip-angle. The approximation based linear regression is also shown to be a very efficient inversion technique for single orthogonal fractures. When neighboring fractures are considered in the inversion, the hybrid inversion model provides excellent results. In all cases, good agreement is obtained between the true and estimated fracture parameters suggesting that a tri-axial EM tool has excellent potential to map the proppant distribution in hydraulic fractures. The following conclusions are obtained from this study:

- By using a mono-axial transmitter coil and tri-axial receiver coils, it is possible to recover the effective properties of hydraulic fractures; two coil configurations (co-axial and cross-polarized) and two coil spacings (short and long) are essential to provide the complete description of fracture geometries and conductivities.
- For fractures that are assumed to be circular, parameters such as fracture conductivity and radius were shown to be recovered very accurately. For fractures that are assumed to be elliptical, we recover the effective radius for a circle which has the same area as the ellipse. When the proppant concentration varies radially in a fracture (linearly decreasing conductivities towards the fracture tip), the inverted conductivity value is approximately equal to the average conductivity of the fracture. In all these cases, the calculated dip-angle is always close to the true value.
- For heterogeneous conductivity rock, an accurate estimate of fracture parameters is obtained only after the subtraction of the differential signals with and without a hydraulic fracture. The differential signals without a fracture can be large enough to

affect the inversion accuracy. This highlights the importance of logging the well before and after fracturing operations.

- For a tool spacing of 18 m, differential signals for the fracture of interest are affected by two neighboring fractures on each side when 9 m spacing is used for the distance between fractures. To invert the results for multiple fractures in a time efficient manner, five fractures should be included in each forward model run. This approach is shown to provide a very accurate estimation of fracture parameters in the given stage.

Chapter 5: DESIGN SPECIFICATIONS AND SIMULATIONS FOR A FIELD DEPLOYABLE TOOL

The final chapter summarizes a suggested design of the tool and explores its potential based on the numerical models presented in the previous chapters. The results presented here provide quantitative insight into the differential signals by evaluating the tool properties and proppant characteristics. To minimize power requirements and to investigate large fracture surface areas, we studied the effect of tool operation frequencies including multi-frequency measurements. In addition, we studied the effect of tool coil spacing to improve the efficiency of primary field cancellation and suggested a trend-line for selecting the coil separation distances. Later, we present numerical results for an inter-well deployment of the tool where a treatment well is monitored by an offset well. We also showed how proppant settlement can be monitored and how the enhanced electrical permittivity and magnetic permeability of the proppants can improve the differential signals. Lastly, the effect of electrical anisotropy of shale rocks in the measurements is studied. At the end of the chapter, we suggest future possibilities to improve the tool capabilities.

5.1. LITERATURE REVIEW

In this review section, we provide information on how this tool can be deployed in the field by providing a summary of engineering reports obtained from E-Spectrum Technologies Inc. (2016). Fig. 5.1 shows the main two components needed for field deployment: a surface system and a modular downhole tool. The surface system includes computer hardware that allows the data to be downloaded and analyzed. For EM signals, deeper penetration into the rock is generally obtained by using lower frequencies. In practice, however, lower frequencies require higher power which necessitates a surface

power supply. Therefore, the surface system also consists of a power source that delivers currents to the downhole tool. Lastly, considering the depth of reservoirs, it is anticipated that the power loss will be minimized if DC signals are delivered to the downhole tool and then converted to AC.

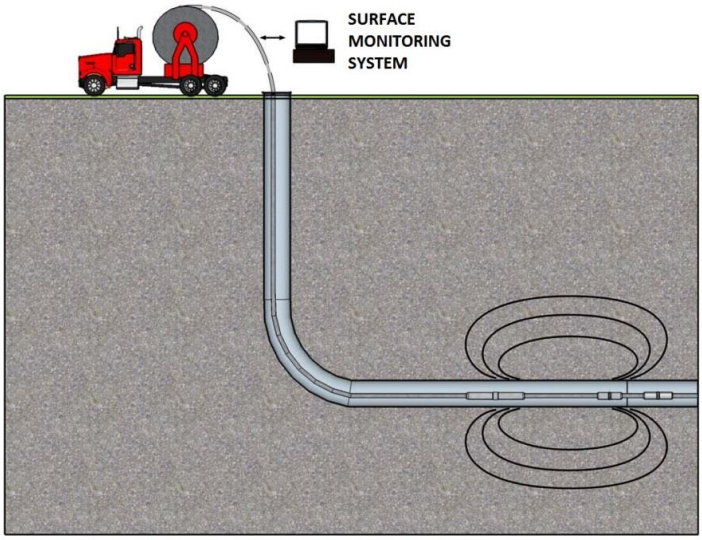

Figure 5.1: Low frequency electromagnetic induction tool consisting of a surface system and a modular downhole tool.

As shown in Fig. 5.2, in the current suggested deployment, the power supply is located on the surface, and a wireline cable is used to communicate with the downhole tool. In the rest of this section, we focus on the design specifications of the downhole tool that is proposed to be built.

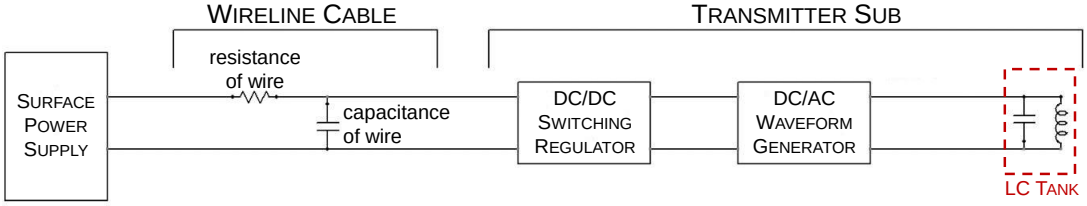

Figure 5.2: Transmitter sub power delivery system.

The modular downhole tool is designed to be deployed as a bottom hole assembly that consists of a transmitter control and coil sub, a receiver sub and a wired space bar. The transmitter control sub, which could be composed of a metallic section (the effect of this metallic section on the detected differential signals has not been numerically studied), includes the necessary electronics and hardware to communicate with the surface and the other modules of the downhole tool. It is powered from the surface and provides AC signals to the transmitter coil sub.

The transmitter coil sub is a tool section with a non-metallic housing which seals an LC tank shown with a dashed red box in Fig. 5.2. The LC tank is the most important component of the tool which acts as an energy storage device, and it consists of induction coils and capacitors. The tank stores energy in the magnetic field of induction coils and the electric field of capacitors and thus minimizes power demand. A detailed physics of the tank is presented in Section 5.1.2.

The transmitter sub is connected to three receiver subs (short, intermediate and long spacing module subs) which are non-metallic tool sections sealing receiver coils and electronics. They contain a replaceable bucking/receiver coil pair, and the data is stored in the receiver sub's logging memory which can be downloaded after tripping out and disassembling the tool. Each sub also has an Orientation Module (OM) which monitors the misalignment of the bucking/receiver coil pair with respect to transmitting coils. The module contains a tri-axial magnetometer and accelerometer providing information on the coil orientation with respect to the earth's magnetic and gravitational fields. It enables the correction of misalignment errors while the data is used in the inversion analyses.

The wired spacer bars are used to obtain the required spacing between transmitting and receiving coils while electrically and mechanically connecting the various modules. Lastly, a gamma ray attachment can be added to the tip of the downhole

tool to determine the tool's location. This enables an accurate subtraction of the measured signals before and after fracturing.

The maximum diameter of the tool must be less than 10 cm (4 inches), and the entire assembled tool is estimated to be about 23 m (76 ft.) long. The non-metallic sections of the downhole tool (transmitter coil sub, receiver subs, and spacer rods) can be made of fiberglass or plastic.

5.1.1. Primary Field Cancellation

In this dissertation, we have focused on single frequency analyses which allow us to use the frequency domain in all the experimental and computational set-ups. As already mentioned in Section 1.1, in the frequency domain, the primary fields need to be canceled in co-axial and co-planar configurations (the primary field in cross-polarized configuration is theoretically zero) to improve the tool's sensitivity to small variations in the total magnetic field. The cancellation technique we have used is detailed both in Chapter 1 and 3. Another approach was implemented in Yu et al. (2016) where a transmitter coil is utilized as the bucking unit to cancel direct coil coupling in a small area near the receiving coil without affecting the primary field at other locations. This bucking coil is in a concentric arrangement with the receiver coil and minimizes incident field such that the total magnetic flux density at receiver locations can be approximated to the scattered field. They suggest this approach to have the capabilities of performing in situ bucking adjustments which can further increase the sensitivity of the tool in the downhole measurements (Liu et al., 2015).

The implementation of the same electromagnetic induction concept in the time domain eliminates the need to cancel the primary field where the responses are measured in the absence of it. Measurements in the time domain, however, are more susceptible to

noise which can easily be filtered out in the frequency domain. If wide band analyses are required, the implementation of time domain methods will be more efficient because the same analyses in the frequency domain are overwhelming requiring many separate measurements.

5.1.2. LC Tank

The EM-based approach we are using for the hydraulic fracture monitoring supports many different types of waveforms: Gaussian, sinusoidal, square, etc. (Palisch et al., 2016). In this dissertation, we have considered a signal generator which pulses sinusoidal waves to the LC tank (Fig. 5.3) which is one of the main components of the tool. The tank circuit, which consists of transmitting coils and capacitors, is an energy storage device which stores energy in the magnetic field of coils and the electric field of capacitors. During each cycle, this field energy is circulated between these two components. In an ideal case, when the DC resistance of its components is negligible, no energy is lost per cycle, so no further energy needs to be supplied. In a real application, however, the tank circuit will lose energy in every cycle due to DC resistance, and this loss must be compensated for by the AC voltage source. The loss can be minimized if the tank is operated at a resonant frequency defined as:

$$\omega = \frac{1}{\sqrt{LC}} \tag{5.1}$$

where ω is the angular frequency, L is the inductance and C is the capacitance of the tank. It is possible to adjust the capacitance (number of capacitors in parallel, p) to maintain a required operation frequency for a given inductor (Fig. 5.3). In space limited tools, however, the addition of more capacitors is not always an easy task. The additional practical challenge is the temperature constraint of the capacitors.

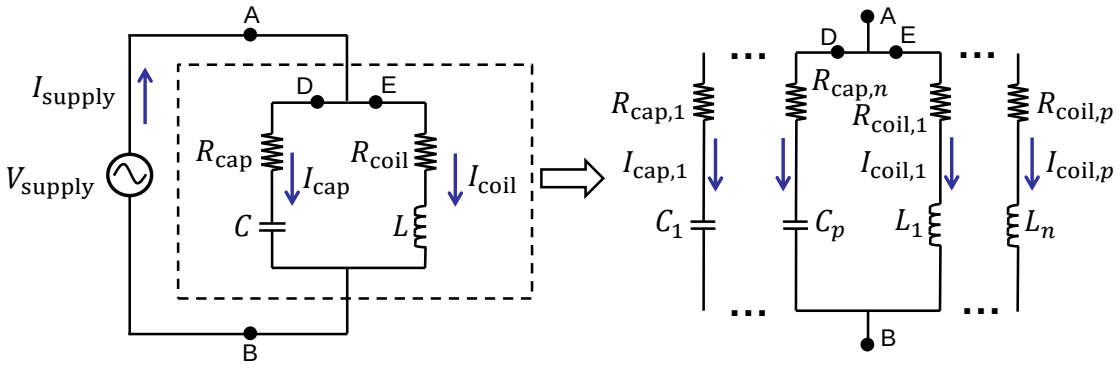

Figure 5.3: LC transmitter tank diagram.

For the induction coils used in the tank, the quality factor (Q) is an important design parameter to determine the efficiency of a coil's power storage. It is defined by the ratio of the inductive reactance (X) and the DC resistance (R) as shown below:

$$Q_{\text{coil}} = \frac{X_{\text{coil}}}{R_{\text{coil}}} = \frac{2\pi f L}{R_{\text{coil}}} \tag{5.2}$$

As is the case for dipole moment, the larger the value of quality factor, the better the design. It is possible to connect several inductor coils in parallel to decrease the total resistivity of a coil and to produce higher quality factors. The number of inductor coils in parallel (n), however, decreases the total inductance (L):

$$L < \frac{L_i}{n} \tag{5.3}$$

where inductance on each coil is calculated as:

$$L_i = \frac{\mu_{\text{core}} A_{\text{coil}} N_{\text{coil}}^2}{nh} \tag{5.4}$$

This is due to mutual inductance. The lower inductivity not only gives a lower quality factor but it also requires a higher capacitance for the given resonant frequency (Eq. 5.1). As previously mentioned, this is a mechanical challenge for a tool development.

In summary, for a low frequency electromagnetic induction tool, coils can be designed with a thicker gauge wire with fewer turns to reduce the losses and to lower the driving source power. Another important design consideration for this application is the use of a ferrite core which acts as a magnetic field multiplier. We get more benefit from a ferrite core as the length to diameter ratio of the coil increases, and this ratio is very small for coils oriented orthogonal to the wellbore. Therefore, a coil core oriented in the wellbore direction (z-oriented transmitter coil) will produce the strongest magnetic field.

5.2. TOOL SPECIFICATIONS

In this application, scattered signal levels are proportional to the frequency and inversely proportional to the distance between the coils. As we decrease the operation frequency, the signals get too weak to be detected (in the frequency range of interest signal levels decrease $\sim\omega^2$ as the frequency decreases). Hydraulic fractures, however, can be large and penetrate deep into the reservoir requiring large investigation areas which need lower operating frequencies and larger tool spacing. In this section, we provide optimum tool spacing maps to maximize received signals and to evaluate the bucking efficiency. Then, the investigation area of the tool is demonstrated by using the optimized spacing and frequency. The same analysis can be carried out for other frequencies and spacings with the numerical forward and inversion models provided in the Appendix. In the last sub-section, we performed a numerical study to appraise the applicability of the inter-well tool deployment where a transmitter coil is logging a fracture in a treatment well and observations are made in an offset well.

5.2.1. Tool Spacing

From the previous chapter on inversion analyses, we know that the calculation of fracture parameters require responses both from relatively short and long coil spacings. Therefore, it is very important to have detectable differential signals in all spacings. The detectability of the signal depends on its absolute and relative values. In this sub-section, we evaluate the effect of tool aperture on the strength of signals of interest (presented in absolute and relative level). First, we look at the incident and scattered signals detected with one receiver coil at different background conductivities. Then, we compare the incident and scattered signals when the fracture size is changed. Finally, the same comparison is performed when we include the bucking-receiver coil into the system.

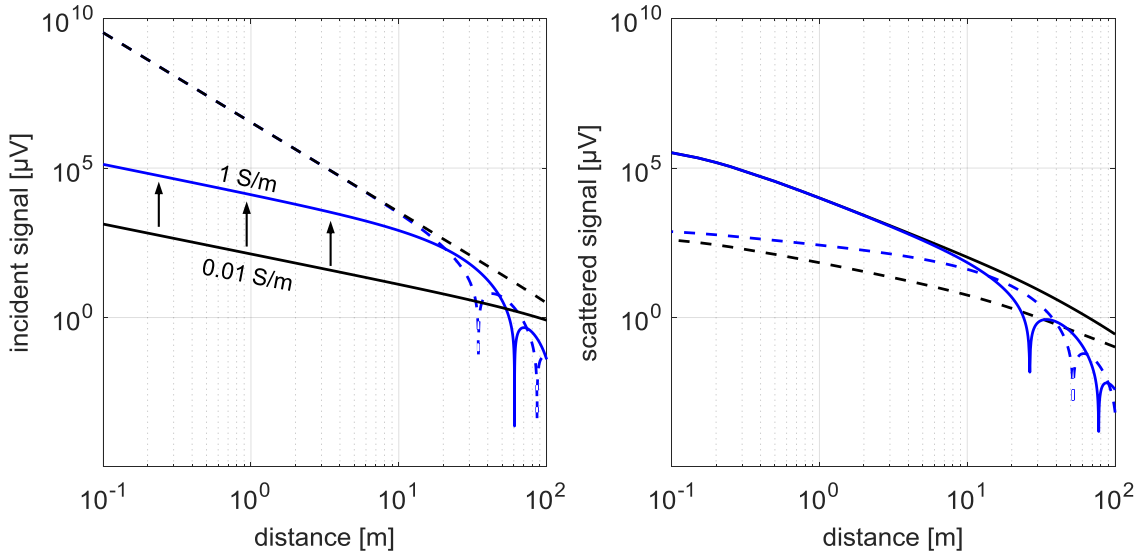

Figure 5.4: The effect of background conductivity on the incident (left) and scattered (right) signals: *x*-axis is the distance between transmitter and receiver coil; solid and dashed lines show real and imaginary components, respectively; black and blue lines are for a background formation conductivity of 0.01 S/m and 1 S/m, respectively. The tool is operated at 1 kHz frequency and 1500 $A \cdot m^2$ transmitting moment; the cross-sectional area of the receiver coil is 30 mm^2 with 600 turns. For the scattered field calculation, fracture is assumed to be a disc with 30 m radius, 333 S/m conductivity and 5 mm thickness.

Fig. 5.4 shows the change of incident signals with the change of background conductivity and transmitter-receiver spacing. The interval selected for the formation conductivity covers the minimum and maximum electrical conductivities of shale (Adisoemarta, 1999). For the scattered signals, the receiver is positioned at the fracture location, and we adjust the distance between the transmitter and the receiver coils. Obviously, as the distance between coils increases both incident and scattered signals weaken. An increase in the background conductivity of the formation, however, increases the real component of incident signals and the imaginary component of scattered signals keeping the other components the same for most of the transmitter-receiver spacing. Note

that for a majority of the region that covers the nominal tool spacings, imaginary signals are stronger than the real signals for incident fields and vice versa for scattered fields.

Fig. 5.5 shows incident and scattered signals for fractures with a radius of 1 m and 20 m, and the background (rock) formation conductivity is 0.333 S/m. As already noted in Fig. 5.4, there is a phase difference between the dominant components of incident and scattered signals, however, in all cases, the real component of incident signals is significantly stronger compared to that of scattered signals. This suggests the importance of the bucking coil for both short and long coil spacings. For the short spacing receiver, even signal decomposition will improve the quality of detection and adding the bucking coil will improve it further. For the long spacing receiver, however, the implementation of the bucking coil is more vital. Further plots are proposed for the optimum spacing between the receiver and bucking coil.

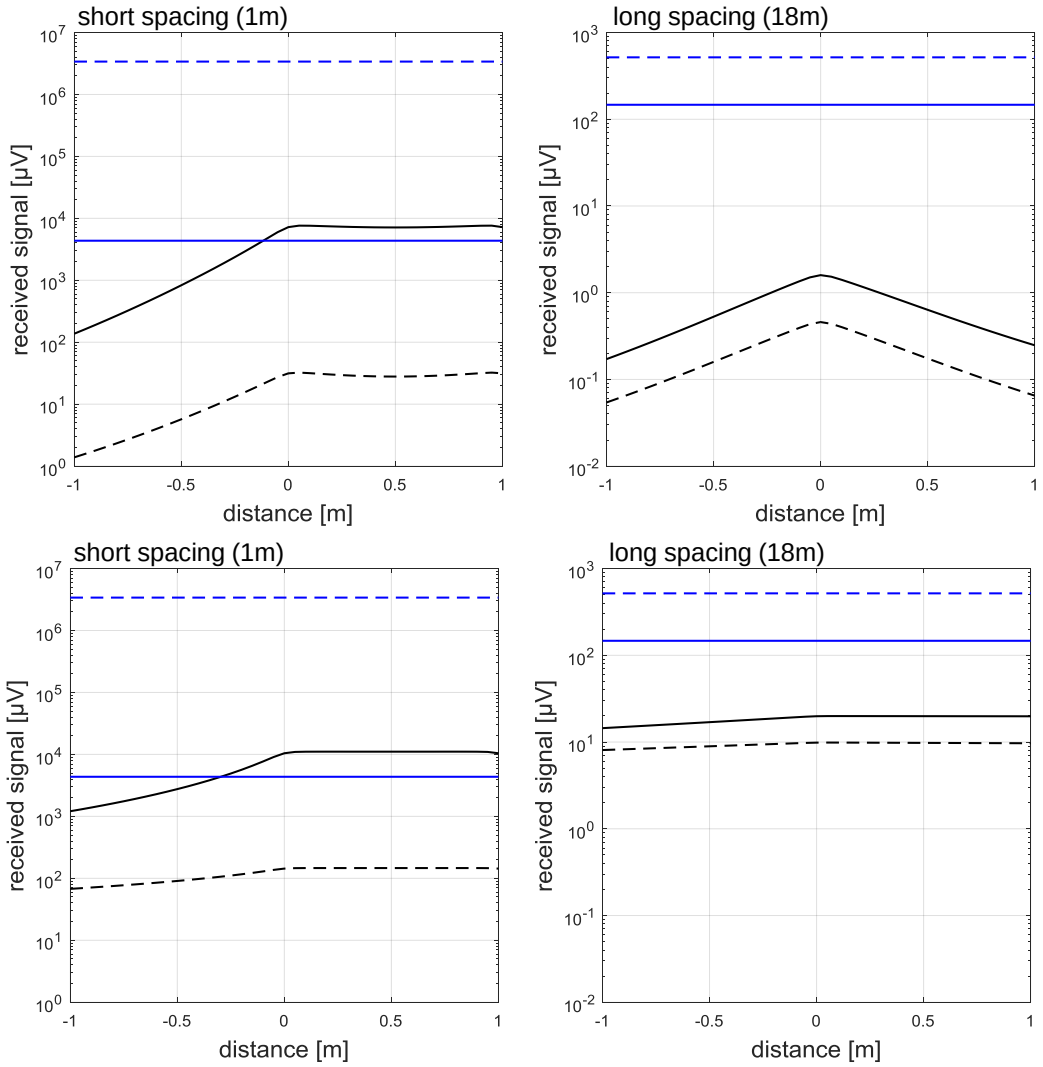

Figure 5.5: Incident (blue) and scattered (black) signals for short (left column) and long (right column) coil spacings: real (solid lines) and imaginary (dashed lines) components of signals are shown for the background formation with 0.333 S/m conductivity. The tool is operated at 1 kHz frequency and 1500 $A \cdot m^2$ transmitting moment; the cross-sectional area of the receiver coil is 30 mm^2 with 600 turns. For the scattered field calculation, a fracture is assumed to be a disc with 1 m (upper row) and 20 m (lower row) radius, 333 S/m conductivity and 5 mm thickness.

To find the optimum bucking and receiver coil distances for the long coil spacing, we plotted the absolute and relative signal levels for the 30 m radius fracture in Fig. 5.6.

The *y*-axis of the plots is the distance between the transmitter and the center of the receiver couples, and the relative signal is calculated by dividing the secondary signals by primary signals. Based on these absolute and relative signals, we suggest a trend-line (shown with a dashed line) to select the distance between coils. The dashed line is the region where differential signals are strong enough to be detected and their ratio to the primary signals is sufficiently large.

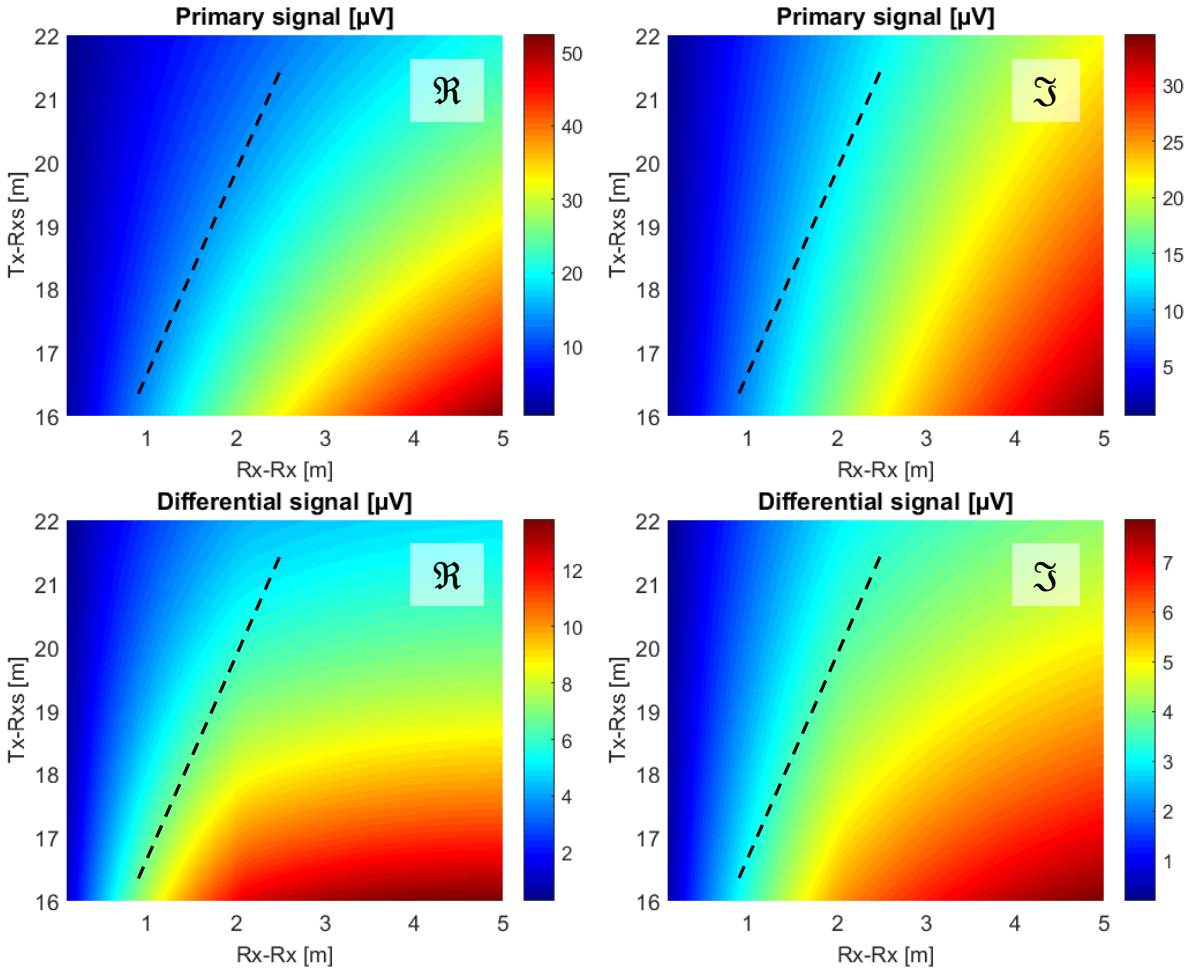

Figure 5.6.

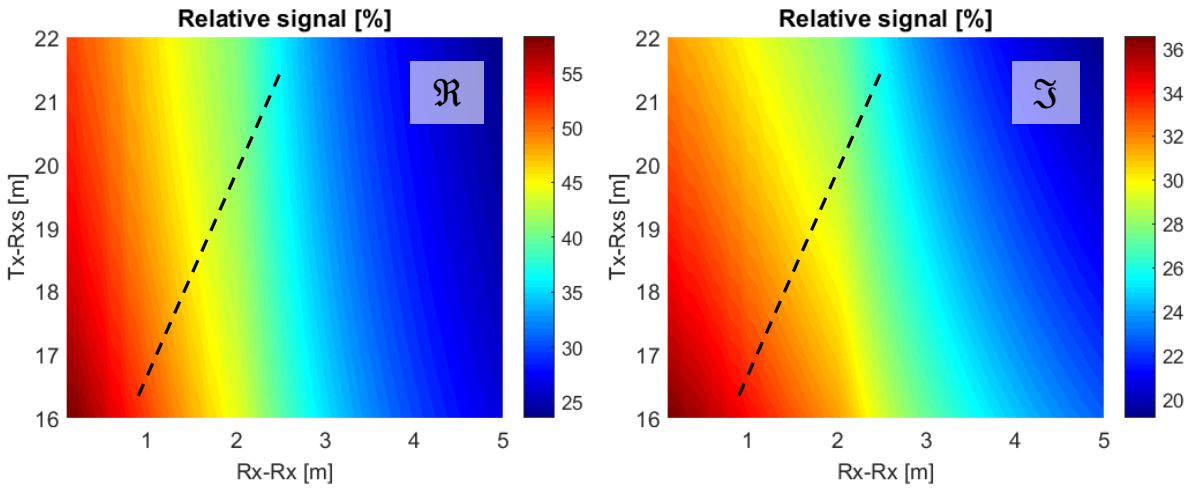

Figure 5.6: The primary (top row), differential (middle row) and relative (bottom row) signals for different transmitter-receiver and receiver-receiver spacings: real (left column) and imaginary (right column) components of signals are shown for the background formation with the conductivity of 0.333 S/m. For the differential and relative signal calculation, the fracture is a disc with 30 m outer radius, 10 cm inner radius, 333 S/m conductivity and 5 mm thickness.

5.2.2. Depth of Investigation

In this section, we estimate the investigation area of the tool by using the inversion algorithm developed in the previous chapter. We run multiple realizations by increasing the radius of fractures and calculating a variation in the inverted fracture parameters. Fig. 5.7 shows results for the tool with nominal spacings and properties. After running the forward model for the orthogonal and circular fractures with the node spacing factor of ten, we added one percent of random noise to the differential signals. A node spacing factor of four was used in the inversion analysis. There are at least five realizations for the given radius of a fracture and 300 of the most successful results are plotted in the figure. The measured variation is calculated by subtracting the true model parameter from the calculated value. In the runs, the fracture conductivity for the true model is 100 S/m.

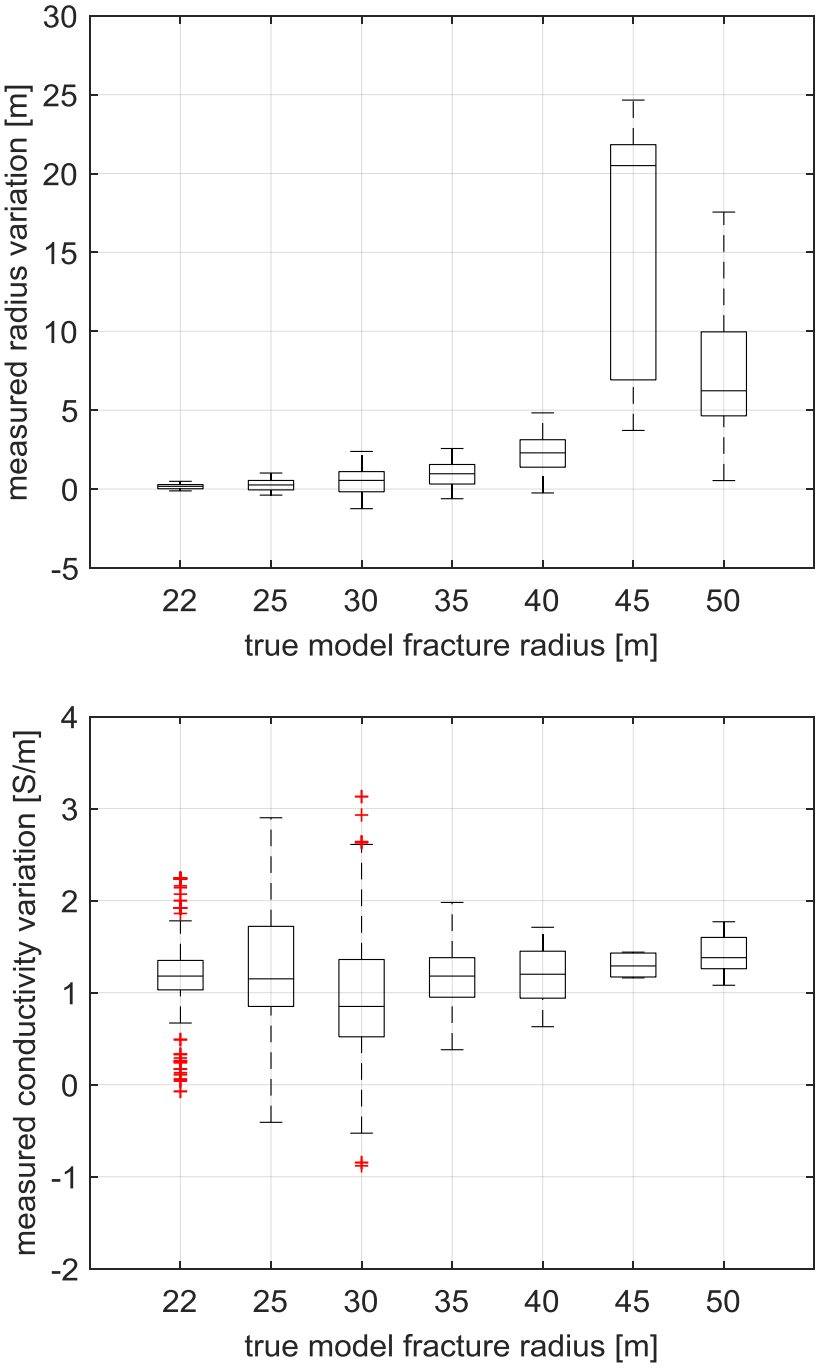

Figure 5.7: Box plots for the inverted vs. actual parameters: calculated variation of fracture radius (upper) and fracture conductivity (lower) vs. the fracture radius of the true model. The boxes include 300 of the lowest error results from 5 different realizations.

The results show that once the radius surpasses 40 m, the tool with the nominal spacing and properties loses resolution. The variation of fracture conductivity, however, is not increasing for this uniformly distributed conductivity case. To determine fracture sizes larger than 40 m we can use longer spacings for the tool but we need to make sure that signals are detectable. One way to increase these signal levels is to deploy a receiver coil with a higher magnetic dipole moment (not taking into account the noise level in the field). Another way is to use proppants with further enhanced electromagnetic properties (see Section 5.3.4).

5.2.3. Inter-well Testing

To diagnose larger fractures, another potential deployment of the tool is the inter-well monitoring of the treatment well. In this part, we numerically evaluate signal levels detected with receivers in an observation well while logging a treatment well with a transmitter coil. The fracture is an orthogonal circle with a radius of 30 m, conductivity of 333 S/m and thickness of 5 mm. The upper drawing of Fig. 5.8 shows the scheme used in the simulation, and in the lower graph, secondary (scattered) signals are plotted. Two separate lines are shown for the transmitter fracture distance: the lower line is the secondary signals when the transmitter coil is 30 m away from the fracture and the upper line shows signals when the transmitter coil is at the center of the fracture. The receiver is in the observation well where its *z*-coordinate is always the same as that of the fracture. The tool is operated at 1 kHz frequency and 1500 $\mathrm{A \cdot m^2}$ transmitting moment; the cross-sectional area of the receiver coil is 30 $\mathrm{mm^2}$ with 600 turns.

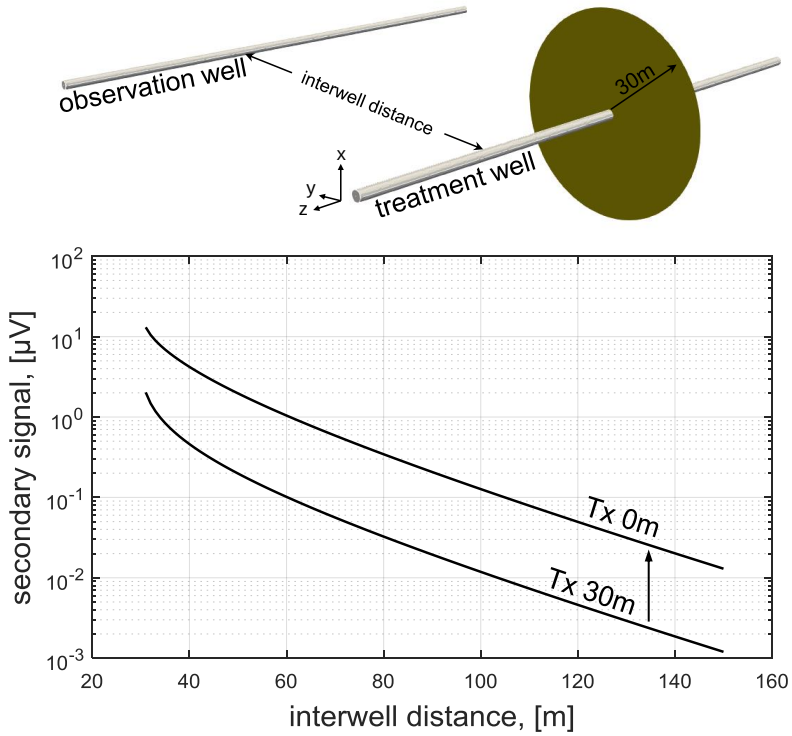

Figure 5.8: Inter-well hydraulic fracture monitoring: scattered signals are calculated for a receiver coil in the observation well and a transmitter coil in the treatment well (upper drawing). In the plot, upper and lower lines show signals when the transmitter coil is 0 m and 30 m away from the fracture, respectively. The fracture is a disc with an outer radius of 30 m, inner radius of 10 cm, conductivity of 333 S/m and thickness of 5 mm. The background formation (rock) conductivity is 0.333 S/m. The tool is operated at 1 kHz frequency and $1500\,\mathrm{A}\cdot\mathrm{m}^2$ transmitting moment; the cross-sectional area of the receiver coil is $30\ \mathrm{mm}^2$ with 600 turns.

As it can be seen in the plot (Fig. 5.8), for the transmitter coil at the center of the fracture (upper line), the scattered signals fall below 1 μV when the observation well is 60 m away from the treatment well. To detect weak signals is practically challenging and this limits the deployment of the tool for inter-well diagnosis.

5.2.4. Multi-Frequency Analysis

As shown in *Section 4.3.1.4*, operating the induction tool at a single frequency provides a single conductivity value for the model with radially decreasing conductivity. In this section, a sensitivity study is carried out to investigate if additional constraints on fracture geometry can be obtained with multi-frequency induction measurements. By using the integral equation solver a fracture with radially and linearly decreasing electrical conductivity is simulated at different frequencies, and results are compared to the signals at a nominal 1 kHz frequency. To obtain the relative signal, the differential signal at a given frequency is divided by that at 1 kHz. Fig. 5.9 shows real and imaginary components of these relative signals at short and long coil spacing.

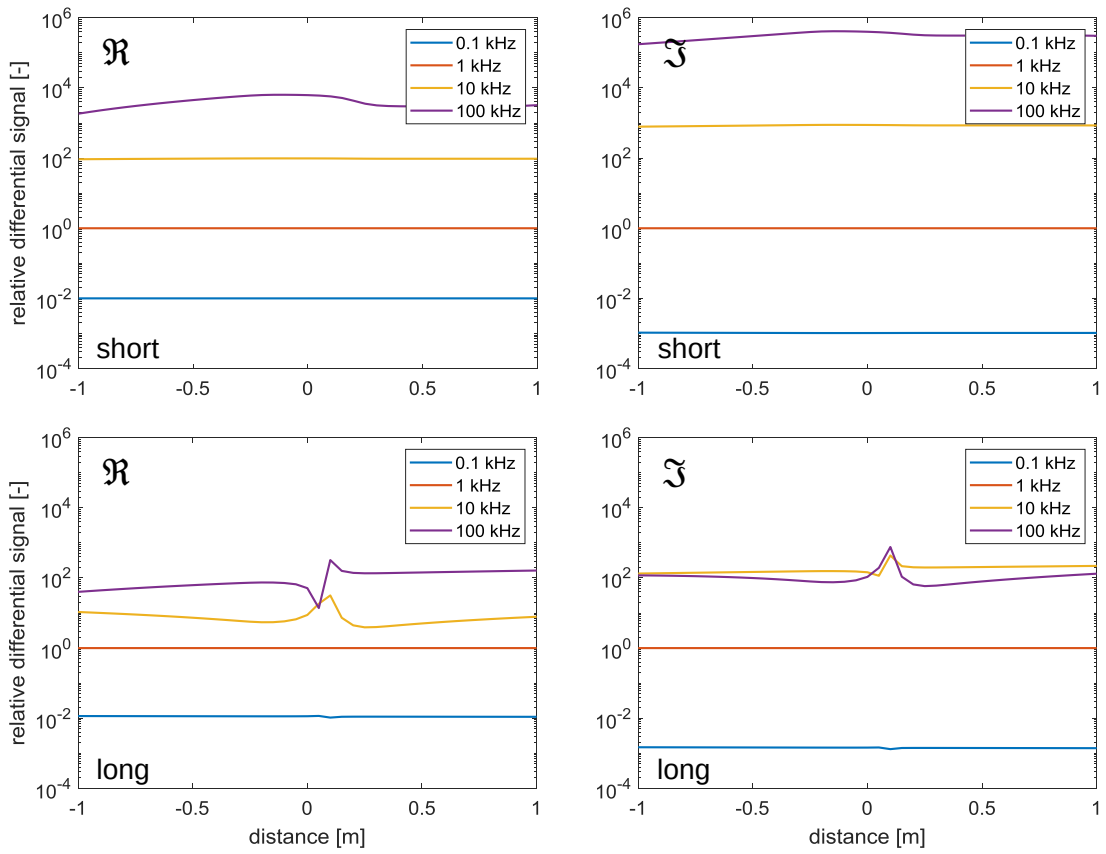

Figure 5.9: The relative differential signals (normalized with respect to signals at 1 kHz) at different operation frequencies: the fracture model is orthogonal circle with a radius of 10 m, and the conductivity at the wellbore is 333 S/m and 0 S/m at the fracture tip, decreasing linearly; real (left column) and imaginary (right column) differential signals are shown for co-axial coil configurations in short (upper row) and long (bottom row) coil spacing.

An increase in the operation frequency decreases the investigation area of the tool, therefore, the signals are not expected to linearly scale with an increase in the frequency. As shown in Fig. 5.9, indeed, the differential signals do not scale linearly at all frequencies. The signal at 100 kHz frequency for the short coil spacing and the signals at 10 and 100 kHz frequencies for the long coil spacing can provide additional information on conductivity distribution.

5.3. SIMULATING FIELD DEPLOYABLE TOOL

In this section, we numerically investigate the tool's potential to detect proppant settling. Later, a numerical study is carried out to see how proppants can be upgraded to scatter stronger signals.

5.3.1. Proppant Settlement

There has been a great deal of research conducted on the proppant transport in hydraulic fractures (Blyton et al. 2015). Investigating favorable conditions leading to efficient proppant delivery to induced fractures without letting them settle has been a long-standing challenge. Independent proppant monitoring techniques assist in these studies and improve operational efficiencies. Therefore, in this section, we evaluate the potential of the induction tool for settlement detection by changing the geometry of fractures, as shown in Fig. 5.10, and recording the variation in the differential signals. For all cases, we assume that the injected proppant volume is the same; as the area of fracture decreases, we linearly increase the conductivity. The surface area of fractures is 201 m^2, 162 m^2, 101 m^2 and 67 m^2, hence the conductivity is selected as 100 S/m, 124 S/m, 200 S/m and 300 S/m for the fractures from left to right (Fig. 5.10), and the thickness of fractures is 5 mm for all cases.

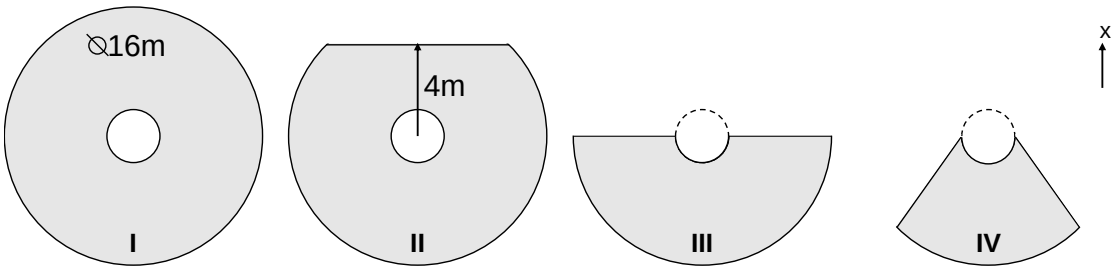

Figure 5.10: Fracture models used in the proppant settlement simulation: models are orthogonal to the wellbore, and the injected volume of proppant is constant.

Differential signals for the four different cases of fractures are plotted in Fig. 5.11. In the computation, the distances for the short spacing receivers are 0.8 m and 1.2 m, and 17.8 m and 18.2 m for the long spacing receivers. The operational frequency is 1 kHz, and transmitting magnetic dipole moment is 1500 A.m^2. The cross-sectional area of receiver coils is 30 cm^2 with 600 turns. The formation (rock) conductivity is 0.333 S/m.

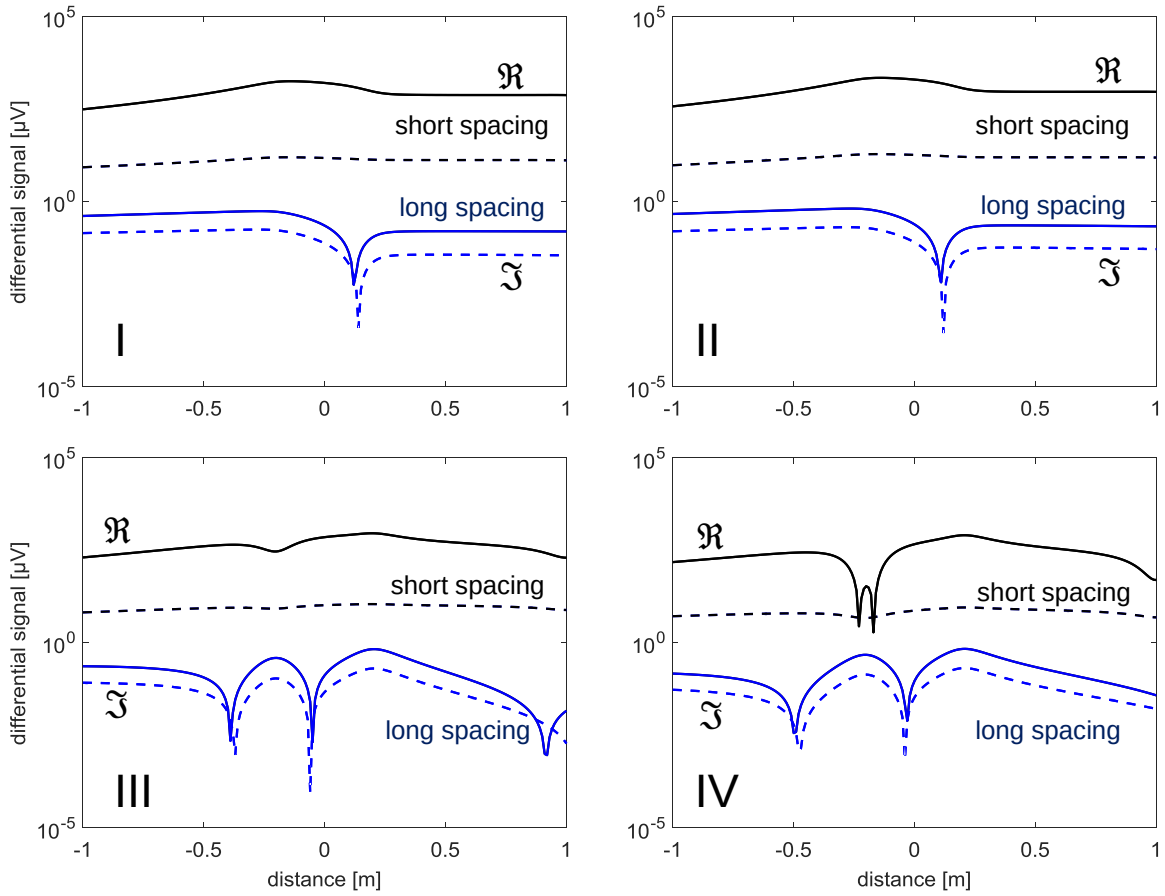

Figure 5.11: Monitoring proppant settling: fracture models shown in Fig. 5.10 are used to compute the real (solid line) and imaginary (dashed line) components of differential signals in short (black) and long (blue) coil spacings.

As the shape of fracture becomes more irregular, differential signals vary from that of the regular circle response. This proves that there is good potential for the tool to evaluate proppant settlement.

5.3.2. Enhanced Electrical Permittivity

Till now, all results are demonstrated for the electrical conductivity of proppants where both the relative permittivity and magnetic permeability are one. In this sub-section, we investigate how proppants with enhanced electrical permittivity affect the differential signals. In the next sub-section, the effect of enhanced magnetic permeability is studied.

To evaluate the effect of enhanced electrical permittivity, we need to implement the boundary condition shown in Eq. 2.13. In the equation, shunt admittance is due to two parallel sheets: a resistive sheet with the admittance σt and a pure reactive sheet (the right component of the summation). In Fig. 5.12, we plot those components over a wide frequency range. The fracture conductivity is 333 S/m and thickness is 5 mm. As can be seen from the plot, in the 1 Hz - 1 MHz range of frequency, the resistive sheet strongly dominates shunt admittance and consequently surface impedance. As the relative permittivity of proppants increases the signals of interest will not be affected.

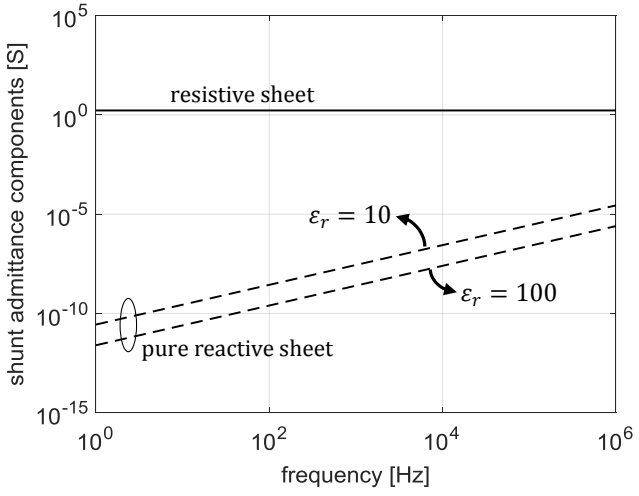

Figure 5.12: Dependence of shunt admittance (Eq. 2.13) on the resistive (solid line) and pure reactive (dashed lines) sheet.

5.3.3. Enhanced Magnetic Permeability

For evaluating the effect of enhanced relative magnetic permeability, we have used the axial hybrid method and the values are adjusted between 1, 5, 10, 20 and 50. In the simulation, the fracture has an outer radius of 8 m, inner radius of 10 cm, conductivity of 333 S/m and thickness of 5 mm, and the background formation (rock) conductivity is 0.333 S/m. The uniform section of meshing ranges from -1 to 1 m with the step sizes of 10 cm (Fig. 2.13). In the expanding mesh section, grid expansion ratio is 1.1, and the computation domain is truncated at 100 m on both edges. The operation frequency is 1 kHz, and the magnetic dipole moment of transmitter coil is 1500 $A.m^2$. The cross-sectional area of receiver coil is 30 cm^2, and the number of turns on the receiver coil is 600. The distance between the transmitter and the first and second receivers is 0.8 and 1.2 m, respectively. Fig. 5.13 shows real and imaginary components of differential signals for all relative permeabilities.

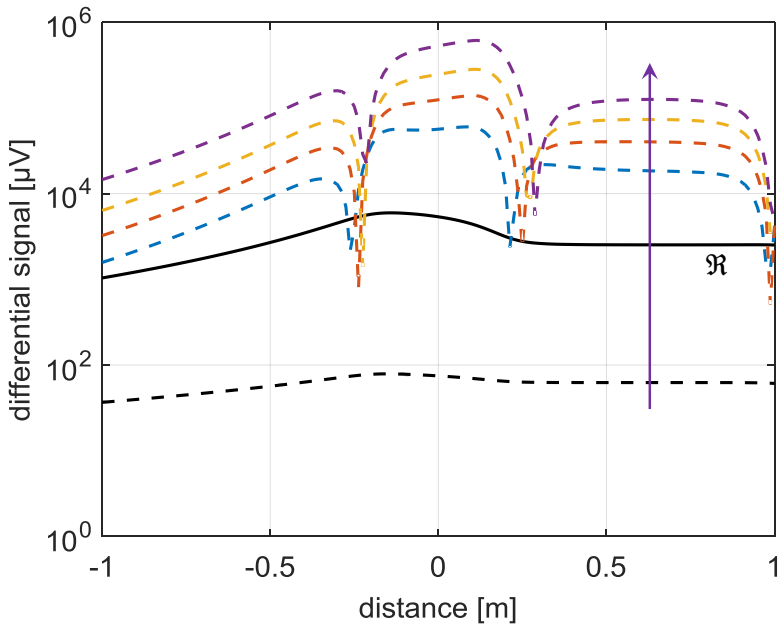

Figure 5.13: The effect of fracture relative magnetic permeability on the differential signals calculated with co-axial configuration of short coil spacing: relative magnetic permeability increases in the direction of arrow, and the values are selected as 1, 5, 10, 20 and 50; black solid line shows real component of signals for all simulated cases and dashed lines are imaginary components.

It can be seen from the plot that the real part of the differential signal does not change while increasing the relative permeability; however, imaginary components increase significantly. A 50 times increase in the relative permeability results in imaginary differential signals 100 times stronger than the real components.

5.3.4. Effect of Electrical Conductivity Anisotropy in Shale Rocks

In this sub-section, we investigate the possible effect of formation electrical conductivity anisotropy in induction tool measurements. If we assume that the formation conductivity is different in the transverse and wellbore directions (note that this might not be an accurate representation of the anisotropy for horizontal wellbores), the axial hybrid method can be used to simulate the scenario (Eq. 2.37 and 2.38). We use anisotropic

conductivities for the background formation in the forward model to obtain the "true model". The inversion model is run assuming isotropic conductivity, and the calculation is repeated twice for transverse and wellbore direction background conductivities. The results are shown in upper and lower rows of Fig. 5.14. The fracture is 10 m in radius and 333 S/m in conductivity. The transverse and horizontal conductivities are selected to be 0.5 and 0.25 S/m, respectively. The same meshing scheme shown in *Section 4.3.1.5* is used.

As shown in the box plots, the results are accurate for the run that uses the transverse background conductivity indicating that it has the dominant effect on the measured signals. The conclusion is the same when we repeat the forward and inversion runs with reversed transverse and horizontal background conductivities.

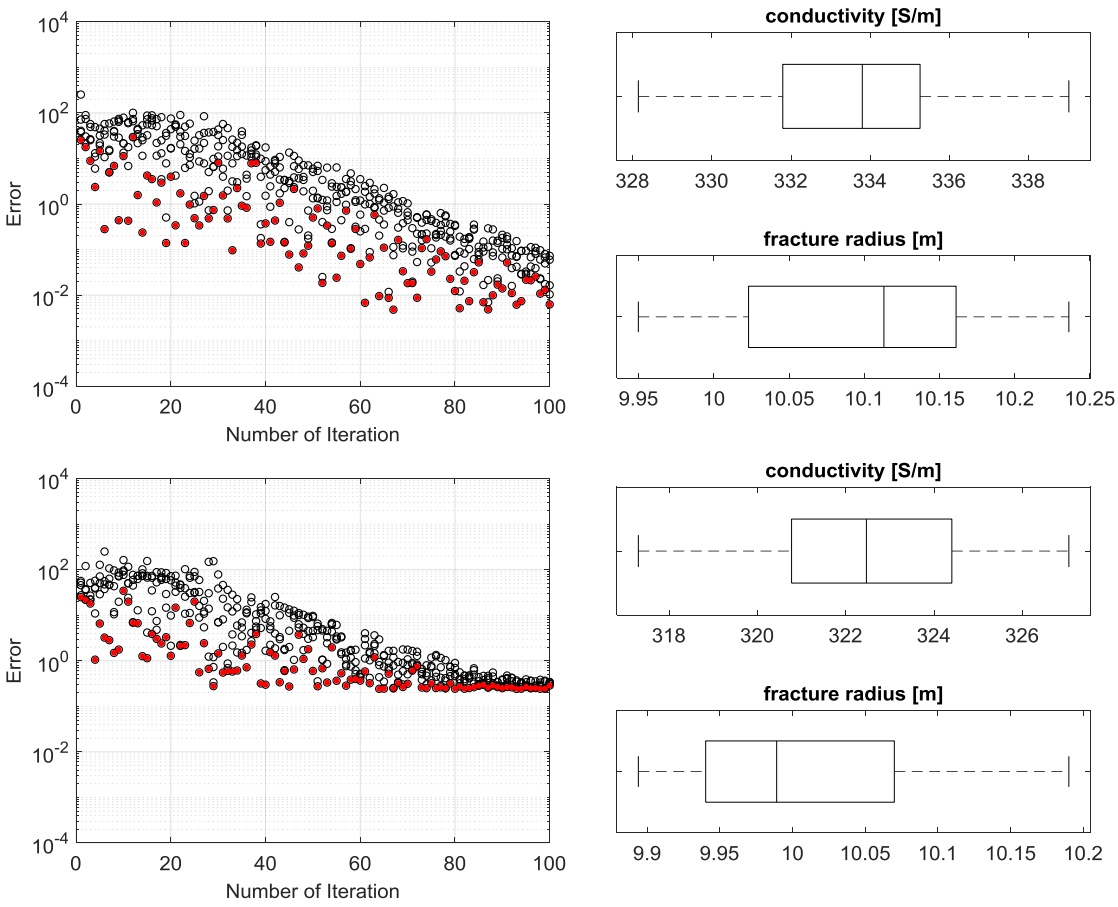

Figure 5.14: The effect of electrical conductivity anisotropy on the inversion of log data: the upper and lower rows show the inversion results when the transverse and vertical formation conductivities are selected in the inversion process, respectively.

5.4. CONCLUSIONS

In this chapter, first, we presented the current design of the induction tool. Then, we demonstrated the capabilities of the current tool with nominal spacing and properties. The signal levels for a range of shale rock electrical conductivities are presented and the improvement made with the bucking coil is evaluated to establish a trend-line to calculate the distance between the receiver and bucking coil for the given transmitter-receiver distance. For the investigation area, the resolution of the tool is sufficiently high, up to 40

m radii. Further improvement can be obtained by sustaining detectable signal levels for the increased tool spacing. This can be achieved with better coil design, large EM contrast proppants or both. We also evaluated an inter-well deployment of the tool and found it practically challenging to detect the signals from the observation well. In the last sub-section for tool specifications, the potential of multi-frequency analyses in the recovery of conductivity distribution is demonstrated.

In the second half of the results, we demonstrated the potential of the induction tool in monitoring proppant settlement. By changing the shapes and keeping the total injected proppant volume the same, we have shown that the differential signals are distinguishable. Secondly, to improve the differential signals we can increase the magnetic permeability of the proppants ignoring related practical challenges. The differential signals are shown to be indifferent to the enhanced electrical permittivity. Lastly, the transverse component of background formation conductivity is shown to be dominating the accuracy of the inversion analyses.

5.5. FUTURE WORK

In this last section, we provide a list of several additional efforts that could be made to make the tool more efficient:

- The current design of the tool cannot handle in-situ bucking. This is a practical challenge which can cause a loss of accuracy in the measured signals. The surface control of the bucking, which is suggested in Yu et al. (2016), can be studied and incorporated into the current tool.
- Proppants with enhanced magnetic permeability can be used (ignoring practical limitations) in the field which was shown to further increase the signal levels compared to the case when only electrical conductivity is the contrast agent.

- The capability of multi frequency analysis can be added to the tool which may produce more information on a conductivity distribution inside the fracture. Although this may require only slight changes in the tool itself, significant changes in the computational study will be necessary. This may require time-domain analyses for the computation efficiency.
- In the inversion study, different shapes of fractures can be parametrized and used in the simulation to envision capabilities of the tool, especially in investigating proppant settlement. This will be more meaningful after obtaining field data.
- Current inversion analysis will recover information about the main branch of fractures. They can be extended to the generation of a conductivity map where secondary branches of fractures can also be monitored. The use of axial hybrid methods will be less costly because of lower computation dimensions, and the study can be further extended to three-dimensional numerical solutions where variable background formation conductivities can be computed.

Appendix

MOM SOLUTION

This Matlab code simulates a tri-axial induction tool in a 3-D spatial domain, and a Cartesian coordinate system is used for the computation. To run the program, one needs three input files, i.e., fracture.txt, operation.txt and sampling.txt. Fracture.txt contains the specifics of the circular fracture geometry, conductivity and node spacing coefficient on the edges of ellipses. An example is shown as follows:

0	% fracture location on the z-axis which is the wellbore axis, [m]
1	% fracture radius, it is r_major on the y-axis, [m]
1	% fracture aspect ratio, r_major/r_minor, [-]
0	% dip-angle, rotated about the x-axis which is the vertical axis, [˚]
100 100	% linearly decreasing conductivity, values at r_well and r_frac, [S/m]
0.005	% fracture thickness, [m]
0.1	% well radius, [m]
10	% node spacing coefficient on the inner and outer radius of ellipse, [-]

Operation.txt contains the specifics of the transmitter/receiver coils and the background formation (rock) conductivity. An example is shown as follows:

1000	% operation frequency, [Hz]
1500	% magnetic dipole moment, [A.m2]
600	% number of turns on receiver coil, [-]
0.003	% cross-sectional area of receiver coil [m2]
0.333	% background formation conductivity [S/m]

An example of sampling.txt is shown below where the first three columns show the Cartesian coordinates of transmitter, the second and third triads show the coordinates of the first and second receivers, respectively:

0	0	-2	0	0	-1.2	0	0	-0.8
0	0	-1.95	0	0	-1.15	0	0	-0.75
0	0	-1.9	0	0	-1.1	0	0	-0.7
0	0	-1.85	0	0	-1.05	0	0	-0.65
...	...	...	...	...	...	...	...	...
...	...	...	...	...	...	...	...	...

Main function:

```
clear all; close all; clc

string = strcat(pwd,'\Library\hfd_1m_0deg\');

timerVal = tic;

muo = 4*pi*1E-7;          % free space electrical permeability, [H/m]
epso = 8.854187817*1E-12; % free space permittivity, [F/m]

opcon = load(strcat(string,'operation.txt'));

omega = 2*pi*opcon(1);    % angular frequency, [rad.Hz]

k1 = sqrt(muo*epso*omega^2-1j*muo*opcon(5)*omega);

geometry(string);

tic; [Zmn,Bmn] = impedance(k1); T1 = toc;

Tmn = 1j*omega*muo*Zmn+Bmn;

tic; Hsca = scattered(k1,Tmn,string); T2 = toc;

Mtr = prod(opcon(2:4));

Vxz = -1j*(muo*omega)^2*Mtr*(Hsca(:,1))*1e6;
Vyz = -1j*(muo*omega)^2*Mtr*(Hsca(:,2))*1e6;
Vzz = -1j*(muo*omega)^2*Mtr*(Hsca(:,3))*1e6;

out = [real(Vxz) imag(Vxz) real(Vyz) imag(Vyz) real(Vzz) imag(Vzz)];

dlmwrite(strcat(string,'out.dat'),out,'delimiter','\t');

T3 = toc(timerVal);

fid = fopen(strcat(string,'info.dat'),'w+');

fprintf(fid,'%f \t %% matrix fill time\n',T1);
fprintf(fid,'%d \t\t %% number of unknowns\n',size(Bmn,1));
fprintf(fid,'%f \t %% matrix solution time for all points\n',T2);
fprintf(fid,'%d \t\t %% number of source points\n',size(Vzz,1));
fprintf(fid,'%f \t %% total run time\n',T3);

fclose(fid);
```

Incident function calculates Eq. 2.23 and 2.24 in spherical coordinates and converts them to Cartesian coordinates:

```
function Ec = Einc(k1,R1,R2)

    % Given two coordinates: observation (R1) and source (R2)
    % Es is the electrical field in spherical coordinates
    % Ec is the electrical field in Cartesian coordinates [Ex,Ey,Ez]
    % The source is z-oriented

    global NofD

    r(:,1) = R1(:,1)-R2(1,1);
    r(:,2) = R1(:,2)-R2(1,2);
    r(:,3) = R1(:,3)-R2(1,3);

    R = sqrt(sum(r.*r,2));

    teta = acosd(r(:,3)./R);        % 0<teta<180
    phi = atand(r(:,2)./r(:,1));    % 0<phi<360

    v1 = r(:,1)<0;
    v2 = r(:,2)<0;

    phi = phi+v1*180;
    phi = phi+(~v1.*v2)*360;

    Es = k1*sind(teta)./(4*pi*R).*(1+1./(1j*k1*R)).*exp(-1j*k1*R);
    Ec = [-sind(phi).*Es cosd(phi).*Es zeros(NofD,1)];

end
```

Gauss function provides integration points and weight for all triangular elements; order of Gaussian quadrature is 2:

```
function [Rn,Wn,Pn] = gauss(R1,R2,R3)

    xw=[0.16666666666667 0.16666666666667 0.33333333333333;
        0.16666666666667 0.66666666666667 0.33333333333333;
        0.66666666666667 0.16666666666667 0.33333333333333];

    global NofT
```

```
    Pn = size(xw,1);
    Wn = xw(:,3);

    N1 = 1-xw(:,2)-xw(:,1);
    N2 = xw(:,2);
    N3 = xw(:,1);

    Rn = zeros(NofT,3,Pn);

    for k = 1:Pn
        Rn(:,:,k) = R1*N1(k)+R2*N2(k)+R3*N3(k);
    end

end
```

The geometry function creates nodes for the circles defined with the input parameters. The outputs also include connectivity and construction maps for the vectorized calculations. Any mesh generator can be adopted for this job. Details and structure of global outputs are shown below:

```
function [] = geometry(string)

    % NofV: number of vertices
    % NofD: number of edges
    % NofT: number of triangles
    % TtoV  [NofTx3]: vertices of triangle
    % VtoR  [NofVx3]: x,y,z coordinates of vertex
    % TtoD  [NofTx4]: edges of triangle, no bndry edge: 4th-column 2or3
    % TtoD1 [NofTx6]: edge for which triangle is Tp(1:3) && Tm(4:6)
    % DtoT  [NofDx6]: [Tp,Tm,Vp,Vm,Ve,Vw] of edge
    % AofT  [NofTx1]: area of triangles
    % GofT  [NofTx1]: conductance of triangle
    % RofC  [NofTx3]: coordinates of triangle's center
    % lofD  [NofDx1]: edge length
    % RofCp [NofDx3]: center of edge's positive triangle
    % RofCm [NofDx3]: center of edge's minus triangle
    % rhocp [NofDx3]: vector to center of edge's positive triangle
    % rhocm [NofDx3]: vector from center of edge's minus triangle

    fid = fopen(strcat(string,'fracture.txt'));

    origin = str2num(strtok(fgetl(fid),'%'));
    r_frac = str2num(strtok(fgetl(fid),'%'));
    aspect = str2num(strtok(fgetl(fid),'%'));
    dipang = str2num(strtok(fgetl(fid),'%'));
```

```
    S_frac = str2num(strtok(fgetl(fid),'%'));
    t_frac = str2num(strtok(fgetl(fid),'%'));
    r_well = str2num(strtok(fgetl(fid),'%'));
    lambda = str2num(strtok(fgetl(fid),'%'));

    fclose(fid);

     …

end
```

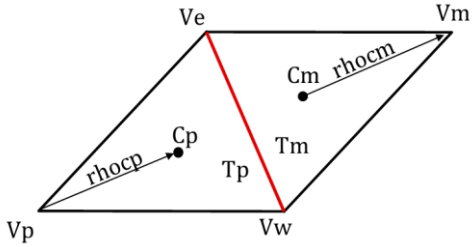

The impedance function fills the impedance and boundary matrices:

```
function [Zmn,Bmn] = impedance(k1)

    global VtoR DtoT TtoD TtoD1 TtoV NofD NofT
    global RofC rhocp rhocm lofD AofT GofT

    R1 = VtoR(TtoV(:,1),:);
    R2 = VtoR(TtoV(:,2),:);
    R3 = VtoR(TtoV(:,3),:);

    [Rn,Wn,Pn] = gauss(R1,R2,R3);

    Lpn = zeros(NofD,3,Pn);
    Lmn = zeros(NofD,3,Pn);
    Gmn = zeros(NofT,NofT,Pn);

    for k = 1:Pn
        rhop = Rn(DtoT(:,1),:,k)-VtoR(DtoT(:,3),:);
        rhom = VtoR(DtoT(:,4),:)-Rn(DtoT(:,2),:,k);
        Lpn(:,1,k) = lofD.*rhop(:,1)/2;
        Lpn(:,2,k) = lofD.*rhop(:,2)/2;
        Lpn(:,3,k) = lofD.*rhop(:,3)/2;
        Lmn(:,1,k) = lofD.*rhom(:,1)/2;
        Lmn(:,2,k) = lofD.*rhom(:,2)/2;
        Lmn(:,3,k) = lofD.*rhom(:,3)/2;
        Gmn(:,:,k) = green1(k1,RofC,Rn(:,:,k));
    end

    Zmn = zeros(NofD,NofD);

    for n = 1:NofD
        Pp = zeros(NofD,1);
```

```
        Pm = zeros(NofD,1);
        Ap = zeros(NofD,3);
        Am = zeros(NofD,3);
        for k = 1:Pn
            Gpp = Gmn(DtoT(:,1),DtoT(n,1),k);
            Gmp = Gmn(DtoT(:,2),DtoT(n,1),k);
            Gpm = Gmn(DtoT(:,1),DtoT(n,2),k);
            Gmm = Gmn(DtoT(:,2),DtoT(n,2),k);
            Pp = Pp+lofD(n)*(Gpp-Gpm)*Wn(k);
            Pm = Pm+lofD(n)*(Gmp-Gmm)*Wn(k);
            Ap(:,1) = Ap(:,1)+(Lpn(n,1,k)*Gpp+Lmn(n,1,k)*Gpm)*Wn(k);
            Ap(:,2) = Ap(:,2)+(Lpn(n,2,k)*Gpp+Lmn(n,2,k)*Gpm)*Wn(k);
            Ap(:,3) = Ap(:,3)+(Lpn(n,3,k)*Gpp+Lmn(n,3,k)*Gpm)*Wn(k);
            Am(:,1) = Am(:,1)+(Lpn(n,1,k)*Gmp+Lmn(n,1,k)*Gmm)*Wn(k);
            Am(:,2) = Am(:,2)+(Lpn(n,2,k)*Gmp+Lmn(n,2,k)*Gmm)*Wn(k);
            Am(:,3) = Am(:,3)+(Lpn(n,3,k)*Gmp+Lmn(n,3,k)*Gmm)*Wn(k);
        end
        Zmn(:,n) = (sum(Ap.*rhocp+Am.*rhocm,2))/2+(Pm-Pp)/k1^2;
    end

    Lcpn = zeros(NofD+1,3);
    Lcmn = zeros(NofD+1,3);

    Lcpn(1:NofD,1) = lofD.*rhocp(:,1)/2./...
                     AofT(DtoT(:,1))./GofT(DtoT(:,1));
    Lcpn(1:NofD,2) = lofD.*rhocp(:,2)/2./...
                     AofT(DtoT(:,1))./GofT(DtoT(:,1));
    Lcpn(1:NofD,3) = lofD.*rhocp(:,3)/2./...
                     AofT(DtoT(:,1))./GofT(DtoT(:,1));
    Lcmn(1:NofD,1) = lofD.*rhocm(:,1)/2./...
                     AofT(DtoT(:,2))./GofT(DtoT(:,2));
    Lcmn(1:NofD,2) = lofD.*rhocm(:,2)/2./...
                     AofT(DtoT(:,2))./GofT(DtoT(:,2));
    Lcmn(1:NofD,3) = lofD.*rhocm(:,3)/2./...
                     AofT(DtoT(:,2))./GofT(DtoT(:,2));

    Lrp1 = rhocp.*(Lcpn(TtoD1(DtoT(:,1),1),:)+...
                   Lcmn(TtoD1(DtoT(:,1),4),:));
    Lrp2 = rhocp.*(Lcpn(TtoD1(DtoT(:,1),2),:)+...
                   Lcmn(TtoD1(DtoT(:,1),5),:));
    Lrp3 = rhocp.*(Lcpn(TtoD1(DtoT(:,1),3),:)+...
                   Lcmn(TtoD1(DtoT(:,1),6),:));
    Lrm1 = rhocm.*(Lcpn(TtoD1(DtoT(:,2),1),:)+...
                   Lcmn(TtoD1(DtoT(:,2),4),:));
    Lrm2 = rhocm.*(Lcpn(TtoD1(DtoT(:,2),2),:)+...
                   Lcmn(TtoD1(DtoT(:,2),5),:));
    Lrm3 = rhocm.*(Lcpn(TtoD1(DtoT(:,2),3),:)+...
                   Lcmn(TtoD1(DtoT(:,2),6),:));

    Bmn = spalloc(NofD,NofD+1,5*NofD);

    Bmn = Bmn+sparse(1:NofD,TtoD(DtoT(:,1),1),...
```

```
                sum(Lrp1,2)/2,NofD,NofD+1);
    Bmn = Bmn+sparse(1:NofD,TtoD(DtoT(:,1),2),...
                sum(Lrp2,2)/2,NofD,NofD+1);
    Bmn = Bmn+sparse(1:NofD,TtoD(DtoT(:,1),3),...
                sum(Lrp3,2)/2,NofD,NofD+1);
    Bmn = Bmn+sparse(1:NofD,TtoD(DtoT(:,2),1),...
                sum(Lrm1,2)/2,NofD,NofD+1);
    Bmn = Bmn+sparse(1:NofD,TtoD(DtoT(:,2),2),...
                sum(Lrm2,2)/2,NofD,NofD+1);
    Bmn = Bmn+sparse(1:NofD,TtoD(DtoT(:,2),3),...
                sum(Lrm3,2)/2,NofD,NofD+1);

    Bmn(:,NofD+1) = [];

    display('impedance and boundary matrix is constructed')

end

function G = green1(k1,R1,R2)

    % R1 is the observer
    % R2 is the source point

    global NofT

    R = zeros(NofT);

    for j = 1:NofT
        r(:,1) = R1(:,1)-R2(j,1);
        r(:,2) = R1(:,2)-R2(j,2);
        r(:,3) = R1(:,3)-R2(j,3);
        R(:,j) = sqrt(sum(r.*r,2));
    end

    G = exp(-1j*k1*R)./(4*pi*R);

end
```

The scattered function calculates differential magnetic fields for all sampling points:

```
function [Hsca] = scattered(k1,Tmn,string)

    global VtoR DtoT TtoD1 TtoV NofD NofT
    global RofCp RofCm rhocp rhocm lofD

    R1 = VtoR(TtoV(:,1),:);
```

```
R2 = VtoR(TtoV(:,2),:);
R3 = VtoR(TtoV(:,3),:);

[Rn,Wn,Pn] = gauss(R1,R2,R3);

Lpn = zeros(NofD,3,Pn);
Lmn = zeros(NofD,3,Pn);

for k = 1:Pn
    rhop = Rn(DtoT(:,1),:,k)-VtoR(DtoT(:,3),:);
    rhom = VtoR(DtoT(:,4),:)-Rn(DtoT(:,2),:,k);
    Lpn(:,1,k) = lofD.*rhop(:,1)/2;
    Lpn(:,2,k) = lofD.*rhop(:,2)/2;
    Lpn(:,3,k) = lofD.*rhop(:,3)/2;
    Lmn(:,1,k) = lofD.*rhom(:,1)/2;
    Lmn(:,2,k) = lofD.*rhom(:,2)/2;
    Lmn(:,3,k) = lofD.*rhom(:,3)/2;
end

sampling = load(strcat(string,'sampling.txt'));

RofS = sampling(:,1:3);
RofO1 = sampling(:,4:6);
RofO2 = sampling(:,7:9);

alfa = (sum((RofO1-RofS).^2,2)./sum((RofO2-RofS).^2,2)).^(3/2);

Nosp = size(RofS,1);
Hsca = zeros(Nosp,3);

[TLmn,TUmn] = lu(Tmn);

for i = 1:Nosp

    Ep = Einc(k1,RofCp,RofS(i,:));
    Em = Einc(k1,RofCm,RofS(i,:));
    Vm = sum(rhocp.*Ep+rhocm.*Em,2)/2;

    In = TUmn\(TLmn\Vm);

    Jd = zeros(NofT,3,Pn);

    LIpn = zeros(NofD+1,3,Pn);
    LImn = zeros(NofD+1,3,Pn);

    for k = 1:Pn
        LIpn(1:NofD,1,k) = Lpn(:,1,k).*In;
        LIpn(1:NofD,2,k) = Lpn(:,2,k).*In;
        LIpn(1:NofD,3,k) = Lpn(:,3,k).*In;
        LImn(1:NofD,1,k) = Lmn(:,1,k).*In;
```

```
            LImn(1:NofD,2,k) = Lmn(:,2,k).*In;
            LImn(1:NofD,3,k) = Lmn(:,3,k).*In;
        end

        Jd = Jd+LIpn(TtoD1(:,1),:,:)+LImn(TtoD1(:,4),:,:);
        Jd = Jd+LIpn(TtoD1(:,2),:,:)+LImn(TtoD1(:,5),:,:);
        Jd = Jd+LIpn(TtoD1(:,3),:,:)+LImn(TtoD1(:,6),:,:);

        GG1 = green2(k1,RofO1(i,:),Rn);
        GG2 = green2(k1,RofO2(i,:),Rn);

        G1J = permute(sum(cross(GG1,Jd),1),[3 2 1]);
        G2J = permute(sum(cross(GG2,Jd),1),[3 2 1]);

        Hsca1(1,1) = sum(G1J(:,1).*Wn,1);
        Hsca1(1,2) = sum(G1J(:,2).*Wn,1);
        Hsca1(1,3) = sum(G1J(:,3).*Wn,1);
        Hsca2(1,1) = sum(G2J(:,1).*Wn,1);
        Hsca2(1,2) = sum(G2J(:,2).*Wn,1);
        Hsca2(1,3) = sum(G2J(:,3).*Wn,1);

        Hsca(i,:) = Hsca2-Hsca1*alfa(i);

    end
end

function GG = green2(k1,R1,R2)

    % R1 is the observer; R2 is the source point
    % GG is the gradient of Green's function

    global NofT

    Pn = size(R2,3);
    GG = zeros(NofT,3,Pn);

    for k = 1:Pn
        r(:,1) = R1(1,1)-R2(:,1,k);
        r(:,2) = R1(1,2)-R2(:,2,k);
        r(:,3) = R1(1,3)-R2(:,3,k);

        R = sqrt(sum(r.*r,2));
        G = exp(-1j*k1*R)./(4*pi*R);
        const = -(1+1j*k1*R).*G./R.^2;

        GG(:,1,k) = r(:,1).*const;
        GG(:,2,k) = r(:,2).*const;
        GG(:,3,k) = r(:,3).*const;
    end
end
```

Output file info.dat provides information on the computation time (matrix fill time, matrix solution time for all sampling points and total run time), number of unknowns and number of source points. The out.dat provides calculated real and imaginary voltages for all orientations of receiver coil (transmitter coil is *z*-oriented) and for all sampling points.

AXIAL HYBRID SOLUTION

This Matlab code simulates the tri-axial induction tool in axially symmetric and transversely isotropic formations. A cylindrical coordinate system is used for the computation. To run the program, one needs four input files, i.e., formation.txt, meshing.txt, operation.txt and sampling.txt. The formation.txt contains the horizontal and radial boundaries of a layered medium and electrical conductivity and magnetic permeability of layers. An example is shown as follows:

```
3, 3              % number of horizontal layers, number of radial layers [-]
-0.0025, 0.0025       % z values of horizontal boundaries [m]
0.1, 18           % rho values of radial boundaries for given horizontal layer [m]
0.3, 0.3, 0.3     % sigma values of radial layers for given horizontal layer [S/m]
0.3, 100, 0.3     % sigma values of radial layers for given horizontal layer [S/m]
0.3, 0.3, 0.3     % sigma values of radial layers for given horizontal layer [S/m]
1, 1, 1  % relative permeability values of radial layers for given horizontal layer [-]
1, 1, 1  % relative permeability values of radial layers for given horizontal layer [-]
1, 1, 1  % relative permeability values of radial layers for given horizontal layer [-]
```

The meshing.txt is the input of gridding scheme on the *z*-axis (horizontal wellbore axis). An example is shown as follows:

```
-1                % start of uniform meshing section [m]
1                 % end of uniform meshing [m]
0.1               % element size in the middle uniform part of the grid [m]
1.25              % size ratio of two adjacent elements in the expanding part [-]
10.0              % truncation of the domain on both edges [m]
```

The operation.txt contains the specifics of the transmitter/receiver coils. An example is shown as follows:

```
1000        % operation frequency [Hz]
1500        % magnetic dipole moment [A.m2]
600         % number of turns on receiver coil [-]
0.003       % cross-sectional area of receiver coil [m2]
```

An example of sampling.txt is shown below:

```
-2          % first logging point (Tx location) [m]
0           % last logging point (Tx location) [m]
41          % number of logging points [-]
0.8         % distance between transmitter and the first receiver coil [m]
1.2         % distance between transmitter and the second receiver coil [m]
```

Main function:

```
clear all; close all; clc

string = strcat(pwd,'\Library\run_MM_short\');

timerVal = tic;

global muo omega Nb

muo = 4*pi*1E-7;    % free space electrical permeability, [H/m]

MMtr = indata(string);
stat = meshing(string);

tic; [Cmat,Lambda] = eigencall(stat); T1=toc;
tic; [Q,Hc0p,Jc0p] = refmatrix(stat,Cmat,Lambda); T2=toc;
tic; [z_obsr,Hsca] = scattered(string,Cmat,Lambda,Q,Hc0p,Jc0p); T3=toc;

Vzz_sca = 1j*muo*omega*MMtr*Hsca*1e6;

out = [real(Vzz_sca) imag(Vzz_sca)];

dlmwrite(strcat(string,'out.dat'),out,'delimiter','\t');

T4 = toc(timerVal);

fid = fopen(strcat(string,'info.dat'),'w+');
```

```
fprintf(fid,'%f \t %% the solution of eigenvalue problem\n',T1);
fprintf(fid,'%d \t %% number of basis functions\n',Nb);
fprintf(fid,'%f \t %% calculation of refraction matrix\n',T2);
fprintf(fid,'%f \t %% solution time for all points\n',T3);
fprintf(fid,'%d \t %% number of source points\n',size(Vzz_sca,1));
fprintf(fid,'%f \t %% total run time\n',T4);

fclose(fid);
```

The indata function globally defines input values:

```
function [Mtr] = indata(string)

    global Nz Nr bnd_z bnd_r sigma_sz mur_sz omega nord Nord

    fid = fopen(strcat(string,'formation.txt'));

    Nzr = str2num(strtok(fgetl(fid),'%'));

    Nz = Nzr(1);       % number of layers in the wellbore direction
    Nr = Nzr(2);       % number of layers in the radial direction

    bnd_z = str2num(strtok(fgetl(fid),'%'));
    bnd_r = str2num(strtok(fgetl(fid),'%'));

    sigma_sz = zeros(Nz,Nr);
    mur_sz = zeros(Nz,Nr);

    for i = 1:Nz
        sigma_sz(i,:) = str2num(strtok(fgetl(fid),'%'));
    end

    for i = 1:Nz
        mur_sz(i,:) = str2num(strtok(fgetl(fid),'%'));
    end

    fclose(fid);

    fid = fopen(strcat(string,'operation.txt'));

    freq = str2num(strtok(fgetl(fid),'%'));
    Mtx = str2num(strtok(fgetl(fid),'%'));
    Nrx = str2num(strtok(fgetl(fid),'%'));
    Arx = str2num(strtok(fgetl(fid),'%'));

    fclose(fid);
```

```
    Mtr = Mtx*Nrx*Arx;
    omega = 2*pi*freq;

    % ---------------------- Fourier series ------------------------ %

    nordmin = 0;
    nordmax = 1;

    nord = (nordmin:nordmax)';
    Nord = length(nord);

end
```

The meshing function creates grids based on the scheme defined in the meshing.txt, adds additional grids due to the formation and creates construction vectors for the vectorized computation:

```
function [stat] = meshing(string)

    global Zglobal dz Nz Nr bnd_z Ne Nb B1 B2

    fid = fopen(strcat(string,'meshing.txt'));

    zlog1 = str2num(strtok(fgetl(fid),'%'));
    zlogN = str2num(strtok(fgetl(fid),'%'));
    Dz = str2num(strtok(fgetl(fid),'%'));
    Qexp = str2num(strtok(fgetl(fid),'%'));
    zmax = str2num(strtok(fgetl(fid),'%'));

    fclose(fid);

    zlog1 = zlog1-1;
    zlogN = zlogN+1;

    Zmiddle = (zlog1:Dz:zlogN)';

    Nright = ceil(log((zmax-zlogN)/Dz*(1-1/Qexp)+1)/log(Qexp))+2;

    Zright = zeros(Nright,1);

    for i = 1:Nright
        Zright(i) = zlogN+Dz*sum(power(Qexp,(1:i)));
    end
```

```
    Nleft = ceil(log((zmax+zlog1)/Dz*(1-1/Qexp)+1)/log(Qexp))+2;

    Zleft = zeros(Nleft,1);

    for i = 1:Nleft
        Zleft(i) = zlog1-Dz*sum(power(Qexp,(1:i)));
    end

    Zglobal = [flipud(Zleft)',Zmiddle',Zright']';

    idx = zeros(Nz-1,1);

    for i = 1:Nz-1
        if sum(bnd_z(i)==Zglobal)
            idx(i) = sum(bnd_z(i)>Zglobal)+1;
        else
            idx(i) = sum(bnd_z(i)>Zglobal);
            Zglobal = [Zglobal(1:idx(i));bnd_z(i);...
                       Zglobal(idx(i)+1:end)];
            idx(i) = idx(i)+1;
        end
    end

    dz = Zglobal(2:end)-Zglobal(1:end-1);

    Ng = length(Zglobal);       % number of grids
    Ne = Ng-1;                  % number of elements
    Nb = 2*(Ne-1);              % number of basis functions

    idx = [1;idx;Ng];

    B1 = 1:Nb;
    B2 = B1+Nb;

    global muo omega sigma_sz mur_sz

    stat.qe = zeros(Ne,Nr);
    stat.qh = zeros(Ne,Nr);

    for j = 1:Nr
        for i = 1:Nz
            stat.qe(idx(i):idx(i+1)-1,j) = sigma_sz(i,j);
            stat.qh(idx(i):idx(i+1)-1,j) = mur_sz(i,j);
        end
    end

    stat.k2 = 1j*omega*muo*stat.qe.*stat.qh;

end
```

The integral function analytically calculates Eqs. 2.43-2.44 and 2.49-2.52:

```
function GG = integral(cx,qx1,qx2,flag)

    global Ne

    gg = zeros(Ne,4,4);

    if flag == 1
        gg = gxgx(cx,qx1,qx2);
    elseif flag == 2
        gg = gxgxd(cx,qx1,qx2);
    elseif flag == 3
        gg = gxdgxd(cx,qx1,qx2);
    end

    GG = assembly(gg);

end

function gg = gxgx(cx,qx1,qx2)

    global dz

    gg(:,1,1) = 13/35*dz.*cx;
    gg(:,1,2) = 11/210*qx2.*dz.*dz.*cx;
    gg(:,1,3) = 9/70*dz.*cx;
    gg(:,1,4) = -13/420*qx2.*dz.*dz.*cx;

    gg(:,2,1) = 11/210*qx1.*dz.*dz.*cx;
    gg(:,2,2) = 1/105*qx1.*dz.*qx2.*dz.*dz.*cx;
    gg(:,2,3) = 13/420*qx1.*dz.*dz.*cx;
    gg(:,2,4) = -1/140*qx1.*dz.*qx2.*dz.*dz.*cx;

    gg(:,3,1) = 9/70*dz.*cx;
    gg(:,3,2) = 13/420*qx2.*dz.*dz.*cx;
    gg(:,3,3) = 13/35*dz.*cx;
    gg(:,3,4) = -11/210*qx2.*dz.*dz.*cx;

    gg(:,4,1) = -13/420*qx1.*dz.*dz.*cx;
    gg(:,4,2) = -1/140*qx1.*dz.*qx2.*dz.*dz.*cx;
    gg(:,4,3) = -11/210*qx1.*dz.*dz.*cx;
    gg(:,4,4) = 1/105*qx1.*dz.*qx2.*dz.*dz.*cx;

end

function gg = gxgxd(cx,qx1,qx2)
```

```
    global dz Ne

    gg(:,1,1) = -1/2*cx;
    gg(:,1,2) = 1/10*qx2.*dz.*cx;
    gg(:,1,3) = 1/2*cx;
    gg(:,1,4) = -1/10*qx2.*dz.*cx;

    gg(:,2,1) = -1/10*qx1.*dz.*cx;
    gg(:,2,2) = zeros(Ne,1);
    gg(:,2,3) = 1/10*qx1.*dz.*cx;
    gg(:,2,4) = -1/60*qx1.*qx2.*dz.*dz.*cx;

    gg(:,3,1) = -1/2*cx;
    gg(:,3,2) = -1/10*qx2.*dz.*cx;
    gg(:,3,3) = 1/2*cx;
    gg(:,3,4) = 1/10*qx2.*dz.*cx;

    gg(:,4,1) = 1/10*qx1.*dz.*cx;
    gg(:,4,2) = 1/60*qx1.*qx2.*dz.*dz.*cx;
    gg(:,4,3) = -1/10*qx1.*dz.*cx;
    gg(:,4,4) = zeros(Ne,1);

end

function gg = gxdgxd(cx,qx1,qx2)

    global dz

    gg(:,1,1) = 6/5*cx./dz;
    gg(:,1,2) = 1/10*qx2.*cx;
    gg(:,1,3) = -6/5*cx./dz;
    gg(:,1,4) = 1/10*qx2.*cx;

    gg(:,2,1) = 1/10*qx1.*cx;
    gg(:,2,2) = 2/15*qx1.*qx2.*dz.*cx;
    gg(:,2,3) = -1/10*qx1.*cx;
    gg(:,2,4) = -1/30*qx1.*qx2.*dz.*cx;

    gg(:,3,1) = -6/5*cx./dz;
    gg(:,3,2) = -1/10*qx2.*cx;
    gg(:,3,3) = 6/5*cx./dz;
    gg(:,3,4) = -1/10*qx2.*cx;

    gg(:,4,1) = 1/10*qx1.*cx;
    gg(:,4,2) = -1/30*qx1.*qx2.*dz.*cx;
    gg(:,4,3) = -1/10*qx1.*cx;
    gg(:,4,4) = 2/15*qx1.*qx2.*dz.*cx;

end
```

```
function GG = assembly(gg)

    global Ne Nb

    GG = sparse(Nb,Nb);

    idx1 = 1:2:Nb;
    idx2 = 2:2:Nb;

    GG = GG+sparse(idx1,idx1,gg(1:Ne-1,3,3)+gg(2:Ne,1,1),Nb,Nb);
    GG = GG+sparse(idx1,idx2,gg(1:Ne-1,3,4)+gg(2:Ne,1,2),Nb,Nb);
    GG = GG+sparse(idx2,idx1,gg(1:Ne-1,4,3)+gg(2:Ne,2,1),Nb,Nb);
    GG = GG+sparse(idx2,idx2,gg(1:Ne-1,4,4)+gg(2:Ne,2,2),Nb,Nb);

    GG = GG+sparse(idx1(2:Ne-1),idx1(1:Ne-2),gg(2:Ne-1,3,1),Nb,Nb);
    GG = GG+sparse(idx1(2:Ne-1),idx2(1:Ne-2),gg(2:Ne-1,3,2),Nb,Nb);

    GG = GG+sparse(idx1(1:Ne-2),idx1(2:Ne-1),gg(2:Ne-1,1,3),Nb,Nb);
    GG = GG+sparse(idx1(1:Ne-2),idx2(2:Ne-1),gg(2:Ne-1,1,4),Nb,Nb);

    GG = GG+sparse(idx2(2:Ne-1),idx1(1:Ne-2),gg(2:Ne-1,4,1),Nb,Nb);
    GG = GG+sparse(idx2(2:Ne-1),idx2(1:Ne-2),gg(2:Ne-1,4,2),Nb,Nb);

    GG = GG+sparse(idx2(1:Ne-2),idx1(2:Ne-1),gg(2:Ne-1,2,3),Nb,Nb);
    GG = GG+sparse(idx2(1:Ne-2),idx2(2:Ne-1),gg(2:Ne-1,2,4),Nb,Nb);

    GG = full(GG);

end
```

The eigencall function calculates eigenvalues and eigenvectors for each radial layer, and it verifies orthogonality condition shown in Eq. 2.45:

```
function [Cmat,Lambda] = eigencall(stat)

    global Nr Nb B1 B2

    Cmat = zeros(2*Nb,2*Nb,Nr);

    Lambda = zeros(2*Nb,Nr);

    for l = 1:Nr
        A1e = integral(-1./stat.qe(:,l),stat.qe(:,l),stat.qe(:,l),3);
        A1h = integral(-1./stat.qh(:,l),stat.qh(:,l),stat.qh(:,l),3);

        A2e = integral(stat.k2(:,l)./...
```

```
                        stat.qe(:,l),stat.qe(:,l),stat.qe(:,l),1);
        A2h = integral(stat.k2(:,l)./...
                        stat.qh(:,l),stat.qh(:,l),stat.qh(:,l),1);

        Be = integral(1./stat.qe(:,l),stat.qe(:,l),stat.qe(:,l),1);
        Bh = integral(1./stat.qh(:,l),stat.qh(:,l),stat.qh(:,l),1);

        Ae = A1e+A2e;
        Ah = A1h+A2h;

        [CCe,DDe] = eig(Ae,Be,'vector');
        [CCh,DDh] = eig(Ah,Bh,'vector');

        Cmat(B1,B1,l) = orthog(CCe,Be);
        Cmat(B2,B2,l) = orthog(CCh,Bh);

        Lambda(B1,l) = sqrt(DDe);
        Lambda(B2,l) = sqrt(DDh);
    end

end

function Ceta = orthog(Ceta_old,Beta)

    global Nb

    Ceta = Ceta_old;
    noneI = transpose(Ceta_old)*Beta*Ceta_old;
    noneI = sqrt(1./diag(noneI));

    for i = 1:Nb
        Ceta(:,i) = Ceta_old(:,i)*noneI(i);
    end

end
```

The calculation of generalized refraction matrix:

```
function [Q,Hc0p,Jc0p] = refmatrix(stat,Cmat,Lambda)

    global Nr Nb B1 B2

    P1p = zeros(2*Nb,2*Nb,Nr-1);
    P1m = zeros(2*Nb,2*Nb,Nr-1);
    P2p = zeros(2*Nb,2*Nb,Nr-1);
    P2m = zeros(2*Nb,2*Nb,Nr-1);

    Dhep = zeros(Nb,Nb,Nr-1);
```

```
    Dehp = zeros(Nb,Nb,Nr-1);

    Dhem = zeros(Nb,Nb,Nr-1);
    Dehm = zeros(Nb,Nb,Nr-1);

    for l = 1:Nr-1

        pe1p =
integral(1./stat.pe(:,l+1),stat.qe(:,l),stat.qe(:,l+1),1);
        P1p(B1,B1,l) = transpose(Cmat(B1,B1,l))*pe1p*Cmat(B1,B1,l+1);
        ph1p =
integral(1./stat.ph(:,l+1),stat.qh(:,l),stat.qh(:,l+1),1);
        P1p(B2,B2,l) = transpose(Cmat(B2,B2,l))*ph1p*Cmat(B2,B2,l+1);

        pe1m = integral(1./stat.pe(:,l),stat.qe(:,l+1),stat.qe(:,l),1);
        P1m(B1,B1,l) = transpose(Cmat(B1,B1,l+1))*pe1m*Cmat(B1,B1,l);
        ph1m = integral(1./stat.ph(:,l),stat.qh(:,l+1),stat.qh(:,l),1);
        P1m(B2,B2,l) = transpose(Cmat(B2,B2,l+1))*ph1m*Cmat(B2,B2,l);

        pe2p = integral(1./stat.pe(:,l),stat.qe(:,l),stat.qe(:,l+1),1);
        P2p(B1,B1,l) = transpose(Cmat(B1,B1,l))*pe2p*Cmat(B1,B1,l+1);
        ph2p = integral(1./stat.ph(:,l),stat.qh(:,l),stat.qh(:,l+1),1);
        P2p(B2,B2,l) = transpose(Cmat(B2,B2,l))*ph2p*Cmat(B2,B2,l+1);

        pe2m =
integral(1./stat.pe(:,l+1),stat.qe(:,l+1),stat.qe(:,l),1);
        P2m(B1,B1,l) = transpose(Cmat(B1,B1,l+1))*pe2m*Cmat(B1,B1,l);
        ph2m =
integral(1./stat.ph(:,l+1),stat.qh(:,l+1),stat.qh(:,l),1);
        P2m(B2,B2,l) = transpose(Cmat(B2,B2,l+1))*ph2m*Cmat(B2,B2,l);

        dhep =
integral(1./stat.ph(:,l)./stat.qe(:,l+1),stat.qh(:,l),stat.qe(:,l+1),2)
;
        Dhep(:,:,l) = transpose(Cmat(B2,B2,l))*dhep*Cmat(B1,B1,l+1);
        dehp =
integral(1./stat.pe(:,l)./stat.qh(:,l+1),stat.qe(:,l),stat.qh(:,l+1),2)
;
        Dehp(:,:,l) = transpose(Cmat(B1,B1,l))*dehp*Cmat(B2,B2,l+1);

        dhem =
integral(1./stat.ph(:,l+1)./stat.qe(:,l),stat.qh(:,l+1),stat.qe(:,l),2)
;
        Dhem(:,:,l) = transpose(Cmat(B2,B2,l+1))*dhem*Cmat(B1,B1,l);
        dehm =
integral(1./stat.pe(:,l+1)./stat.qh(:,l),stat.qe(:,l+1),stat.qh(:,l),2)
;
        Dehm(:,:,l) = transpose(Cmat(B1,B1,l+1))*dehm*Cmat(B2,B2,l);

    end
```

```
    Dhe = zeros(Nb,Nb,Nr);
    Deh = zeros(Nb,Nb,Nr);

    for l = 1:Nr

        dhe =
integral(1./stat.ph(:,l)./stat.qe(:,l),stat.qh(:,l),stat.qe(:,l),2);
        Dhe(:,:,l) = transpose(Cmat(B2,B2,l))*dhe*Cmat(B1,B1,l);
        deh =
integral(1./stat.pe(:,l)./stat.qh(:,l),stat.qe(:,l),stat.qh(:,l),2);
        Deh(:,:,l) = transpose(Cmat(B1,B1,l))*deh*Cmat(B2,B2,l);

    end

    display('done with static part')

    global muo bnd_r omega nord Nord

    Hc0m = zeros(2*Nb,Nr-1,Nord);
    Jc0m = zeros(2*Nb,Nr-1,Nord);
    Hc0p = zeros(2*Nb,Nr-1,Nord);
    Jc0p = zeros(2*Nb,Nr-1,Nord);

    Hc1m = zeros(2*Nb,Nr-1,Nord);
    Jc1m = zeros(2*Nb,Nr-1,Nord);
    Hc1p = zeros(2*Nb,Nr-1,Nord);
    Jc1p = zeros(2*Nb,Nr-1,Nord);

    for l = 1:Nr-1

        Lm = Lambda(:,l+1)*bnd_r(l);
        Lp = Lambda(:,l)*bnd_r(l);

        Am = imag(Lm)<0;
        Ap = imag(Lp)<0;

        for i = 1:Nord
            Hc0m(:,l,i) = besselh(nord(i),1,Lm,1);
            Jc0m(:,l,i) = besselj(nord(i),Lm,1).*exp(1j*real(Lm));
            Jc0m(Am,l,i) = Jc0m(Am,l,i).*exp(-2*imag(Lm(Am)));
            Hc0p(:,l,i) = besselh(nord(i),1,Lp,1);
            Jc0p(:,l,i) = besselj(nord(i),Lp,1).*exp(1j*real(Lp));
            Jc0p(Ap,l,i) = Jc0p(Ap,l,i).*exp(-2*imag(Lp(Ap)));
        end

        for i = 1:Nord
            if i == 1
                Left1 = besselh(nord(i)-1,1,Lm,1);
                Left2 = besselj(nord(i)-1,Lm,1).*exp(1j*real(Lm));
                Left2(Am) = Left2(Am).*exp(-2*imag(Lm(Am)));
```

```
                Left3 = besselh(nord(i)-1,1,Lp,1);
                Left4 = besselj(nord(i)-1,Lp,1).*exp(1j*real(Lp));
                Left4(Ap) = Left4(Ap).*exp(-2*imag(Lp(Ap)));
            else
                Left1 = Hc0m(:,l,i-1);
                Left2 = Jc0m(:,l,i-1);
                Left3 = Hc0p(:,l,i-1);
                Left4 = Jc0p(:,l,i-1);
            end
            if i == Nord
                Right1 = besselh(nord(i)+1,1,Lm,1);
                Right2 = besselj(nord(i)+1,Lm,1).*exp(1j*real(Lm));
                Right2(Am) = Right2(Am).*exp(-2*imag(Lm(Am)));
                Right3 = besselh(nord(i)+1,1,Lp,1);
                Right4 = besselj(nord(i)+1,Lp,1).*exp(1j*real(Lp));
                Right4(Ap) = Right4(Ap).*exp(-2*imag(Lp(Ap)));
            else
                Right1 = Hc0m(:,l,i+1);
                Right2 = Jc0m(:,l,i+1);
                Right3 = Hc0p(:,l,i+1);
                Right4 = Jc0p(:,l,i+1);
            end
            Hc1m(:,l,i) = (Left1-Right1)/2;
            Jc1m(:,l,i) = (Left2-Right2)/2;
            Hc1p(:,l,i) = (Left3-Right3)/2;
            Jc1p(:,l,i) = (Left4-Right4)/2;
        end

    end

    display('done with bessel')

    Chipm = Hc1m./Hc0m;
    Chimm = Jc1m./Jc0m;
    Chipp = Hc1p./Hc0p;
    Chimp = Jc1p./Jc0p;

    display('done with Chi')

    Yp = zeros(2*Nb,Nr-2,Nord);
    Ym = zeros(2*Nb,Nr-2,Nord);

    for l = 1:Nr-2

        L_Drho = Lambda(:,l+1)*(bnd_r(l+1)-bnd_r(l));

        for i = 1:Nord
            Yp(:,l,i) = exp(1j*L_Drho).*(Hc0p(:,l+1,i)./Hc0m(:,l,i));
            Ym(:,l,i) = exp(1j*L_Drho).*(Jc0m(:,l,i)./Jc0p(:,l+1,i));
        end
```

```
    end

    display('done with gamma')

    Q = zeros(2*Nb,2*Nb,Nr-1,Nord);

    for i = 1:Nord

        Tp = zeros(2*Nb,2*Nb,Nr-1);
        Tm = zeros(2*Nb,2*Nb,Nr-1);

        Rp = zeros(2*Nb,2*Nb,Nr-1);
        Rm = zeros(2*Nb,2*Nb,Nr-1);

        for l = 1:Nr-1

            beta1pp = zeros(2*Nb,2*Nb);
            beta1mp = zeros(2*Nb,2*Nb);
            beta2pm = zeros(2*Nb,2*Nb);

            beta1mm = zeros(2*Nb,2*Nb);
            beta1pm = zeros(2*Nb,2*Nb);
            beta2mp = zeros(2*Nb,2*Nb);

            beta1pp(B1,B1) = 1j*nord(i)/bnd_r(l)*Dhe(:,:,l);
            beta1pp(B2,B1) = -diag(Chipp(B1,l,i).*Lambda(B1,l));
            beta1pp(B1,B2) = -
1j*omega*muo*diag(Chipp(B2,l,i).*Lambda(B2,l));
            beta1pp(B2,B2) = 1j*nord(i)/bnd_r(l)*Deh(:,:,l);

            beta1mp(B1,B1) = 1j*nord(i)/bnd_r(l)*Dhe(:,:,l);
            beta1mp(B2,B1) = -diag(Chimp(B1,l,i).*Lambda(B1,l));
            beta1mp(B1,B2) = -
1j*omega*muo*diag(Chimp(B2,l,i).*Lambda(B2,l));
            beta1mp(B2,B2) = 1j*nord(i)/bnd_r(l)*Deh(:,:,l);

            beta2mp(B1,B1) = 1j*nord(i)/bnd_r(l)*Dhem(:,:,l);
            beta2mp(B2,B1) = -
P2m(B1,B1,l)*diag(Chimp(B1,l,i).*Lambda(B1,l));
            beta2mp(B1,B2) = -
1j*omega*muo*P2m(B2,B2,l)*diag(Chimp(B2,l,i).*Lambda(B2,l));
            beta2mp(B2,B2) = 1j*nord(i)/bnd_r(l)*Dehm(:,:,l);

            beta1pm(B1,B1) = 1j*nord(i)/bnd_r(l)*Dhe(:,:,l+1);
            beta1pm(B2,B1) = -diag(Chipm(B1,l,i).*Lambda(B1,l+1));
            beta1pm(B1,B2) = -
1j*omega*muo*diag(Chipm(B2,l,i).*Lambda(B2,l+1));
            beta1pm(B2,B2) = 1j*nord(i)/bnd_r(l)*Deh(:,:,l+1);

            beta1mm(B1,B1) = 1j*nord(i)/bnd_r(l)*Dhe(:,:,l+1);
```

```
            beta1mm(B2,B1) = -diag(Chimm(B1,l,i).*Lambda(B1,l+1));
            beta1mm(B1,B2) = -
1j*omega*muo*diag(Chimm(B2,l,i).*Lambda(B2,l+1));
            beta1mm(B2,B2) = 1j*nord(i)/bnd_r(l)*Deh(:,:,l+1);

            beta2pm(B1,B1) = 1j*nord(i)/bnd_r(l)*Dhep(:,:,l);
            beta2pm(B2,B1) = -
P2p(B1,B1,l)*diag(Chipm(B1,l,i).*Lambda(B1,l+1));
            beta2pm(B1,B2) = -
1j*omega*muo*P2p(B2,B2,l)*diag(Chipm(B2,l,i).*Lambda(B2,l+1));
            beta2pm(B2,B2) = 1j*nord(i)/bnd_r(l)*Dehp(:,:,l);

            beta1pp = beta1pp*diag(power(Lambda(:,l),-2));
            beta1mp = beta1mp*diag(power(Lambda(:,l),-2));
            beta2mp = beta2mp*diag(power(Lambda(:,l),-2));
            beta1pm = beta1pm*diag(power(Lambda(:,l+1),-2));
            beta1mm = beta1mm*diag(power(Lambda(:,l+1),-2));
            beta2pm = beta2pm*diag(power(Lambda(:,l+1),-2));

            Tp(:,:,l) = (beta2pm-beta1mp*P1p(:,:,l))\(beta1pp-beta1mp);
            Tm(:,:,l) = (beta2mp-beta1pm*P1m(:,:,l))\(beta1mm-beta1pm);

            Rp(:,:,l) = P1p(:,:,l)*Tp(:,:,l)-eye(2*Nb);
            Rm(:,:,l) = P1m(:,:,l)*Tm(:,:,l)-eye(2*Nb);

        end

        display('done with local matrices')

        for l = (Nr-1):-1:1
            if l == Nr-1
                Q(:,:,l,i) = Rp(:,:,l);
            else
                Q1 = diag(Ym(:,l,i))*Q(:,:,l+1,i)*diag(Yp(:,l,i));
                S = (eye(2*Nb)-Rm(:,:,l)*Q1)\Tp(:,:,l);
                Q(:,:,l,i) = Rp(:,:,l)+Tm(:,:,l)*Q1*S;
            end
        end

        display('done with generalized matrix')

    end
end
```

The calculation of differential magnetic fields for all sampling points:

```
function [z_obsrvr,Hsca] = scattered(string,Cmat,Lambda,Q,Hc0p,Jc0p)
```

```
global bnd_r mur_sz nord Nord Nb B2

fid = fopen(strcat(string,'sampling.txt'));

Zstart = str2num(strtok(fgetl(fid),'%'));
Zend = str2num(strtok(fgetl(fid),'%'));
Nsamples = str2num(strtok(fgetl(fid),'%'));
Ltr1 = str2num(strtok(fgetl(fid),'%'));
Ltr2 = str2num(strtok(fgetl(fid),'%'));

alfa = (Ltr1/Ltr2)^3;

fclose(fid);

rhoa = 1e-6;

Lb = Lambda(:,1)*bnd_r(1);
La = Lambda(:,1)*rhoa;

Aa = imag(La)<0;

Hcap_a = zeros(2*Nb,Nord);
Jcap_a = zeros(2*Nb,Nord);

Q_a = zeros(2*Nb,2*Nb,Nord);

for i = 1:Nord

    Hcap_a(:,i) = besselh(nord(i),1,La,1);
    Jcap_a(:,i) = besselj(nord(i),La,1).*exp(1j*real(La));
    Jcap_a(Aa,i) = Jcap_a(Aa,i).*exp(-2*imag(La(Aa)));

    Yp_a = exp(1j*(Lb-La)).*(Hc0p(:,1,i)./Hcap_a(:,i));
    Ym_a = exp(1j*(Lb-La)).*(Jcap_a(:,i)./Jc0p(:,1,i));

    Q_a(:,:,i) = diag(Ym_a)*Q(:,:,1,i)*diag(Yp_a);

end

display('all done before sampling')

z_source = linspace(Zstart,Zend,Nsamples)';
z_obsrv1 = z_source+Ltr1;
z_obsrv2 = z_source+Ltr2;

Hsca1 = zeros(Nsamples,1);
Hsca2 = zeros(Nsamples,1);

for k = 1:Nsamples
```

```
        gh_source = sampling(z_source(k),mur_sz(1,1));
        gh_obsrv1 = sampling(z_obsrv1(k),mur_sz(1,1));
        gh_obsrv2 = sampling(z_obsrv2(k),mur_sz(1,1));
        for i = 1:Nord
            bph =
1/4j/mur_sz(1,1)*diag(Hcap_a(B2,i).*Jcap_a(B2,i).*Lambda(B2,1).^2)*...
                transpose(Cmat(B2,B2,1))*gh_source;
            Hsca_n_1 =
1/mur_sz(1,1)*gh_obsrv1'*Cmat(B2,B2,1)*Q_a(B2,B2,i)*bph;
            Hsca_n_2 =
1/mur_sz(1,1)*gh_obsrv2'*Cmat(B2,B2,1)*Q_a(B2,B2,i)*bph;
            if i == 1
                Hsca1(k,1) = Hsca1(k,1)+Hsca_n_1;
                Hsca2(k,1) = Hsca2(k,1)+Hsca_n_2;
            else
                Hsca1(k,1) = Hsca1(k,1)+2*Hsca_n_1;
                Hsca2(k,1) = Hsca2(k,1)+2*Hsca_n_2;
            end
        end
    end

    Hsca = Hsca2-Hsca1*alfa;
    z_obsrvr = z_source+(Ltr2+Ltr1)/2;

end

function geta = sampling(z_dash,qeta)

    % wellbore must be homogeneous

    global Zglobal dz Ne Nb

    geta = zeros(Nb,1);

    for i = 1:Ne
        if and(z_dash>=Zglobal(i),z_dash<Zglobal(i+1))
            L1 = (Zglobal(i+1)-z_dash)/dz(i);
            L2 = (z_dash-Zglobal(i))/dz(i);
            geta(2*i-3) = -2*L1^3+3*L1^2;
            geta(2*i-2) = qeta*dz(i)*L1^2*L2;
            geta(2*i-1) = -2*L2^3+3*L2^2;
            geta(2*i) = -qeta*dz(i)*L2^2*L1;
        end
    end
end
```

The info.dat is an output file which provides information on the computation time (solving the generalized eigenvalue problem, refraction matrix fill time, solution time for

all sampling points and total run time), number of basis functions and number of source points. Another output file, the out.dat, provides calculated real and imaginary voltages for the *z*-oriented receiver coil (transmitter coil is also *z*-oriented) and for all sampling points.

SIMULATED ANNEALING / NEIGHBOR APPROXIMATION

The Matlab code inverts tri-axial induction tool data for recovering fracture parameters: conductivity, radius and dip-angle. To run the program, one needs the input file of inversion.txt in addition to the information required for the forward runs, i.e., node spacing, and well radius. An example for inversion.txt is shown below:

```
100         % number of iterations
5           % number of models in each iteration
3           % number of model parameters
10          % minimum value for fracture conductivity
1           % minimum value for fracture radius
0           % minimum value for fracture dip-angle
500         % maximum value for fracture conductivity
100         % maximum value for fracture radius
80          % maximum value for fracture dip-angle
```

Main function:

```
clear all; close all; clc;

string = strcat(pwd,'\Library\hfd_2_8m_30deg\');

indata = load(strcat(string,'inversion.txt'));

nog = indata(1);          % number of generations
now = indata(2);          % number of walkers in each generation
nop = indata(3);          % number of parameters in each model

m_min = indata(4:3+nop);
m_max = indata(4+nop:3+2*nop);

% R2 is saving any model and its energy which evaluated
```

```
R2 = vfsa(string,m_min,m_max,nog,now,nop);

dlmwrite(strcat(string,'inv_R2.dat'),R2,'delimiter','\t');
```

The vfsa function iterates models by randomly selecting and evaluating:

```
function R2 = vfsa(string,m_min,m_max,nog,now,nop)

    R2 = zeros(nog*now,1+nop);

    m_1 = zeros(nop,now);
    m_2 = zeros(nop,now);
    E_1 = zeros(1,now);
    E_2 = zeros(1,now);

    for j = 1:now
        m_1(:,j) = m_min+rand(nop,1).*(m_max-m_min);
        E_1(j) = errcall(string,m_1(:,j));
        R2(j,:) = [E_1(j),m_1(:,j)'];
    end

    for i = 2:nog
        T = temperature(i,nog);
        for j = 1:now
            for k = 1:nop
                m_2(:,j) = offspring(m_1(:,j),k,m_min,m_max,T);
                if k < nop
                    E_2(j) = neighbor(m_2(:,j),R2(1:(i-1)*now,:),...
                                      m_min,m_max);
                else
                    E_2(j) = errcall(string,m_2(:,j));
                    R2((i-1)*now+j,:) = [E_2(j),m_2(:,j)'];
                end
                d_E = E_2(j)-E_1(j);
                if d_E <= 0
                    m_1(k,j) = m_2(k,j);
                    E_1(j) = E_2(j);
                else
                    if exp(-d_E/T) > rand
                        m_1(k,j) = m_2(k,j);
                        E_1(j) = E_2(j);
                    end
                end
            end
        end
        [m_1,E_1] = selection(m_1,E_1);

        display(['Number of Generation is ' num2str(i)])
```

```
    end
end
```

The errcall function calculates error based on Eq. 4.2 by comparing each forward model to the measured data. The MOM solution shown in the Appendix is attached to this function to evaluate the forward models:

```
function E = errcall(string,param)

    G_frac = param(1)*0.005;
    r_frac = param(2);
    dipang = param(3);

    muo = 4*pi*1E-7;    % free space electrical permeability, [H/m]
    epso = 8.854187817*1E-12;   % free space permittivity, [F/m]

    opcond = load(strcat(string,'operation.txt'));

    omega = 2*pi*opcond(1);     % angular frequency, [rad.Hz]
    Mtr = prod(opcond(2:4));

    k1 = sqrt(muo*epso*omega^2-1j*muo*opcond(5)*omega);

    geometry(r_frac,dipang,string);

    [Zmn,Bmn] = impedance(k1,opcond(6));

    Tmn = 1j*omega*muo*Zmn+Bmn/G_frac;
    Hsca = scattered(k1,opcond(7),Tmn,string);

    Vhfd = load(strcat(string,'out.dat'));

    Vdsh_yz = abs(Vhfd(:,3)+1j*Vhfd(:,4));
    Vsca_yz = abs(-1j*(muo*omega)^2*Mtr*(Hsca(:,2))*1e6);
    Vdsh_zz = abs(Vhfd(:,5)+1j*Vhfd(:,6));
    Vsca_zz = abs(-1j*(muo*omega)^2*Mtr*(Hsca(:,3))*1e6);

    Vdsh = [Vdsh_yz; Vdsh_zz];
    Vsca = [Vsca_yz; Vsca_zz];

    E = (Vsca./Vdsh-1)'*(Vsca./Vdsh-1);
end
```

The temperature function is a control parameter:

```
function T = temperature(i,nog)

    To = 1;     % initial temperature, popular spec. is 1
    Tf = 1e-2; % final temperature, popular specs. are [0.01 0.1]
    T = To*power(Tf/To,(i-1)/(nog-1));

end
```

In the given iteration, the exact error value is calculated only once for each model. The neighbor function uses history of forward models to estimate errors for one-directional moves.

```
function energy = neighbor(m,G_E,m_min,m_max)

    nop = size(m,1);            % number of parameters
    noE = size(G_E,1);          % number of previous forward runs

    mb = G_E(:,2:1+nop)';
    distance = zeros(noE,1);

    si = m_max-m_min;

    Cm = diag(1./power(si,2));  % dimensionalize parameter space

    for i = 1:noE
        distance(i) = sqrt((m-mb(:,i))'*Cm*(m-mb(:,i)));
    end

    [~,n] = min(distance);
    energy = G_E(n,1);

end
```

The offspring function generates new model from a given old model by the random shift in one dimension:

```
function [m_n] = offspring(m_o,k,m_min,m_max,tmp)

    m_n = m_o;          % produced new model

    for ntry = 1:100
```

```
        dif = rand-0.5;
        if dif < 0
            sign = -1;
        end
        if dif >= 0
            sign = 1;
        end
        m_t = m_o(k)+sign*rand*tmp*(m_max(k)-m_min(k));
        if m_t>=m_min(k) && m_t<=m_max(k)
            break;
        end
    end

    if ntry >= 100
        error('could not find search point from cauchy distribution')
    end

    m_n(k) = m_t;

end
```

The out.dat is an output file which provides error and model parameters for every computed forward model.

References

Adisoemarta, P.S., 1999, Complex electrical properties of shale as a function of frequency and water content: Ph.D. dissertation, Texas Tech University.

Balan, H.O., A. Gupta, and D.T. Georgi, 2017, Feasibility of predicting long-term shale gas production and EURs based on early-time data: Presented at the SPE Middle East Oil & Gas Show and Conference, doi: 10.2118/183754-MS.

Balanis, C.A., 2005, Antenna theory analysis and design: John Wiley & Sons, Inc.

Basu, S., 2014, Fracture diagnostics using low-frequency electromagnetic induction: M.S. thesis, The University of Texas at Austin.

Basu, S., and M.M. Sharma, 2014, A new method for fracture diagnostics using low-frequency electromagnetic induction: Presented at the SPE Hydraulic Fracturing Technology Conference, doi: 10.2118/168606-MS.

Batchelor, A.S., R. Baria, and K. Hearn, 1983, Monitoring the effects of hydraulic stimulation by microseismic event location: a case study: Presented at the SPE-AIME Annual Technical Conference and Exhibition, doi: 10.2118/12109-MS.

Blyton, C.A.J., D.P. Gala, and M.M. Sharma, 2015, A comprehensive study of proppant transport in a hydraulic fracture: Presented at the SPE Annual Technical Conference and Exhibition, doi: 10.2118/174973-MS.

Davidson, D.B., 2011, Computational electromagnetics for RF and microwave engineering: Cambridge University Press.

Duesterhoeft, W.C., R.E. Hartline, and H.S. Thomsen, 1961, The effect of coil design on the performance of the induction log: Journal of Petroleum Technology, **13**, no. 11, 1137-1150, doi: 10.2118/1558-G-PA.

Eftekhari, B., M. Marder, and T.W. Patzek, 2018, Field data provide estimates of effective permeability, fracturing spacing, well drainage area and incremental production in gas

shales: Journal of Natural Gas Science and Engineering, **56**, 141-151, doi: 10.1016/j.jngse.2018.05.027

Fluke 1625, 2006, Earth/ground tester user manual: Fluke Corporation.

Fouskakis, D., and D. Draper, 2002, Stochastic optimization, a review: International Statistical Review, 70, no. 3, 315-349, doi: 10.1111/j.1751-5823.2002.tb00174.x

Frischknecht, F.C., 1988, Electromagnetic physical scale modeling, *in* M.N. Nabighian, ed., Electromagnetic methods in applied geophysics: Theory: SEG, 365-469.

Gianzero, S., Y. Lin, and S. Su, 1985, A new high-speed hybrid technique for simulation and inversion of resistivity logs: SPE Formation Evaluation, **3**, no. 1, 55-61, doi: 10.2118/14189-PA

Gul, S., and V. Aslanoglu, 2018, Drilling and well completion cost analysis of geothermal wells in turkey: Presented at the 43rd Workshop on Geothermal Reservoir Engineering.

Heagy, L.J., and D.W. Oldenburg, 2013, Investigating the potential of using conductive or permeable proppant particles for hydraulic fracture characterization: 83rd Annual International Meeting, SEG, Expanded Abstracts, 576-580.

Hibbs, A.D., 2014, Evaluation of deep subsurface resistivity imaging for hydrofracture monitoring, https://www.netl.doe.gov/File%20Library/Research/Oil-Gas/Natural%20Gas/fe0013902-qpr-jan-mar-2014.pdf, accessed 1 November 2015.

Hoversten, G.M., M. Commer, E. Haber, and C. Schwarzbach, 2015, Hydro-frac monitoring using ground time-domain electromagnetics: Geophysical Prospecting, **63**, 1508-1526, doi: 10.1111/1365-2478.12300.

Jin, J.M., 2010, Theory and computation of electromagnetic fields: John Wiley & Sons, Inc.

Kaur, G., and A.E. Yilmaz, 2011, A practical implementation and comparative assessment of the radial-angular-transform singularity cancellation method: IEEE Transactions on Antennas and Propagation, **59**, no. 12, doi: 10.1109/TAP.2011.2165516

LaBrecque, D., R. Brigham, J. Denison, L. Murdoch, W. Slack, Q.H. Liu, Y. Fang, J. Dai, Y. Hu, Z. Yu, A. Kleinhammes, P. Doyle, Y. Wu, and M. Ahmadian, 2016, Remote imaging of proppants in hydraulic fracture networks using electromagnetic methods: results of small-scale field experiments: Presented at the SPE Hydraulic Fracturing Technology Conference, doi: 10.2118/179170-MS.

Lindell, I.V., 1992, Methods for electromagnetic field analysis: Clarendon Press.

Li, J., and L.C. Shen, 1993, Vertical eigenstate method for simulation of induction and MWD resistivity sensors: IEEE Transactions on Geoscience and Remote Sensing, **31**, no. 2, 399–406, doi: 10.1109/36.214916

Liu, Q.H., Z. Yu, J. Zhou, 2015, Electromagnetic (EM) well logging tools and related methods: U.S. Patent WO/2016/144457.

Lovell, J.R., 1993, Finite element methods in resistivity logging: Ph.D. dissertation, Delft University of Technology.

Pai, D.M., 1991, Induction log modeling using vertical eigenstates: IEEE Transactions on Geoscience and Remote Sensing, **29**, no. 2, 209–213, doi: 10.1109/36.73661

Palisch, T., W. Al-Tailji, L. Bartel, C. Cannan, M. Czapski, and K. Lynch, 2016, Recent advancements in far-field proppant detection: Presented at the SPE Hydraulic Fracturing Technology Conference doi: 10.2118/ 179161-MS.

Pardo, D., and C. Torres-Verdin, 2013, Sensitivity analysis for the appraisal of hydrofractures in horizontal wells with borehole resistivity measurements: Geophysics, **78**, no. 4, D209-D222, doi: 10.1190/geo2013-0014.1.

Qian, Z.G., W.C. Chew, and R. Suaya, 2007, Generalized impedance boundary condition for conductor modeling in surface integral equation: IEEE Transactions on Microwave Theory and Techniques, **55**, no. 11, doi: 10.1109/TMTT.2007.908678.

Rao, S.M., D.R. Wilton, and A.W. Glisson, 1982, Electromagnetic scattering by surfaces of arbitrary shape: IEEE Transactions on Antennas and Propagation, 30, no. 3, doi: 10.1109/TAP.1982.1142818.

Ren, Y., W.F. Huang, Q.H. Liu, and Y.P. Chen, 2016, Accurate fracture scattering simulation by thin dielectric sheet-based surface integral equation: IEEE Geoscience and Remote Sensing Letters, **13**, no. 10, 1448-1451, doi: 10.1109/LGRS.2016.2591079.

Salies, N.G., 2012. Study on the feasibility of using electromagnetic methods for fracture diagnostics: M.S. thesis, The University of Texas at Austin.

Sambridge, M., 1999, Geophysical inversion with a neighborhood algorithm – I. searching a parameter space, Geophysical Journal International, 138, no. 2, 479-494, doi: 10.1046/j.1365-246X.1999.00876.x

Sen, M., and P. Stoffa, 2013, Global optimization methods in geophysical inversion: Cambridge University Press.

Sharma, M.M., and R. Manchanda, 2015, The role of induced un-propped (IU) fractures in unconventional oil and gas wells: Presented at the SPE Annual Technical Conference and Exhibition, doi: 10.2118/174946- MS.

Shiriyev, J., Y. Brick, P. Zhang, A.E. Yilmaz, C. Torres-Verdin, M.M. Sharma, T. Hosbach, M.A. Oerkfitz, and J. Gabelmann, 2018, Experiments and simulations of a prototype tri-axial electromagnetic induction logging tool for open-hole hydraulic fracture diagnostics: Geophysics, **83**, no. 3, D73-D81, doi: 10.1190/GEO2017-0354.1

Shrivastava, K., and M.M. Sharma, 2018, Proppant transport in complex fracture networks: Presented at the SPE Hydraulic Fracturing Technology Conference and Exhibition, doi: 10.2118/189895-MS.

Sinclair, G., 1948, Theory of models of electromagnetic systems: Proceedings of the IEEE, **36**, no. 11, 1364-1370, doi: 10.1109/JRPROC.1948.232289.

Smolen, J.J., and A. Spek, 2003, Distributed temperature sensing, http://w3.energistics.org/schema/witsml_v1.3.1_data/doc/Shell_DTS_Primer.pdf, accessed 30 May 2017.

Sookprasong, P.A., R.S. Hurt, and C.C. Gill, 2014, Downhole monitoring of multi-cluster, multi-stage horizontal well fracturing with fiber optic distributed acoustic sensing (DAS) and distributed temperature sensing (DTS): Presented at the International Petroleum Technology Conference, doi: 10.2523/IPTC-17972-MS

Swift, C.M., 1988, Fundamentals of the electromagnetic method, *in* M.N. Nabighian, ed., Electromagnetic methods in applied geophysics: Theory: SEG, 5-13.

Ugueto, G.A., Huckabee, P.T., Molenaar, M.M., Wyker, B., and Somanchi, K., 2016, Perforation cluster efficiency of cemented plug and perf limited entry completions; insight from fiber optics diagnostics: Presented at the SPE Hydraulic Fracturing Technology Conference, doi: 10.2118/179124-MS.

Wang, G.L., C. Torres-Verdin, and S. Gianzero, 2009, Fast simulation of tri-axial borehole induction measurements acquired in axially symmetrical and transversely isotropic media: Geophysics, **74**, no. 6, E233-E249, doi: 10.1190/1.3261745

Warpinski, N.R., and P.T. Branagan, 1989, Altered stress fracturing: Journal of Petroleum Technology, **41**, no. 9, 990-997, doi: 10.2118/17533-PA.

Wheaton, B., K. Haustveit, and W. Deeg, 2016, A case study of completion effectiveness in the Eagle Ford Shale using DAS/DTS observations and hydraulic fracture monitoring: Presented at the SPE Hydraulic Fracturing Technology Conference, doi: 10.2118/179149-MS

Wu, C., S. Yi, and M.M. Sharma, 2017, Proppant distribution among multiple perforation clusters in a horizontal wellbore: Presented at the SPE Hydraulic Fracturing Technology Conference and Exhibition, doi: 10.2118/184861-MS.

Yang, K., and A. E. Yilmaz, 2014, An FFT-accelerated integral equation solver for analyzing scattering in rectangular cavities: IEEE Transactions on Microwave Theory and Techniques, **62**, no. 9, 1930-1942, doi: 10.1109/TMTT.2014.2335176.

Yang, K., A.E. Yilmaz, and C. Torres-Verdin, 2016, Efficient 3D parametric inversion of hydraulic fractures with low frequency borehole tri-axial electromagnetic measurements: 86th Annual International Meeting, SEG, Expanded Abstracts, 954-958.

Yang, K., C. Torres-Verdin, and A.E. Yilmaz, 2015, Detection and quantification of three-dimensional hydraulic fractures with horizontal borehole resistivity measurements: IEEE Transactions on Geoscience and Remote Sensing, **53**, no. 8, 4605-4615, doi: 10.1109/TGRS.2015.2402656.

Yu, Z., J. Zhou, Y. Fang, Y. Hu, and Q. H. Liu, 2016, Through-casing hydraulic fracture evaluation by induction logging II: the inversion algorithm and experimental validations: IEEE Geoscience and Remote Sensing, **55**, no. 2, 1189-1198, doi: 10.1109/TGRS.2016.2621002.

Zhang, G.J., G.L. Wang, and H.M. Wang, 1999, Application of novel basis functions in a hybrid method simulation of the response of induction logging in axisymmetrical stratified media: Radio Science, **34**, no. 1, 19-26, 10.1029/98RS02767

Zhang, P., J. Shiriyev, C. Torres-Verdin, M.M. Sharma, Y. Brick, J. Massey, and A.E. Yilmaz, 2016, Fracture diagnostics using a low-frequency electromagnetic induction method: Presented at the 50th US Rock Mechanics/Geomechanics Symposium.